BIOPHYSICAL STUDIES ON THE MISFOLDING AND AGGREGATION OF HUMAN β_2-MICROGLOBULIN AND A YEAST PRION DETERMINANT

DOMINIC NARANG

Thesis submitted for the partial fulfilment of the degree of

DOCTOR OF PHILOSOPHY

Department of Biological Sciences

Indian Institute of Science Education and Research (IISER) Mohali

November, 2015

CERTIFICATE

The work presented in this thesis has been carried out by me under the supervision of Dr. Samrat Mukhopadhyay at the Department of Biological Sciences, Indian Institute of Science Education and Research (IISER) Mohali.

This work has not been submitted in part or full for a degree, a diploma, or a fellowship to any other university or institute.

Whenever contributions of others are involved, every effort is made to indicate this clearly, with due acknowledgement of collaborative research and discussions. This thesis is a bonafide record of original work done by me and all sources listed within have been detailed in the bibliography.

Date **Place** **Dominic Narang**

In my capacity as supervisor of the candidate's thesis work, I certify that above statements made by candidate are true to best of our knowledge.

Dr. Samrat Mukhopadhyay

(Supervisor)

Dedicated To My Family

ACKNOWLEDGEMENTS

"Knowledge is in the end based on acknowledgement."- Ludwig Wittgenstein

This thesis could not have been completed without the guidance of my supervisor, Dr. Samrat Mukhopadhyay, whom I thank for all his patience and support over the years. His enormous experience and continuous scientific input were crucial in helping me to grow as an independent scientist. He has provided a free research environment that allowed me to gain crucial experience in an overall friendly environment.

I am thankful to the Director IISER Mohali, Professor N. Satyamurthy for providing us the excellent research facilities to work in the institute.

I wish to thank the members of my doctoral committee, Dr. Samarjit and Professor Anand Bachhawat, for their advices, encouragement, and critical critiques that they freely and frequently offered.

I extend my heartfelt thanks to all the members of the Mukhopadhyay lab, both past and present members Dr. Pushpender Kumar Sharma, Dr. Mily Bhattacharya, Dr. Neha Jain, Vijit Dalal, Shruti Arya, Karishma Bhasne, Hema Swasthi, Priyanka dogra, Priyanka Madhu, Vinodh, Shambu, Anubhuti Singh, Simarbir Kaur and Satavisa for their kind support and for always keeping conducive lab environment.

I would like to dedicate special thanks to Dr. Pushpender Kumar Sharma for initiating the project on human β_2m in the lab and his critical input into the work. I would like to express my deep gratitude to Vinodh, Hema Swasthi, Anubhuti Singh and Simarbir for their immense support for my work and critical input into my thesis.

I am thankful to Prof G. Krishnamoorthy (TIFR Mumbai) for providing us access to time-resolved fluorescence instrument.

I am thankful to my friends Dr. Anil, Dr. Shailesh, Aman, Zulkifli, Avinash, Shruti and bhishem for being wonderful company and extending their help whenever required.

I would like to express my extreme thanks to my family and my wife Kanika for their continuous support and patience over the years, without which I would not have been able to complete this work successfully.

My sincere appreciation goes to all IISER faculty members, staff, library, and instrumentation etc. whose help and support was always there when needed.

I sincerely thank all of them whom I have unintentionally left out; who at some point of time, in some way or the other, have contributed in this journey.

The financial support by CSIR and CPSDE is duly acknowledged.

Dominic Narang

Synopsis

Biophysical Studies on the Misfolding and Aggregation of Human β_2-Microglobulin and a Yeast Prion Determinant

Dominic Narang

Department of Biological Sciences

Indian Institute of Science Education and Research (IISER) Mohali

Thesis Supervisor: Samrat Mukhopadhyay

Chapter 1: Introduction

Protein misfolding and aggregation resulting in amyloid formation are associated with a large number of human diseases including Alzheimer disease, Parkinson disease, Transmissible Spongiform Encephalopathies, Huntington disease, Frontotemporal dementia, and Amyotrophic lateral sclerosis. Various studies on deciphering the mechanism of protein aggregation indicate that the partial unfolding of the native structure of a protein is one of the major driving forces for amyloid formation. Therefore, it is necessary to understand how certain conditions perturb the protein structure and which regions of the protein are more prone to aggregation under stress conditions. Further, polymorphism is an important property of amyloid fibrils in which a single protein/ peptide give rises to amyloid fibrils with diverse morphologies and structures complicating the disease pathology. The cause of amyloid polymorphism is still under investigation. From various studies, it is suggested that environment stress caused by a change in pH or oxidative stress or poor quality control can affect the fibril formation and morphologies. To address these questions, we have used human β_2-microglobulin (β_2m) to study the effect of pH on protein structure unfolding and effect of salt on amyloid fibril morphology. We have also used well-characterized strains of yeast [*PSI*$^+$] prion to study the structural differences and the role of water in two distinct strains. The details of studies are described in the following chapter.

Chapter 2: Dynamics and dimension of an amyloidogenic disordered state of human β_2-microglobulin

Human β_2-microglobulin aggregation is implicated in dialysis-related amyloidosis. At pH 2.5, β_2m adopts an ensemble of partially unfolded states which coalesces together to forms long

and straight amyloid fibrils that resemble the *ex-vivo* fibrils isolated from the patients. In order to understand the early events of amyloid formation, it is important to elucidate the structural details of the monomeric precursor under the amyloid-forming condition. In this work, we have provided the detailed structural and dynamical insights into the acid-unfolded state of β_2m formed at pH 2.5. Using a host of fluorescence spectroscopic tools, we show that the acid-unfolded state has high 8-anilinonaphthalene, 1-sulfonic acid (ANS) binding affinity and is devoid of significant secondary structural elements. Additionally, using time-resolved fluorescence anisotropy decay measurements, we have been able to distinguish this compact disordered state from the canonical denatured state of the protein by identifying unique dynamic signatures. Taken together, our results suggest that β_2m at pH 2.5 adopts a compact non-canonical unfolded state resembling a pre-molten globule state.

Chapter 3: Kinetics of pH-induced unfolding of human β_2-microglobulin

In this work, we studied the effect of pH change on the unfolding of β_2m using a range of spectroscopic readouts. To investigate the local structural changes, we created single tryptophan (W60 and W95) mutants of β_2m. The equilibrium results suggested that in the acid-unfolded state of β_2m at pH 2.5, W60 residue attains non-native local structure whereas W95 residue becomes more exposed. Our stopped-flow kinetic data revealed that β_2m undergoes unfolding in a stepwise manner. In the initial unfolding event, we observed an unresolved burst-phase in the fluorescence kinetics of W95. However, the protein retained its secondary structural elements during the burst-phase. The change in W95 fluorescence is dependent on the pH and is ascribed to the protonation of side chains. Our results suggest that β_2m expands in a non-uniform manner with the initial unpacking of tertiary structure and significant core solvation while maintaining a native-like structure around W95 residue. The resolved-phase of unfolding exhibits timescale of ~500 ms that describe the transition from the native-like swollen intermediate to an acid-induced disordered state. Our results highlight that β_2m has a complex pH-induced unfolding mechanism yielding a disordered amyloidogenic precursor comprising both exposed and buried segments.

Chapter 4: Effect of salt on the aggregation mechanism of human β_2-microglobulin

Proteins can adopt multiple amyloid conformations depending upon the growth conditions. The variations in the morphology and the internal structure of amyloid fibrils are likely to

constitute the molecular basis of prion strain phenomenon in prion diseases and other amyloid diseases. From various studies, it is evident that a particular growth condition can favor the formation of a particular nucleating species, leading to distinct fibril morphology. The detailed mechanism and structural information about these early nucleating species is still elusive. Previous studies on β_2m have shown that in the presence of different salt (sodium chloride) concentrations at pH 2.5, it assembles into amyloid fibrils with distinct morphologies. However, the early structural changes in the acid-unfolded state induced by salt has not been investigated. In this work, we studied the effect of salt on the acid-unfolded state of the β_2m. Our results from 9-(2,2-Dicyanovinyl) julolidine (DCVJ) fluorescence and light scattering experiments suggest that at low salt concentrations, β_2m remains monomeric, whereas, at high salt concentration, it oligomerizes to form multimers owing to charge shielding by salt. Further, our ANS and circular dichroism experiments indicate the formation of more hydrophobic patches and α-helical structure at high salt concentrations. Along with these experiments, we have gained site-specific information using Trp mutants. At high salt concentration, region harboring W60 residue is more buried in the oligomers compared to the W95 residue. Additionally, our kinetic data suggests that the oligomerization in the presence of high salt occurs rapidly followed by the hydrophobic core formation. Together our results highlight that β_2m at high salt concentration forms α-helical rich-oligomers that lead to a worm-like amyloid morphology in contrast to long and straight fibrils formed at low salt concentration.

Chapter 5: Structural differences between amyloid fibrils of yeast prion probed tryptophan fluorescence

The strain phenomenon is one of the fascinating aspects of prion biology. The prion determinant of the yeast prion [*PSI*$^+$] is an attractive model for studying the structural basis of prion strains. The structural arrangements of protein monomers within the amyloid assembly resulting in morphological polymorphism have been proposed to dictate the strain diversity. The 253-residue NM domain of Sup35p is an intrinsically disordered segment and is sufficient for [*PSI*$^+$] prion initiation and propagation. Earlier it has been shown that two well-defined strains of [*PSI*$^+$] prion can be created *in vitro* at different temperatures. The fibrils formed at 4 °C are thermodynamically less stable compared to the fibrils formed at 37 °C. Interestingly, when introduced into yeast cells, 4 °C fibrils show strong [*PSI*$^+$] phenotype, whereas 37 °C fibrils show weak [*PSI*$^+$] phenotype. The molecular origin of these strains is

postulated to involve diverse, yet related, conformational states and supramolecular packing of proteins within the amyloid fibrils. However, the precise structural and dynamical variations between the prion strains and their distinct physiological impacts remain unknown. To elucidate the structural origin of the prion strains, we took advantage of the fact that NM is devoid of tryptophan and created 19 single tryptophan mutants encompassing the entire length of NM. After establishing that these mutants behave similar to wild-type, we recorded a number of steady-state and dynamic fluorescence readouts that revealed the residue-specific dynamics and the supramolecular packing within the amyloids responsible for different strains. The structural variations in two prion strains provided unique molecular insights into the differential binding of Hsp104 that is known to govern the strain propagation.

Chapter 6: Mapping the dynamics of interstitial water in the amyloid folds of distinct prion strains

The structural conversion of yeast prion protein Sup35 into amyloid fibrils adopt multiple conformations that give rise to distinct [*PSI*$^{+}$] prion phenotypes that are inherited through the action of Hsp104. Recently, the role of hydration dynamics in protein recognition and enzyme catalysis has been recognized but its role in prion formation and prion diversity remains unknown. Therefore, we investigated whether the solvation dynamics has any role to play in two distinct strains of [*PSI*$^{+}$] prion; weak and strong. Since water molecules are optically silent, we exploited the fluorescent properties of tryptophan residue to monitor the solvation dynamics. By using single tryptophan mutants of Sup35 at different residue positions and picosecond spectroscopy, we observed that the overall hydration dynamics is significantly slower in the fibrils in comparison to free tryptophan in water. Interestingly, significant differences were observed in the dynamic nature of water molecules along the polypeptide chain length in different strains of Sup35. Water molecules are more ordered and strongly bound in the weak strain as compared to the strong strain that can have biological relevance in the propagation of two [*PSI*$^{+}$] strains. We propose that the differences in the solvation dynamics in amyloid conformations can be correlated with the severing efficiency of Hsp104 which in turn influence the inheritance pattern of strong and weak strains of [*PSI*$^{+}$] prion.

Table of Contents

Introduction

1.1 Protein folding and misfolding

Proteins are the molecular workhorses that adopt three-dimensional folded structures to perform a diverse array of biological functions. A newly synthesized linear chain of several thousand amino acids has an access to astronomically large conformational space, yet it folds on a biologically relevant timescales. Various *in vitro* studies have shown that many proteins attain their native structures in few microseconds (1). To comprehend this enigmatic problem, a number of concepts have been proposed. First, the presence of non-random local interactions in the unfolded state of polypeptide restricts the conformational space available at the beginning of a folding reaction (2). Second, folding occurs through the formation of intermediates which direct the way to native state (3). Third, folding on a funnelled energy landscape in which native state is most stable (4).

In the protein folding funnel, the unfolded state of a protein represents the top of the funnel which has a large ensemble of structures (Fig. 1.1). The unfolded polypeptide chain may fold into the native structure through several downhill routes which can also includes partially folded intermediates. The initial hydrophobic chain collapse and the formation of native-like contacts restrict the conformational plasticity during folding reactions. However, the free energy surface can be rugged involving significant energy barrier in the folding pathway resulting in accumulation of kinetically trapped species (Fig. 1.1). Such species can be unordered globules with high conformational entropy and lacking native-like secondary and tertiary structures but may contain non-native interactions which can favor the formation of misfolded state of a protein. Accumulation of partially folded or misfolded states at high concentrations are problematic due to their high propensity to self-associate to form aggregates. The presence of exposed hydrophobic surfaces in unordered globules causes intermolecular association to form amorphous aggregate or ordered fibrillar aggregates known as amyloids. Amyloids are defined by hydrogen bonded β-strands that run perpendicular to the long fibril axis (cross-β structure) (5).

Initiation of fibrillation can happen either from the misfolding of the native state (partially unfolded species) or accumulation of partially folded intermediates formed during the folding pathways of a protein. Importantly, the structural conversion of a protein to form amyloid fibrils is often associated with the accumulation of soluble oligomers which are known to be more toxic than the mature fibrils (6). Soluble oligomers are heterogeneous in nature and their toxicity is proposed to linked with the exposed nature of sticky hydrophobic patches and polypeptide backbone (7). Although soluble oligomers are heterogeneous in

nature but still there are some common structural epitopes found on the oligomers of different polypeptides indicating a common structure (8). These soluble oligomers undergo structural rearrangements to form fibrils. Therefore, understanding of such species is utmost important to comprehend the mechanism of amyloid formation.

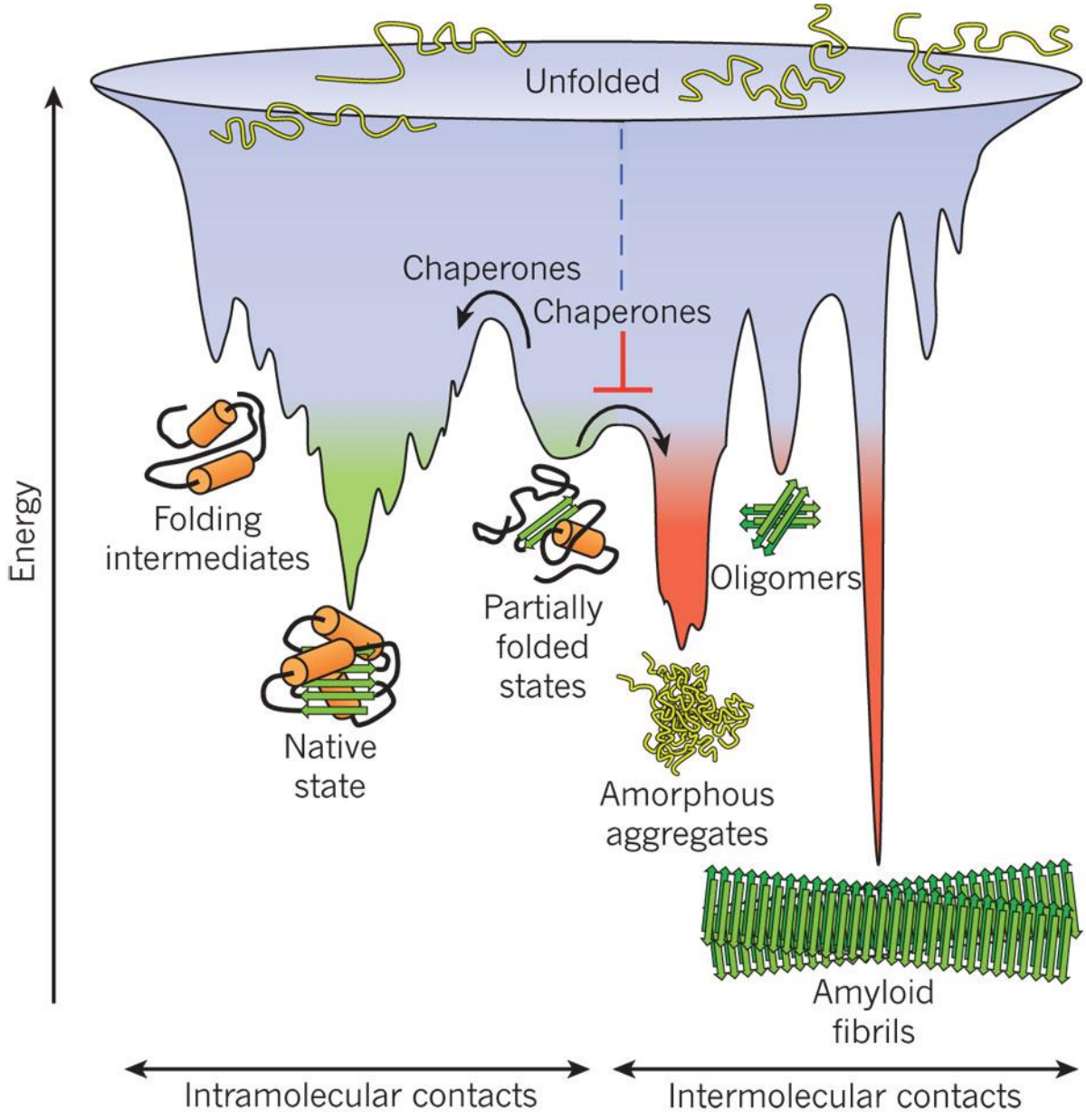

Figure 1.1 Diagrammatic representation of funnel-shaped free-energy surface through which linear chain of polypeptide folds into the native state. Reproduced with permission from Ref. (5).

1.2 Amyloid Structures

Amyloids are homopolymers composed of hundreds to thousands of same protein or peptide molecules. They are typically long, unbranched fibrous structures with a diameter of a few

nanometers and length of often several micrometres. These fibrils have high binding affinities to amyloid-binding dye such thioflavin T (ThT) and Congo red, the later results in green birefringence under polarized microscope. Amyloid fibrils often consist of multiple protofilaments which are tangled around each other to give a twisted ultrastructural appearance. X-ray diffraction studies suggest that the core of each protofilament is composed of multiple β-sheets that run parallel to the fibril axis and each β-sheet consists of perpendicularly oriented β-strands (Fig. 1.2) (9, 10). X-ray fiber diffraction gives two kinds of characteristic diffraction pattern: (a) a meridional reflection at 4.7 Å which corresponds to the inter-β strand spacing, (b) an equatorial reflection at 6-11 Å corresponding to the distance between stacked β-sheets (9, 11). The detailed insights into the packing of protein molecules in amyloid fibrils came from the recent advancements in technologies of cryo-electron microscopy (12, 13) and solid-state NMR spectroscopy (14, 15). Further, X-ray diffraction studies of peptide microcrystals obtained from different proteins provide new insights into the packing of side chains of peptides in the amyloid fibrils (16, 17). These studies confirm that the amyloid state of various proteins have similar overall architecture that can be due to the common features of the polypeptide backbone responsible for the hydrogen bonding pattern in the fibril core. The packing of side chains in the fibrillar structure can cause variation in amyloid structure and morphology (18).

The orientation of β-strands in a sheet can be parallel or antiparallel although the parallel orientation is most widespread (Fig. 1.2). The β-sheets can fall in two main categories: parallel and antiparallel (Fig. 1.2 *a*). The parallel β-sheet has a substantial variation in the organization of β-strands and is further known as in register or out of register. In register refers to the case where, all the β-strand within a β-sheet have identical residues from different molecules stacked upon each other so that each residue is adjacent to the identical residue on neighbouring molecules (Fig. 1.2 *a*). The majority of amyloids fibrils studied appear to have an in-register parallel β-sheet structure but there are few examples where they have pseudo-in register parallel (19, 20) and antiparallel β-sheets (21, 22). An alternate model for cross β-sheet structure is the β-solenoid (Fig. 1.2 *c*). In a β-solenoid model, a polypeptide chain forms two or more rungs or layers connected through the loops. The β-solenoid can be a classic β-helix, where three β-strands often form a triangular layer. An alternate form of β-solenoid is β-roll where two strands along with a loop form a part of layer (Fig. 1.2 *c*). The [HET-s] prion in the fungus *podospora* is formed by the aggregation of HET-s protein which has β-solenoid structure in the amyloid state (14).

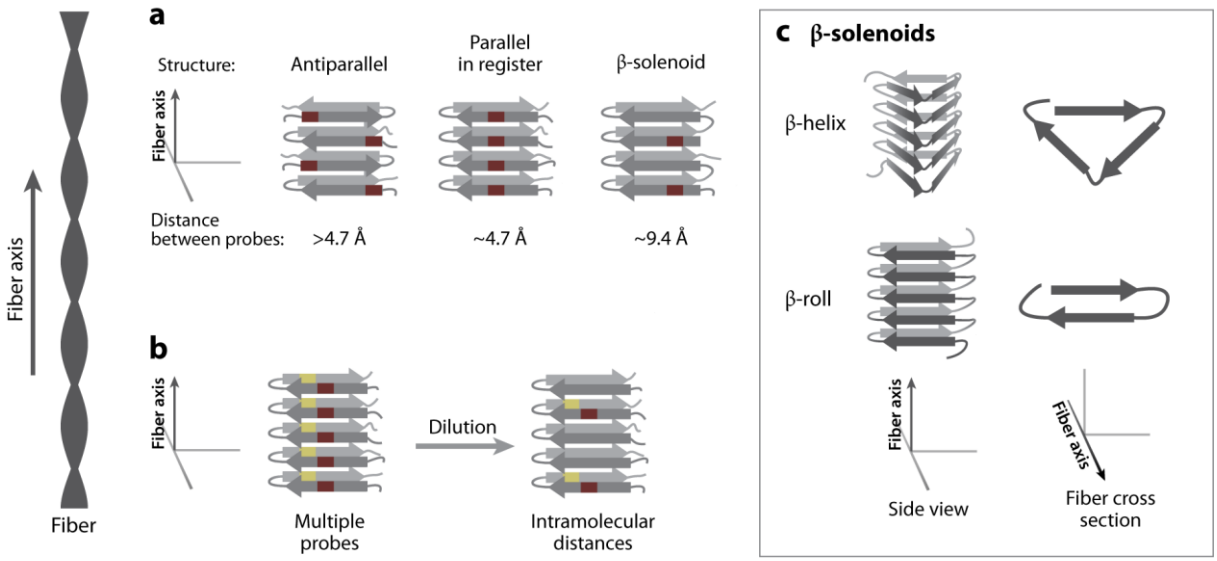

Figure 1.2 Categorization of different amyloid folds and techniques used to distinguish between them. Reproduced with permission from Ref. (23).

The various amyloid structures can be distinguished from each other by introducing a probe at single position in a protein and then estimating the intermolecular distance between the two probes in the amyloid structure. For example, if a probe (red) is installed in a parallel β-sheet structure, then the intermolecular distance should be ~ 4.7 Å (Fig. 1.2 *a*, centre) whereas in case of antiparallel β-sheet structure, it should be greater than 4.7 Å (Fig. 1.2 *a*, left). Similarly for the β-solenoid model, the distance between the probes should be ~ 9.4 Å (Fig. 1.2 *a*, right). These structures can be further distinguished by introducing two dissimilar probes at different positions (Fig. 1.2 *b*). The intra and intermolecular interactions between the probes can be distinguished by dilution of labeled protein. For example, dilution of labeled protein with unlabeled protein should affect the intermolecular distance between molecules as compared to intramolecular distance with in a molecule (Fig. 1.2 *b*) (23).

1.3 Disorders associated with amyloids

There are approximately 50 disorders which are associated with the misfolding of protein and peptides resulting in the formation of amyloid fibrils (24). Few of them are listed in Table 1. The diseases can be broadly classified into three classes (a) neurodegenerative conditions, in which amyloid fibril deposits affect the brain, (b) non-neuropathic localized amyloidoses, in which protein aggregation affects a single type of tissue other than the brain, and (c)

nonneuropathic systemic amyloidoses, in which amyloid fibril deposits affect multiple tissues in different parts of the body (6).

Table 1 Various degenerative diseases caused by the aggregation of peptides/proteins

Disease	Aggregating protein or peptide	Ploypeptide length (number of residues)	Structure of protein or peptide
Neurodegenerative diseases			
Alzheimer's disease	Amyloid-B peptide	37-43	Intrinsically disordered
Spongiform encephalopathies	Prion protein or its fragments	230	Intrinsically disordered and α-helical
Parkinson's disease	α -synuclein	140	Intrinsically disordered
Amyotrophic lateral sclerosis	Superoxidase dismutase-1	153	β-sheet and Ig-like
Huntington's disease	Huntingtin fragments	Variable	Mostly Intrinsically disordered
Familial amyloidotic polyneuropathy	Transthyretin mutants	127	β-sheet
Non-neuropathic systemic amyloidosis			
Amyloid light chain (AL) amyloidosis	Immunoglobulin (Ig) light chains or its fragments	~90	β-sheet and Ig-like
Amyloid A (AA) amyloidosis	Serum amyloid A1 protein fragments	76-104	α-helical and unknown fold
Senile systemic amyloidosis	Wild-type transthyretin	127	β-sheet
Haemodialysis-related amyloidosis	β_2-microglobulin	99	β-sheet and Ig-like
Lyzozyme amyloidosis	Lyzozyme mutants	130	α-helical and β-sheet
Non-neuropathic localized amyloidosis			
Apolipoprotein A1 (Apo A-1) amyloidosis	Apo A-1 fragments	80-93	Intrinsically disordered
Type II diabetes	Amylin	37	Intrinsically disordered
Injection-localized amyloidosis	Insulin	21 and 30	α-helical and insulin-like

1.31 Human β_2-microglobulin: Dialysis-Related Amyloidosis

Human $\beta_2$microglobulin (β_2m) is a light chain of Major Histocompatibility Complex (MHC-I) class I molecule which present antigen to $CD8^+$ T cells (25). After the polypeptide synthesis, subunits translocate into the lumen of the endoplasmic reticulum (ER), where they fold and assemble to form functional class I molecules (25-28). The resulting class I-β_2m heterodimer binds to the peptides primarily generated from proteosomal degradation of cytosolic proteins. After the correct assembly of class I molecules, they are transported from the ER to cell surface (29) and if β_2m is absent, class I molecule fails to transport to the cell surface and are degraded (29, 30). During natural recycling, β_2m dissociate from the MHC I heavy chain and catabolised in the proximal tubules in kidney (31-33). In this way, the concentration of the β_2m is regulated in the body. Due to renal failure, the patients undergoing haemodialysis for a long period has ~50-fold higher concentration of β_2m in the blood (33). Over the years, the protein through unknown mechanism self-associate to form amyloid fibrils which gets deposited in the bones and joints causing painful arthropathy and pathologic fractures (34). This pathological condition is known as dialysis-related amyloidosis (DRA).

Although, the structure and function of β_2m is well studied but its mechanism of amyloid formation *in vivo* leading to disease condition is largely unknown. Moreover, *in vitro* at physiological conditions, β_2m even at a very high protein concentration fails to aggregate (35). In order to accomplish β_2m aggregation *in vitro*, several conditions have been reported which includes low pH (< pH 4) (36) or addition of denaturing agents or organic solvents (37-39) or metal cations like Cu^{2+} (35, 40). These studies have suggested that the key step is the partial unfolding of the monomeric protein. This type of partially unfolded species are known to assemble to form obligatory oligomeric intermediates that are capable of maturing into amyloid fibrils via nucleated conformational conversion (24, 41, 42). Along with *in vitro* studies, attempts have been made to generate a knockout mice model with high expression level of human β_2m protein. The expression level of human β_2m in mice was 100 fold higher than that observed in normal human and 4 times higher than the DRA patients. But amyloid deposits were not observed both in aged or mice injected with amyloid fibrils seeds of β_2m (43). Recently, a natural variant of β_2m (Asp76Asn) was reported in members of a French family who developed progressive bowel dysfunction with extensive visceral amyloid deposits consisting of β_2m. This condition is known as hereditary systemic amyloidosis. In contrast to DRA patients, these members have normal concentration of β_2m in blood and have normal renal function (44, 45). Under physiological conditions, recombinantly

expressed β_2m variant (Asp76Asn) is thermodynamically less stable and is found to be more fibrillogenic compared to wt protein (44).

1.4 Functional Amyloids

Despite the toxic nature of amyloid fibrils, organisms have evolved to take advantage of amyloidogenic properties of proteins (46-51). However, the finding of functional amyloids was very surprising due to the long association of amyloids with human diseases. Functional amyloids are widespread and are identified in bacteria (48, 49), fungi (46, 52-55), insects (50), Aplysia (56, 57) and humans (47). Bacteria employ curli amyloid fibril as a component of the extracellular matrix which is responsible for cell adhesion and colony formation (48, 58, 59). The main component of curli fibrils is CsgA, which is secreted outside the cell in the soluble form and is nucleated by CsgB for fibrillization. The formation of curli fibrils is regulated by two operons which encodes for six proteins (58). Further, the eggs of insects and fishes are protected by the eggshell that is primarily made up of chorion proteins. *In vitro*, these proteins form amyloid fibrils which show Congo red binding and X-ray diffraction pattern (50, 60, 61). Further, X-ray diffraction pattern of intact insect eggshell chorion reveals the amyloid-like diffraction patterns (50).

Several amyloid-based prions in *Saccharomyces cerevisiae* and fungus *podospora anserine* were found to be potentially functional. In *Saccharomyces cerevisiae*, [PSI^+], [*URE3*], and [RNQ^+] are well-studied prions formed by the aggregation of Sup35p, Ure2p and Rnq1p proteins respectively (62-68). The [HET-s] prion in the fungus *podospora* is formed by the aggregation of HET-s protein (19, 69, 70). The [HET-s] prion regulates the heterokaryon formation and prevents the heterokaryon incompatibility between the genetically different colonies (71). In humans, amyloid fibrils of Pmel17 protein is involved in the biogenesis of melanosome (47, 72) and certain peptides and protein hormones are stored in cross β-conformational in secretory granules of the endocrine gland (73). Melanin synthesis takes place in specialized organelles called melanosomes in melanocyte cells which are responsible for skin and eye coloration. The Mα domain cleaved from Pmel17 by proprotein convertase is the primary component of the fibril structure (74, 75). The most important function of amyloid is to provide the template for the chemical synthesis of melanin (76). Further, eukaryotic cells have a unique mechanism for the release of secretory peptides /proteins to the extracellular space from where it is transported to the effector organ (76). These secretory peptides are stored in the high concentration in a membrane-enclosed

secretary granules (77) in the form of amyloid and the nature of these amyloids provides a mechanism to regulate the release of secretory peptides (76).

1.5 Fungal prion

Prion proteins have the ability to adopt at least two distinct states, one of which can stimulate the conversion of non-prion conformation to the prion form. The term "Prion" was first used to describe the infectious agent that causes lethal neurodegenerative diseases of mammals called transmissible spongiform encephalopathies (TSEs) (78). Most transmissible diseases are caused by the infectious form (PrP^{Sc}) of a normal cellular prion protein (PrP^{C}) (79). However, the revolutionary concept of prion was not limited to mammals; many proteins in yeast and fungus also show the prion behaviour. The discovery of yeast prions provides a broader definition to prion then just an infectious agent of TSEs. The well-characterized fungal prion proteins are Sup35, Ure2, Rnq1 in *Saccharomyces cerevisiae* and HET-s in filamentous fungus *Podospora anserine* (80). The conformational conversion of these proteins into prion state affects the protein's function and the associated cell phenotypes. The prion-based phenotypes are propagated from generation to generation through the transmission of prion form of protein. Therefore, yeast prions are considered as epigenetic modifiers which change the biological phenotype without affecting the genetic material (80).

Sup35 is a translation termination factor which recognizes the stop codon during protein synthesis. The conversion of soluble form of Sup35 into its aggregated state, [PSI^{+}], causes the read-through of the stop codon and reveals new biological phenotypes (81). Ure2 is a suppressor of Gln3 (a transcription factor) and represses the genes involved in the utilization of poor sources of nitrogen when rich sources are available. When Ure2 is converted to its prion state, [URE3], it causes the synthesis of proteins related to uptake of poor nitrogen sources (82). Rnq1 protein function is not known and when present in the prion state, [RNQ^{+}], it influences the rate of appearance of other prions (83). The prion state, [HET-s], of protein is involved in heterokaryon incompatibility, a phenomenon of self-recognition and prevents the fusion of fungal strains with genetic incompatibility (84). Recently, many new prions have been identified which includes [SWI^{+}], [$MOT3^{+}$], [MCA], [OCT^{+}], [MOD^{+}] and several other proteins may have prion-like properties in *S. cerevisiae, Schizosaccharomyces pombe* and *P. Anserine* (85). Further genome-wide analysis based on similar sequence composition suggest many new potential prions in yeast and other organisms (86, 87).

1.5.1 Genetic criteria for a yeast prion

1.5.1.1 Reversible curability

If a prion is cured, it can reappear *de novo* in a population at some low frequency because the gene encoding the protein is still present in the cell. On the contrary, curing of nucleic acids such as viruses and plasmids is an irreversible event. Once lost, it cannot arise spontaneously in a population from which it was cured (Fig. 1.3).

1.5.1.2 Overproduction of prion protein induces prion appearance

Overexpression of a prion protein in a cell increases the potential for the spontaneous appearance of prion form. Once the change has occurred in a cell, their autocatalytic activity converts all the molecules into prion form comprising amyloids. In contrast, overexpression of a chromosomally encoded replication factors such as polymerase of a plasmid or virus would not be expected to induce the spontaneous appearance of nucleic acid replicon (Fig. 1.3).

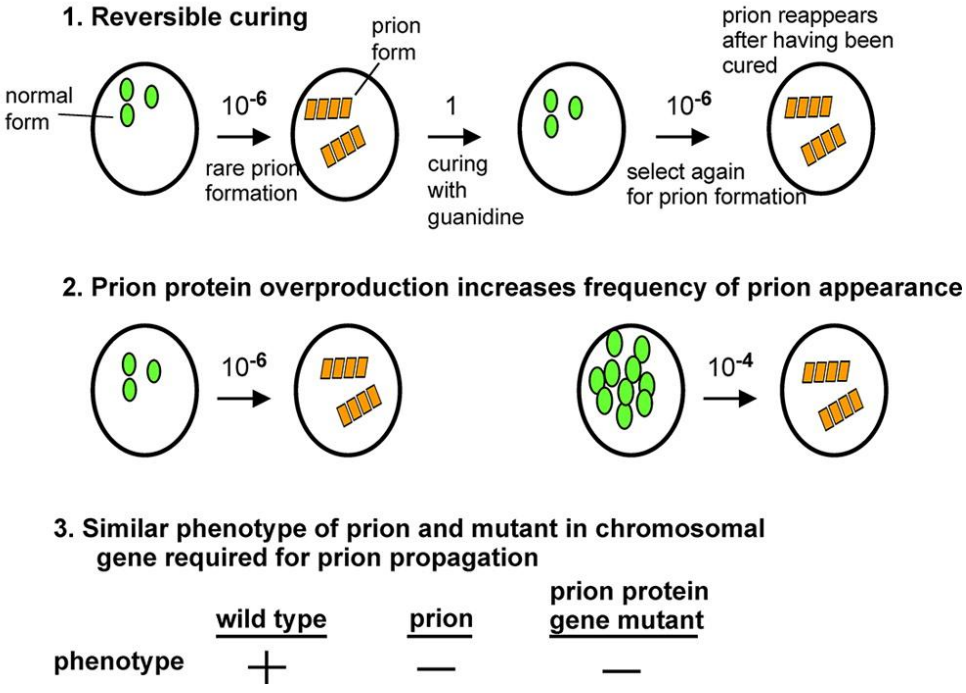

Figure 1.3 Genetic criteria for a prion. Republish with permission from Ref. (88).

1.5.1.3 Prion often mimics loss of function phenotype

Conversion of normal cellular protein into the prion form compromise the functioning of a protein and generate new phenotypes. For example, the conversion of cellular Sup35, a translational termination factor, into prion form causes the decrease in translation termination

activity (loss of function) resulting in read-through of stop codons in cells. Therefore, either incorporation of mutations or formation of prion form leads to inactivation of the gene and read-through phenotype (Fig. 1.3).

1.5.1.4 Non-Mendelian pattern of prions inheritance

Since, prion aggregates are located in cytoplasm and can efficiently convert the non-prion form into the prion conformation, prion phenotypes are dominant and inherited with significant efficiency to all the meiotic progeny. Prions can transfer by cytoduction also which involves the cytoplasmic fusion without nuclear fusion.

1.5.2 Prion Domains

Yeast prion proteins contain regions that are essential and sufficient for the formation and propagation of prion state and can preserve the prion state without full-length protein. These domains are termed as prion domains (PrDs) (89). Ure2p regulates the expression of enzymes and transporters required for the utilization of poor nitrogen sources when rich sources of nitrogen are available (90). The [URE3] prion is induced by the overproduction of N-terminal 65 residues of Ure2p (91), and is sufficient to propagate [URE3] prion in the absence of remainder of the molecule (92). Sup35p is a translation termination factor and residues 1 to 114 (Sup35N) are sufficient for the propagation of [*PSI*$^{+}$] phenotype (93). However, these domains are not only involved in prion propagation but also in many other functions. For example, the Ure2p prion domain enhances the protein stability *in vivo,* (94) and the Sup35p prion domain interacts with the polyA binding proteins and regulates general mRNA turnover systems (95). Generally, yeast prion domains are intrinsically disordered and QN-rich with an exception of Mod5p prion domain (96). Typically, they are rich in N than Q and minimal prion domain may not contain Qs (97). Moreover, the substitution of Qs to Ns increases the prion propagation whereas substituting Ns for Qs decreases the prion propagation (98).

1.5.3 Yeast Prion [*PSI*$^{+}$]

[*PSI*$^{+}$] prion in yeast is well-characterized and formed by a switch of soluble functional Sup35p into non-functional amyloid fibrils (99, 100). The presence of [*PSI*$^{+}$] prion reduces the concentration of soluble Sup35 and causes the read-through of the stop codon. This increase in non-sense suppression creates a host of new phenotypes (101). The presence of [*PSI*$^{+}$] determinant can be detected by the suppression of non-sense mutation in ADE1gene (Ade1-14) (102). The presence of non-sense mutation blocks the adenine biosynthesis

pathway and causes the accumulation of an intermediate product which upon oxidation gives rise to red pigment. In [*psi*$^{-}$] cells that have functional Sup35, the stop codon is not suppressed causing the accumulation of red pigment in the cells (Fig. 1.4). On the contrary, in [*PSI*$^{+}$] cells where Sup35 is sequestered in the amyloid form, stop codon is read-through causing the synthesis of functional Ade2 enzyme and giving normal white color to the colonies (Fig. 1.4) (102). *In vivo* studies with Sup35 fused to GFP suggest that in [*psi*$^{-}$] cells fluorescence was diffusely distributed whereas in [*PSI*$^{+}$] cells, fluorescence was concentrated in a small number of intense foci (Fig. 1.4) (103).

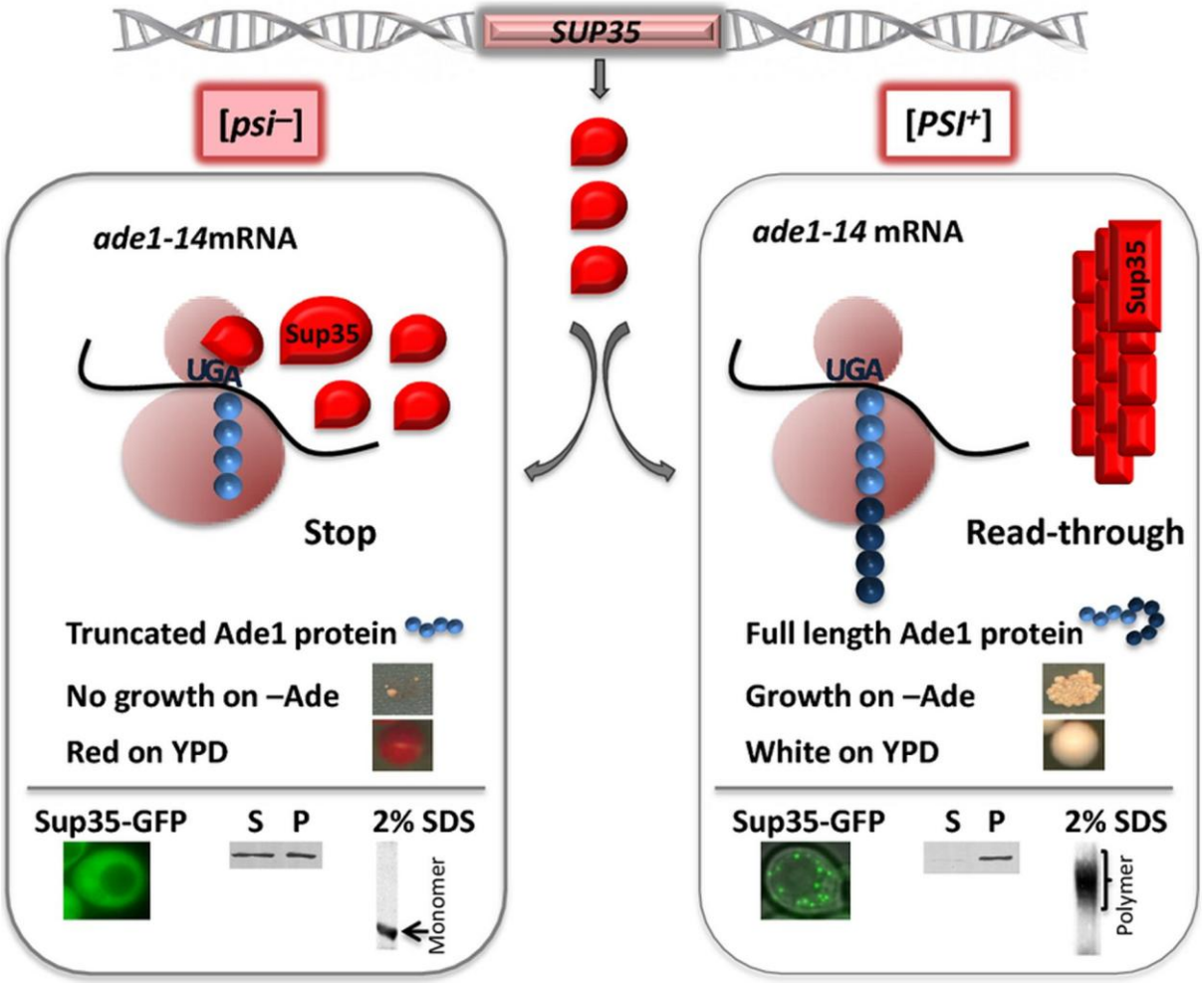

Figure 1.4 Detection of [*PSI*$^{+}$] prion state by introducing a nonsense mutation in the ADE1 gene of Adenine biosynthetic pathway. The [*psi*$^{-}$] cells with stop codon (UGA) mutation fails to grow in a medium lacking adenine and show red color colonies in YPD medium. In [*PSI*$^{+}$] cells, Sup35p being present in the amyloid state, fails to recognize the stop codon, resulting in complete synthesis of Ade1 protein and show growth in medium lacking adenine and form white color colonies on YPD medium. Reproduced with permission from Ref. (104).

Sup35p consists of three structural domains: N-terminal domain (N, residues 1-123), middle domain (M, residues124-253) and C-terminal domain (C, residues 254-685). The N domain is Q/N rich (residues 1-40) and contains a region of 5.5 imperfect oligopeptide repeats (ORs) between residue positions 41 and 97. It is responsible for both prion induction and maintenance (105, 106). The M domain is rich in positively charged residues (K/E) (107) and maintains the solubility of non-prion form of Sup35 and is sufficient along with the N domain (SupNM domain) for prion-based inheritance. The C domain is essential and sufficient for translation termination (106, 108).

1.5.4 Prion strain diversity

Variants/ strains of [*PSI*$^+$] prion were initially recognized based on the genetic analysis. The overexpression of Sup35 in yeast cells induces the appearance of [*PSI*$^+$] phenotypes that display a distinct level of nonsense suppression (105). These phenotypic variants were named based on the strength of read-through of the stop codon and the stability of mitotic inheritance. Strong variant of [*PSI*$^+$] display high level of nonsense (allele ade2-1 or ade1-14) suppression and show white color colonies whereas weak variant of [*PSI*$^+$] show lower efficiency of nonsense suppression resulting in the accumulation of red pigment and forming pink color colonies (Fig. 1.5 *a*). When cells carrying strong and weak variants of [*PSI*$^+$] are mated, the meiotic progenies have strong [*PSI*$^+$] phenotype suggesting that strong variants propagate more efficiently than the weak [*PSI*$^+$] variant (109). The differences in the suppression efficiency correlate inversely with the levels of soluble Sup35. Therefore, the strong [*PSI*$^+$] variant has very small amount of soluble Sup35, whereas the weak variant has increased pool of soluble Sup35 (110). *In vivo* studies using GFP-tagged Sup35NM indicate that strong [*PSI*$^+$] cells have many more punctate fluorescent foci than the weak [*PSI*$^+$] cells (111). The separation of lysates by centrifugation into supernatant (S) and pellet (P) fractions indicate more soluble (and functional) Sup35 available in weak *vs.* strong [*PSI*$^+$] cells (Fig. 1.5 *b*). Furthermore, the size of aggregates in different variants were confirmed and it appears that the strong [*PSI*$^+$] variant exhibit smaller aggregates compared to the weak [*PSI*$^+$] strains which have comparatively larger aggregates (Fig. 1.5 *c*) (112). The differences in strains can be due to different amyloid properties of Sup35 that are likely to determine the amount of soluble Sup35 within the cell.

Further insights into the molecular basis of yeast prion 'variants' came from *in vitro* studies which show that Sup35NM can form different types of amyloid fibrils that can be faithfully propagated *in vitro* (113). Later on, amyloid fibrils of Sup35NM were formed at

different temperatures to generate distinct amyloid conformations. Amyloid fibrils formed at 4 °C was found to have distinct molecular structure compared to fibrils formed at 23 °C or 37 °C (114). The amyloid core in 4 °C fibrils is shorter and thermodynamically less stable than fibrils formed at 37 °C (115, 116). Interestingly, when introduced into yeast cells, 4 °C fibrils (Sc4) show strong [*PSI*$^{+}$] phenotype, whereas 37 °C fibrils (Sc37) show weak [*PSI*$^{+}$] phenotype (114, 116). The Sc4 conformation is physically less stable and hence is efficiently broken by chaperone machinery providing new seeds for templating the soluble pool of Sup35. Whereas, Sc37 conformation is structurally strong and has less severing efficiency that decreases the number of free ends for further polymerization of soluble Sup35 making it weak [*PSI*$^{+}$] phenotype (117).

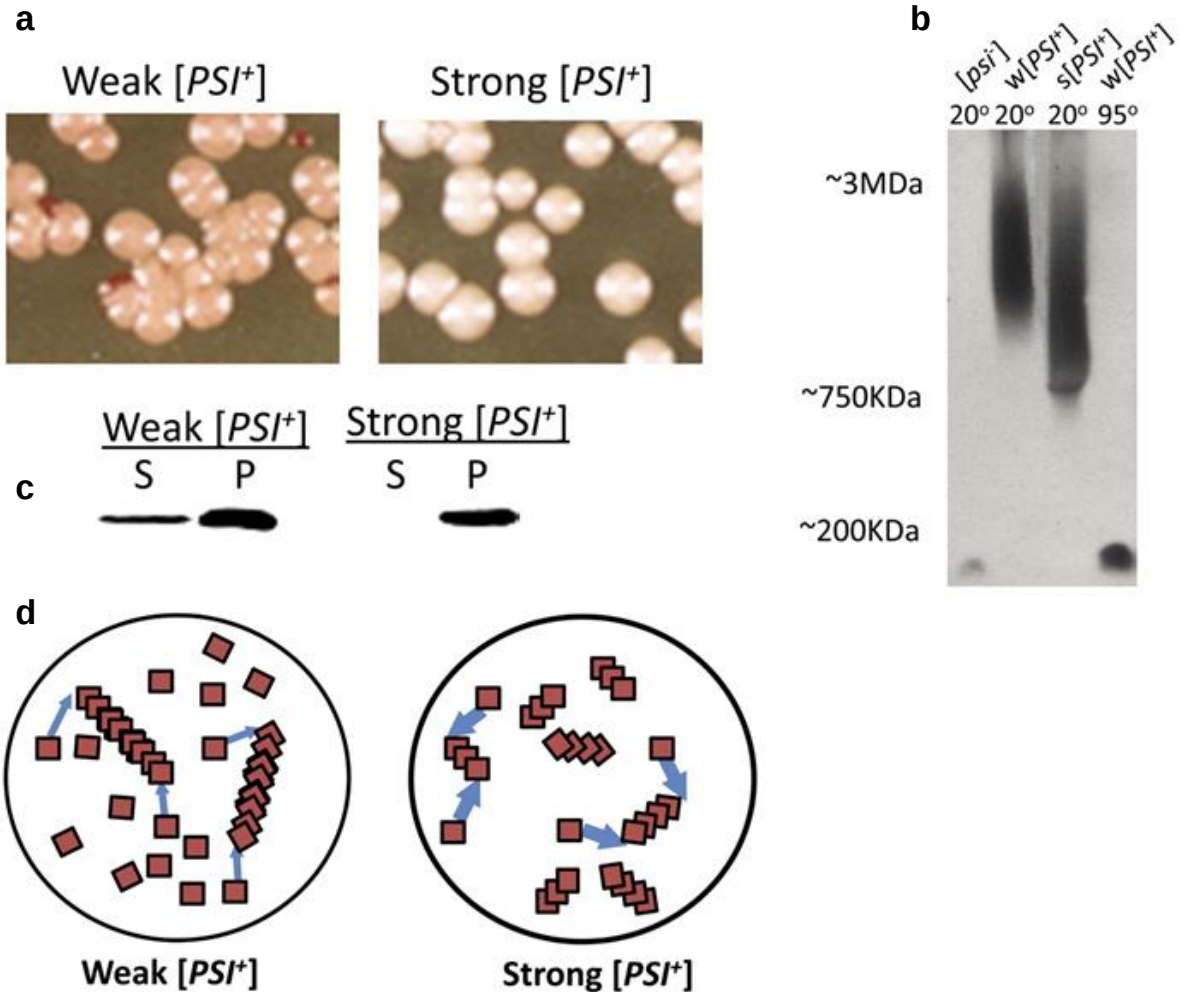

Figure 1.5 Differences between strong and weak strains of [*PSI*$^{+}$] prion. (*a*) Weak strain has light pink color colonies, whereas the strong strain has white color colonies. (*b*) Lysate of weak strain has higher molecular weight aggregates compared to strong strain. (*c*) Most of the Sup35 comes in the pellet fraction in strong strain compared to weak strain. (*d*) Schematic showing the differences in number of free ends available in amyloid fibrils for templating the newly synthesized soluble Sup35 molecules in two different strains. Reproduced with permission from Ref. (96).

1.5.5 Effect of Hsp104 in prion propagation

Interestingly, *in vitro* formation and propagation of amyloid state of yeast prion proteins do not require the assistance of any other cofactors and chaperones but *in vivo* propagation of yeast prions involves the chaperone machinery. For example, [*PSI*$^+$] prion is propagated by the Hsp104 chaperone, a homohexameric AAA ATPase (118). The deletion of HSP104 eliminates [*PSI*$^+$] prion (96). HSp104 is essential for propagation of other yeast prions as well (119) with a few exceptions such as [ISP$^+$] (120). Besides Hsp104, many other chaperones are involved in yeast prion propagation including Hsp70 and Hsp40 (121). The increase in the size of Sup35 aggregates when Hsp104 activity was decreased (122) suggest that the Hsp104 help in fragmentation of amyloid fibril into smaller seeds which provide new free ends for monomer conversion into amyloid state (123, 124). During cell division, these fibrillar seeds are delivered from the mother to daughter cells to propagate the [*PSI*$^+$] prion phenotype. Therefore, the efficiency of chaperone activity is important for fibril fragmentation and propagation. The differences in physical properties of amyloid fibrils affect the chaperone activity and explain the phenotypic differences between prion variants (125). Fibrils of strong [*PSI*$^+$] strain are readily fragmented and therefore, produce a larger number of prion units per cell. The presence of more free termini for association with new proteins results in more efficient utilization of soluble Sup35. On the contrary, thermodynamically more stable fibrils of weak [*PSI*$^+$] prion are less prone for Hsp104 fragmentation resulting in fewer fibril ends and less conversion rate of newly synthesized Sup35 protein molecules. This also explains the presence of large soluble pool of Sup35 (110, 126) and higher molecular weight aggregate in weak strain (112) . The presence of soluble Sup35 in weak strain prevents the read-through of stop codon to some extent giving a light pink color to the colonies as compared to white color colonies observed in strong variant (105).

1.5.6 Structural features of Sup35 amyloid

Based on different methodologies, two distinct models of Sup35NM fibrils were proposed. One important model proposed is the in-register parallel β-sheet (Fig. 1.6 *a*) (127-129). According to this model, the identical residues of different molecules are aligned and stacked on top of each other resulting in one molecule per 4.7 Å in the axial direction. Various line of evidences support this model. First, mass-per-unit-length measurements of amyloid fibril formed from a fragment of NM (residues 1-61) indicate about one molecule per 4.7 Å as predicted by the stacked architecture of β-sheets in parallel in-register model (130, 131).

Second, the scrambling of amino acid sequence of Sup35 prion domain in various ways did not inhibit their prion-forming ability and strain diversity (132). This can only be possible if identical residues stack upon each other irrespective of the identity of neighbouring residues. These observations favoring the in-register parallel β-sheet model was further supported by solid-state NMR data. In these studies, four different amino acid (tyrosine, leucine, alanine and phenylalanine) residues were separately ^{13}C labeled and the intermolecular distance between labeled residues was measured. For a parallel in-register β-sheet, this measurement should be 4.7 Å as the distance between two residues in a sheet is 4.7 Å and for other types of β-sheet model, it should be larger. Most of the residues studied using solid-state NMR showed the intermolecular distance ~ 4.7 Å which is in accordance with the parallel in-register model (127-129, 133).

Another important model proposed for Sup35NM amyloid structure is β-helix (Fig. 1.6 *b*) (134, 135). This model gains some insight from the structure of globular β-helical proteins (134, 136). Each rung of a β-helix is made up of approximately 10 to 20 residues and contains a central pore which prevents the inter-β stand interactions among the β-sheets. Based on this model, two predictions can be made about the fibril structure: first, the amyloid core should be long enough to form more than two rung so that residues in the centre of a core will not make intermolecular contacts. Second, there should not be any 8–10-Å reflection in the X-ray diffraction pattern, because β-sheets parallel to the fibrils axis are not in close contact (137).

This model of Sup35NM fibril was supported by two different studies (135, 138). In one of the report, they showed that the x-ray fibre diffraction pattern of hydrated fibrils has only meridional reflection at 4.7 Å but no equatorial reflection at 9 Å which was contradictory to the observation in dry fibrils that indicates the presence of both patterns. This observation supports that the β-helix is the likely structure of Sup35NM fibrils (138). In another report, they created 37 single cysteine mutations throughout the NM sequence (135). These mutations did not affect the *in vitro* fibrillation kinetics and *in vivo* prion propagation. To determine the length of the amyloid core, they labeled the cysteine residues with environment-sensitive acrylodan dye and found that the solvent-protected amyloid core encompasses the most of the N domain (residues 21–121). However, in a different approach in which they check the labelling efficiencies of cysteine residues after amyloid formation revealed a smaller amyloid core which includes residues from 2–73. Interestingly, this discrepancy in two results could be due to the interaction of dye molecules with protein

residues during the amyloid formation which makes them more buried as compared to post-assembly labelling. Further, they labeled these single cysteine residues with pyrene, a fluorescent dye sensitive to inter-dye spacing, to detect intermolecular interactions between the protein molecules. They found that only residues located in the head (residues 20-40) and tail (residues 90-110) regions have close intermolecular contact, whereas other residues lack the intermolecular contacts which includes the intervening region (approximately residues 40–80) and the M domain. Further, they support this observation by using cysteine-reactive cross-linker probes. The cross-linking in the head and tail regions strongly favor the aggregation kinetics whereas in the intermediate region, it inhibits the aggregation kinetics indicating that only a subsets of residues in the amyloid core form the intermolecular contacts which are consistent with the β-helix model. However, most of the data obtained with cysteine mutations favors the β-helix model but the major drawback with this model is the failure to explain the faithful propagation of different strains of [PSI^{+}] prion.

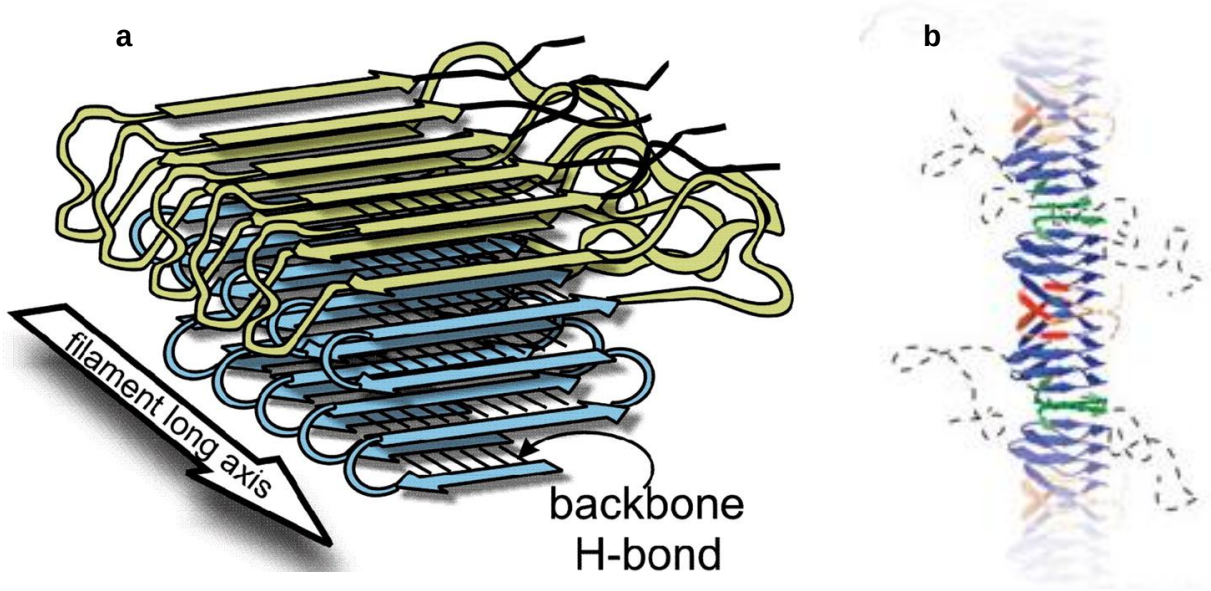

Figure 1.6 Proposed models for Sup35NM amyloid fibrils. (*a*) In-register parallel β-sheet model according to which large part of N and M domain form the stacked β-strands of β-sheets, reproduced from Ref. (127). (*b*) β-helix model according to which the residues in the N domain form the core of amyloid fibril and M domain remains unstructured. The β-strands in red (head region) and green (tail region) color form the intermolecular contacts whereas the β-strands in blue color form the intermolecular contacts. Reproduced with permission from Ref.(135).

1.6 Thesis rationale and objective

The goal of this thesis is to achieve a better understanding of mechanism of amyloid formation which involves the formation of partially structured species, oligomers and amyloid fibrils. Under certain conditions, protein can undergo structural destabilization and give rise to amyloid fibrils with a characteristic cross-β sheet structure. Further, a single polypeptide chain can give rise to amyloid fibrils with distinct structural packing at the protein level. Therefore, it is important to understand the cause of this heterogeneity and the structural differences in distinct amyloid/ prion strains.

To address these issues, I have used human β_2-microglobulin (β_2m) and yeast prion Sup35 as experimental models. Using β_2m, I have characterized the partially acid-unfolded state formed at pH 2.5 (Chapter 2) and studied the effect of change in pH on unfolding of β_2m using stopped-flow apparatus (Chapter 3). β_2m at pH 2.5 in presence of different salt concentrations give rise to amyloid fibril with distinct morphologies. In order to understand the cause of amyloid polymorphism, I have characterized the early oligomers formed in presence of different salt concentrations (Chapter 4). Using yeast prion Sup35, I have studied the structural differences in distinct strains of [*PSI*$^+$] prion (Chapter 5) and role of water in these [*PSI*$^+$] prion strains.

1.7 References

1. Kubelka J, Hofrichter J, & Eaton WA (2004) The protein folding 'speed limit'. *Current opinion in structural biology* 14(1):76-88.
2. Karplus M (1997) The Levinthal paradox: yesterday and today. *Folding and Design* 2:S69-S75.
3. Brockwell DJ & Radford SE (2007) Intermediates: ubiquitous species on folding energy landscapes? *Current opinion in structural biology* 17(1):30-37.
4. Onuchic JN & Wolynes PG (2004) Theory of protein folding. *Current opinion in structural biology* 14(1):70-75.
5. Hartl FU, Bracher A, & Hayer-Hartl M (2011) Molecular chaperones in protein folding and proteostasis. *Nature* 475(7356):324-332.
6. Chiti F & Dobson CM (2006) Protein misfolding, functional amyloid, and human disease. (Translated from eng) *Annu Rev Biochem* 75:333-366 (in eng).
7. Bolognesi B, *et al.* (2010) ANS binding reveals common features of cytotoxic amyloid species. *ACS chemical biology* 5(8):735-740.
8. Kayed R, *et al.* (2003) Common structure of soluble amyloid oligomers implies common mechanism of pathogenesis. *Science* 300(5618):486-489.
9. Sunde M, *et al.* (1997) Common core structure of amyloid fibrils by synchrotron X-ray diffraction. *Journal of molecular biology* 273(3):729-739.
10. Jiménez JL, *et al.* (2002) The protofilament structure of insulin amyloid fibrils. *Proceedings of the National Academy of Sciences* 99(14):9196-9201.
11. Astbury WT, Dickinson S, & Bailey K (1935) The X-ray interpretation of denaturation and the structure of the seed globulins. *Biochemical Journal* 29(10):2351.
12. Fitzpatrick AW, *et al.* (2013) Atomic structure and hierarchical assembly of a cross-β amyloid fibril. *Proceedings of the National Academy of Sciences* 110(14):5468-5473.
13. Sachse C, Fändrich M, & Grigorieff N (2008) Paired β-sheet structure of an Aβ (1-40) amyloid fibril revealed by electron microscopy. *Proceedings of the National Academy of Sciences* 105(21):7462-7466.
14. Wasmer C, *et al.* (2008) Amyloid fibrils of the HET-s (218–289) prion form a β solenoid with a triangular hydrophobic core. *Science* 319(5869):1523-1526.

15. Petkova AT, *et al.* (2002) A structural model for Alzheimer's β-amyloid fibrils based on experimental constraints from solid state NMR. *Proceedings of the National Academy of Sciences* 99(26):16742-16747.
16. Apostol M, *et al.* (2007) Atomic structures of amyloid cross-beta spines reveal varied steric zippers. *Nature* 447(7143):453457Selkoe.
17. Eisenberg D & Jucker M (2012) The amyloid state of proteins in human diseases. *Cell* 148(6):1188-1203.
18. Fändrich M & Dobson CM (2002) The behaviour of polyamino acids reveals an inverse side chain effect in amyloid structure formation. *The EMBO journal* 21(21):5682-5690.
19. Ritter C, *et al.* (2005) Correlation of structural elements and infectivity of the HET-s prion. (Translated from eng) *Nature* 435(7043):844-848 (in eng).
20. Williams AD, *et al.* (2004) Mapping Aβ amyloid fibril secondary structure using scanning proline mutagenesis. *Journal of molecular biology* 335(3):833-842.
21. Balbach JJ, *et al.* (2000) Amyloid fibril formation by Aβ16-22, a seven-residue fragment of the Alzheimer's β-amyloid peptide, and structural characterization by solid state NMR. *Biochemistry* 39(45):13748-13759.
22. Tycko R, Sciarretta KL, Orgel JP, & Meredith SC (2009) Evidence for novel β-sheet structures in Iowa mutant β-amyloid fibrils. *Biochemistry* 48(26):6072-6084.
23. Toyama BH & Weissman JS (2011) Amyloid structure: conformational diversity and consequences. (Translated from eng) *Annu Rev Biochem* 80:557-585 (in eng).
24. Knowles TP, Vendruscolo M, & Dobson CM (2014) The amyloid state and its association with protein misfolding diseases. *Nat Rev Mol Cell Biol* 15(6):384-396.
25. Heemels MT & Ploegh H (1995) Generation, translocation, and presentation of MHC class I-restricted peptides. (Translated from eng) *Annu Rev Biochem* 64:463-491 (in eng).
26. Paulsson KM, *et al.* (2001) Distinct differences in association of MHC class I with endoplasmic reticulum proteins in wild-type, and beta 2-microglobulin- and TAP-deficient cell lines. (Translated from eng) *Int Immunol* 13(8):1063-1073 (in eng).
27. Solheim JC (1999) Class I MHC molecules: assembly and antigen presentation. (Translated from eng) *Immunol Rev* 172:11-19 (in eng).
28. Neefjes JJ, Hammerling GJ, & Momburg F (1993) Folding and assembly of major histocompatibility complex class I heterodimers in the endoplasmic reticulum of

intact cells precedes the binding of peptide. (Translated from eng) *J Exp Med* 178(6):1971-1980 (in eng).

29. Hughes EA, Hammond C, & Cresswell P (1997) Misfolded major histocompatibility complex class I heavy chains are translocated into the cytoplasm and degraded by the proteasome. (Translated from eng) *Proc Natl Acad Sci U S A* 94(5):1896-1901 (in eng).
30. Sege K, Rask L, & Peterson PA (1981) Role of beta2-microglobulin in the intracellular processing of HLA antigens. (Translated from eng) *Biochemistry* 20(16):4523-4530 (in eng).
31. Eichner T & Radford SE (2011) Understanding the complex mechanisms of beta2-microglobulin amyloid assembly. (Translated from eng) *FEBS J* 278(20):3868-3883 (in eng).
32. Floege J, *et al.* (1991) Clearance and synthesis rates of beta 2-microglobulin in patients undergoing hemodialysis and in normal subjects. (Translated from eng) *J Lab Clin Med* 118(2):153-165 (in eng).
33. Floege J & Ketteler M (2001) beta2-microglobulin-derived amyloidosis: an update. (Translated from eng) *Kidney Int Suppl* 78:S164-171 (in eng).
34. Gejyo F, *et al.* (1985) A new form of amyloid protein associated with chronic hemodialysis was identified as beta 2-microglobulin. (Translated from eng) *Biochem Biophys Res Commun* 129(3):701-706 (in eng).
35. Morgan CJ, Gelfand M, Atreya C, & Miranker AD (2001) Kidney dialysis-associated amyloidosis: a molecular role for copper in fiber formation. *J Mol Biol* 309(2):339-345.
36. McParland VJ, *et al.* (2000) Partially unfolded states of beta(2)-microglobulin and amyloid formation in vitro. *Biochemistry* 39(30):8735-8746.
37. Yamamoto S, *et al.* (2004) Low concentrations of sodium dodecyl sulfate induce the extension of beta 2-microglobulin-related amyloid fibrils at a neutral pH. *Biochemistry* 43(34):11075-11082.
38. Yamamoto S, *et al.* (2004) Glycosaminoglycans enhance the trifluoroethanol-induced extension of beta 2-microglobulin-related amyloid fibrils at a neutral pH. *J Am Soc Nephrol* 15(1):126-133.
39. Yamaguchi K, Naiki H, & Goto Y (2006) Mechanism by which the amyloid-like fibrils of a beta 2-microglobulin fragment are induced by fluorine-substituted alcohols. *J Mol Biol* 363(1):279-288.

40. Eakin CM, Knight JD, Morgan CJ, Gelfand MA, & Miranker AD (2002) Formation of a copper specific binding site in non-native states of beta-2-microglobulin. *Biochemistry* 41(34):10646-10656.
41. Serio TR, *et al.* (2000) Nucleated conformational conversion and the replication of conformational information by a prion determinant. *Science* 289(5483):1317-1321.
42. Lee J, Culyba EK, Powers ET, & Kelly JW (2011) Amyloid-β forms fibrils by nucleated conformational conversion of oligomers. *Nature chemical biology* 7(9):602-609.
43. Zhang P, *et al.* (2010) Mouse model to study human A beta2M amyloidosis: generation of a transgenic mouse with excessive expression of human beta2-microglobulin. (Translated from eng) *Amyloid* 17(2):50-62 (in eng).
44. Valleix S, *et al.* (2012) Hereditary systemic amyloidosis due to Asp76Asn variant beta2-microglobulin. (Translated from eng) *N Engl J Med* 366(24):2276-2283 (in eng).
45. Mangione PP, *et al.* (2013) Structure, folding dynamics, and amyloidogenesis of D76N beta2-microglobulin: roles of shear flow, hydrophobic surfaces, and alpha-crystallin. (Translated from eng) *J Biol Chem* 288(43):30917-30930 (in eng).
46. Mackay JP, *et al.* (2001) The hydrophobin EAS is largely unstructured in solution and functions by forming amyloid-like structures. (Translated from eng) *Structure* 9(2):83-91 (in eng).
47. Fowler DM, *et al.* (2006) Functional amyloid formation within mammalian tissue. (Translated from eng) *PLoS Biol* 4(1):e6 (in eng).
48. Chapman MR, *et al.* (2002) Role of Escherichia coli curli operons in directing amyloid fiber formation. (Translated from eng) *Science* 295(5556):851-855 (in eng).
49. Claessen D, *et al.* (2003) A novel class of secreted hydrophobic proteins is involved in aerial hyphae formation in Streptomyces coelicolor by forming amyloid-like fibrils. (Translated from eng) *Genes Dev* 17(14):1714-1726 (in eng).
50. Iconomidou VA, Vriend G, & Hamodrakas SJ (2000) Amyloids protect the silkmoth oocyte and embryo. (Translated from eng) *FEBS Lett* 479(3):141-145 (in eng).
51. Uptain SM & Lindquist S (2002) Prions as protein-based genetic elements. (Translated from eng) *Annu Rev Microbiol* 56:703-741 (in eng).
52. Coustou V, Deleu C, Saupe S, & Begueret J (1997) The protein product of the het-s heterokaryon incompatibility gene of the fungus Podospora anserina behaves as a

prion analog. (Translated from eng) *Proc Natl Acad Sci U S A* 94(18):9773-9778 (in eng).

53. Butko P, *et al.* (2001) Spectroscopic evidence for amyloid-like interfacial self-assembly of hydrophobin Sc3. (Translated from eng) *Biochem Biophys Res Commun* 280(1):212-215 (in eng).
54. King CY, *et al.* (1997) Prion-inducing domain 2-114 of yeast Sup35 protein transforms in vitro into amyloid-like filaments. (Translated from eng) *Proc Natl Acad Sci U S A* 94(13):6618-6622 (in eng).
55. Suzuki G, Shimazu N, & Tanaka M (2012) A yeast prion, Mod5, promotes acquired drug resistance and cell survival under environmental stress. (Translated from eng) *Science* 336(6079):355-359 (in eng).
56. Si K, Lindquist S, & Kandel ER (2003) A neuronal isoform of the aplysia CPEB has prion-like properties. (Translated from eng) *Cell* 115(7):879-891 (in eng).
57. Si K, Choi YB, White-Grindley E, Majumdar A, & Kandel ER (2010) Aplysia CPEB can form prion-like multimers in sensory neurons that contribute to long-term facilitation. (Translated from eng) *Cell* 140(3):421-435 (in eng).
58. Barnhart MM & Chapman MR (2006) Curli biogenesis and function. (Translated from eng) *Annu Rev Microbiol* 60:131-147 (in eng).
59. Cherny I, *et al.* (2005) The formation of Escherichia coli curli amyloid fibrils is mediated by prion-like peptide repeats. (Translated from eng) *J Mol Biol* 352(2):245-252 (in eng).
60. Podrabsky JE, Carpenter JF, & Hand SC (2001) Survival of water stress in annual fish embryos: dehydration avoidance and egg envelope amyloid fibers. (Translated from eng) *Am J Physiol Regul Integr Comp Physiol* 280(1):R123-131 (in eng).
61. Iconomidou VA, *et al.* (2006) Amyloid fibril formation propensity is inherent into the hexapeptide tandemly repeating sequence of the central domain of silkmoth chorion proteins of the A-family. (Translated from eng) *J Struct Biol* 156(3):480-488 (in eng).
62. True HL, Berlin I, & Lindquist SL (2004) Epigenetic regulation of translation reveals hidden genetic variation to produce complex traits. (Translated from eng) *Nature* 431(7005):184-187 (in eng).
63. Chien P, Weissman JS, & DePace AH (2004) Emerging principles of conformation-based prion inheritance. (Translated from eng) *Annu Rev Biochem* 73:617-656 (in eng).

64. Sondheimer N & Lindquist S (2000) Rnq1: an epigenetic modifier of protein function in yeast. (Translated from eng) *Mol Cell* 5(1):163-172 (in eng).
65. Shorter J & Lindquist S (2005) Prions as adaptive conduits of memory and inheritance. (Translated from eng) *Nat Rev Genet* 6(6):435-450 (in eng).
66. Taylor KL, Cheng N, Williams RW, Steven AC, & Wickner RB (1999) Prion domain initiation of amyloid formation in vitro from native Ure2p. (Translated from eng) *Science* 283(5406):1339-1343 (in eng).
67. Baxa U, *et al.* (2005) Filaments of the Ure2p prion protein have a cross-beta core structure. (Translated from eng) *J Struct Biol* 150(2):170-179 (in eng).
68. Lian HY, Jiang Y, Zhang H, Jones GW, & Perrett S (2006) The yeast prion protein Ure2: structure, function and folding. (Translated from eng) *Biochim Biophys Acta* 1764(3):535-545 (in eng).
69. Dos Reis S, *et al.* (2002) The HET-s prion protein of the filamentous fungus Podospora anserina aggregates in vitro into amyloid-like fibrils. (Translated from eng) *J Biol Chem* 277(8):5703-5706 (in eng).
70. Balguerie A, *et al.* (2003) Domain organization and structure-function relationship of the HET-s prion protein of Podospora anserina. (Translated from eng) *EMBO J* 22(9):2071-2081 (in eng).
71. Dalstra HJ, *et al.* (2005) Non-mendelian inheritance of the HET-s prion or HET-s prion domains determines the het-S spore killing system in Podospora anserina. (Translated from eng) *Fungal Genet Biol* 42(10):836-847 (in eng).
72. Berson JF, Harper DC, Tenza D, Raposo G, & Marks MS (2001) Pmel17 initiates premelanosome morphogenesis within multivesicular bodies. (Translated from eng) *Mol Biol Cell* 12(11):3451-3464 (in eng).
73. Maji SK, *et al.* (2009) Functional amyloids as natural storage of peptide hormones in pituitary secretory granules. (Translated from eng) *Science* 325(5938):328-332 (in eng).
74. Theos AC, Truschel ST, Raposo G, & Marks MS (2005) The Silver locus product Pmel17/gp100/Silv/ME20: controversial in name and in function. (Translated from eng) *Pigment Cell Res* 18(5):322-336 (in eng).
75. Berson JF, *et al.* (2003) Proprotein convertase cleavage liberates a fibrillogenic fragment of a resident glycoprotein to initiate melanosome biogenesis. (Translated from eng) *J Cell Biol* 161(3):521-533 (in eng).

76. Fowler DM, Koulov AV, Balch WE, & Kelly JW (2007) Functional amyloid--from bacteria to humans. (Translated from eng) *Trends Biochem Sci* 32(5):217-224 (in eng).
77. Dannies PS (2001) Concentrating hormones into secretory granules: layers of control. (Translated from eng) *Mol Cell Endocrinol* 177(1-2):87-93 (in eng).
78. Prusiner SB (1982) Novel proteinaceous infectious particles cause scrapie. *Science* 216(4542):136-144.
79. Prusiner SB (1998) Prions. *Proceedings of the National Academy of Sciences* 95(23):13363-13383.
80. Uptain SM & Lindquist S (2002) Prions as protein-based genetic elements. *Annual Reviews in Microbiology* 56(1):703-741.
81. Wickner RB, Masison DC, & Edskes HK (1995) [PSI] and [URE3] as yeast prions. *Yeast* 11(16):1671-1685.
82. Wickner RB (1994) [URE3] as an altered URE2 protein: evidence for a prion analog in Saccharomyces cerevisiae. *Science* 264(5158):566-569.
83. Derkatch IL, *et al.* (2000) Dependence and independence of [PSI+] and [PIN+]: a two-prion system in yeast? *The EMBO journal* 19(9):1942-1952.
84. Coustou V, Deleu C, Saupe S, & Begueret J (1997) The protein product of the het-s heterokaryon incompatibility gene of the fungus Podospora anserina behaves as a prion analog. *Proceedings of the National Academy of Sciences* 94(18):9773-9778.
85. Tessier PM & Lindquist S (2009) Unraveling infectious structures, strain variants and species barriers for the yeast prion [PSI+]. *Nature structural & molecular biology* 16(6):598-605.
86. Michelitsch MD & Weissman JS (2000) A census of glutamine/asparagine-rich regions: implications for their conserved function and the prediction of novel prions. *Proceedings of the National Academy of Sciences* 97(22):11910-11915.
87. Alberti S, Halfmann R, King O, Kapila A, & Lindquist S (2009) A systematic survey identifies prions and illuminates sequence features of prionogenic proteins. *Cell* 137(1):146-158.
88. Wickner RB, *et al.* (2013) Amyloids and yeast prion biology. *Biochemistry* 52(9):1514-1527.
89. Ross ED, Minton A, & Wickner RB (2005) Prion domains: sequences, structures and interactions. *Nature cell biology* 7(11):1039-1044.

90. Magasanik B & Kaiser CA (2002) Nitrogen regulation in Saccharomycescerevisiae. *Gene* 290(1):1-18.
91. Masison DC & Wickner RB (1995) Prion-inducing domain of yeast Ure2p and protease resistance of Ure2p in prion-containing cells. *Science* 270(5233):93-95.
92. Masison DC, Maddelein M-L, & Wickner RB (1997) The prion model for [URE3] of yeast: spontaneous generation and requirements for propagation. *Proceedings of the National Academy of Sciences* 94(23):12503-12508.
93. Ter-Avanesyan MD, Dagkesamanskaya AR, Kushnirov VV, & Smirnov VN (1994) The SUP35 omnipotent suppressor gene is involved in the maintenance of the non-Mendelian determinant [psi+] in the yeast Saccharomyces cerevisiae. *Genetics* 137(3):671-676.
94. Shewmaker F, Mull L, Nakayashiki T, Masison DC, & Wickner RB (2007) Ure2p function is enhanced by its prion domain in Saccharomyces cerevisiae. *Genetics* 176(3):1557-1565.
95. Kobayashi T, Funakoshi Y, Hoshino S-i, & Katada T (2004) The GTP-binding release factor eRF3 as a key mediator coupling translation termination to mRNA decay. *Journal of Biological Chemistry* 279(44):45693-45700.
96. Liebman SW & Chernoff YO (2012) Prions in yeast. (Translated from eng) *Genetics* 191(4):1041-1072 (in eng).
97. Crow ET, Du Z, & Li L (2011) A small, glutamine-free domain propagates the [SWI+] prion in budding yeast. *Molecular and cellular biology* 31(16):3436-3444.
98. Halfmann R, *et al.* (2011) Opposing effects of glutamine and asparagine govern prion formation by intrinsically disordered proteins. *Molecular cell* 43(1):72-84.
99. Paushkin SV, Kushnirov VV, Smirnov VN, & Ter-Avanesyan MD (1997) In vitro propagation of the prion-like state of yeast Sup35 protein. *Science* 277(5324):381-383.
100. Glover JR, *et al.* (1997) Self-seeded fibers formed by Sup35, the protein determinant of [PSI+], a heritable prion-like factor of S. cerevisiae. *Cell* 89(5):811-819.
101. True HL & Lindquist SL (2000) A yeast prion provides a mechanism for genetic variation and phenotypic diversity. *Nature* 407(6803):477-483.
102. Tuite MF & Cox BS (2003) Propagation of yeast prions. *Nature Reviews Molecular Cell Biology* 4(11):878-890.
103. Patino MM, Liu J-J, Glover JR, & Lindquist S (1996) Support for the prion hypothesis for inheritance of a phenotypic trait in yeast. *Science* 273(5275):622-626.

104. Chernova TA, Wilkinson KD, & Chernoff YO (2014) Physiological and environmental control of yeast prions. *FEMS microbiology reviews* 38(2):326-344.

105. Derkatch IL, Chernoff YO, Kushnirov VV, Inge-Vechtomov SG, & Liebman SW (1996) Genesis and variability of [PSI] prion factors in Saccharomyces cerevisiae. *Genetics* 144(4):1375-1386.

106. Ter-Avanesyan MD, Dagkesamanskaya AR, Kushnirov VV, & Smirnov VN (1994) The SUP35 omnipotent suppressor gene is involved in the maintenance of the non-Mendelian determinant [psi+] in the yeast Saccharomyces cerevisiae. *Genetics* 137(3):671-676.

107. Liu JJ, Sondheimer N, & Lindquist SL (2002) Changes in the middle region of Sup35 profoundly alter the nature of epigenetic inheritance for the yeast prion [PSI+]. *Proceedings of the National Academy of Sciences of the United States of America* 99 Suppl 4:16446-16453.

108. Ter-Avanesyan MD*, et al.* (1993) Deletion analysis of the SUP35 gene of the yeast Saccharomyces cerevisiae reveals two non-overlapping functional regions in the encoded protein. *Molecular microbiology* 7(5):683-692.

109. Bradley ME, Edskes HK, Hong JY, Wickner RB, & Liebman SW (2002) Interactions among prions and prion "strains" in yeast. *Proceedings of the National Academy of Sciences* 99(suppl 4):16392-16399.

110. Zhou P*, et al.* (1999) The yeast non-Mendelian factor [ETA+] is a variant of [PSI+], a prion-like form of release factor eRF3. *The EMBO journal* 18(5):1182-1191.

111. Derkatch IL, Bradley ME, Zhou P, & Liebman SW (1999) The PNM2 mutation in the prion protein domain of SUP35 has distinct effects on different variants of the [PSI+] prion in yeast. *Current genetics* 35(2):59-67.

112. Kryndushkin DS, Alexandrov IM, Ter-Avanesyan MD, & Kushnirov VV (2003) Yeast [PSI+] prion aggregates are formed by small Sup35 polymers fragmented by Hsp104. *Journal of Biological Chemistry* 278(49):49636-49643.

113. Glover JR*, et al.* (1997) Self-seeded fibers formed by Sup35, the protein determinant of [PSI+], a heritable prion-like factor of S. cerevisiae. *Cell* 89(5):811-819.

114. Tanaka M, Chien P, Naber N, Cooke R, & Weissman JS (2004) Conformational variations in an infectious protein determine prion strain differences. *Nature* 428(6980):323-328.

115. Krishnan R & Lindquist SL (2005) Structural insights into a yeast prion illuminate nucleation and strain diversity. *Nature* 435(7043):765-772.
116. Toyama BH, Kelly MJS, Gross JD, & Weissman JS (2007) The structural basis of yeast prion strain variants. *Nature* 449(7159):233-237.
117. Tanaka M, Collins SR, Toyama BH, & Weissman JS (2006) The physical basis of how prion conformations determine strain phenotypes. *Nature* 442(7102):585-589.
118. Chernoff YO, Lindquist SL, Ono B-i, Inge-Vechtomov SG, & Liebman SW (1995) Role of the chaperone protein Hsp104 in propagation of the yeast prion-like factor [psi+]. *Science* 268(5212):880-884.
119. Rikhvanov E, Romanova N, & Chernoff Y (Chaperone effects on prion and nonprion aggregates. Prion 2007; 1: 217-222. (Taylor & Francis Online).
120. Rogoza T, *et al.* (2010) Non-Mendelian determinant [ISP+] in yeast is a nuclear-residing prion form of the global transcriptional regulator Sfp1. *Proceedings of the National Academy of Sciences* 107(23):10573-10577.
121. Reidy M & Masison DC (2011) Modulation and elimination of yeast prions by protein chaperones and co-chaperones. *Prion* 5(4):245-249.
122. Wegrzyn RD, Bapat K, Newnam GP, Zink AD, & Chernoff YO (2001) Mechanism of prion loss after Hsp104 inactivation in yeast. *Molecular and cellular biology* 21(14):4656-4669.
123. Paushkin S, Kushnirov V, Smirnov V, & Ter-Avanesyan M (1996) Propagation of the yeast prion-like [psi+] determinant is mediated by oligomerization of the SUP35-encoded polypeptide chain release factor. *The EMBO journal* 15(12):3127.
124. Kushnirov VV & Ter-Avanesyan MD (1998) Structure and replication of yeast prions. *Cell* 94(1):13-16.
125. Tanaka M, Collins SR, Toyama BH, & Weissman JS (2006) The physical basis of how prion conformations determine strain phenotypes. *Nature* 442(7102):585-589.
126. Uptain SM, Sawicki GJ, Caughey B, & Lindquist S (2001) Strains of [PSI+] are distinguished by their efficiencies of prion-mediated conformational conversion. *The EMBO journal* 20(22):6236-6245.
127. Shewmaker F, Wickner RB, & Tycko R (2006) Amyloid of the prion domain of Sup35p has an in-register parallel β-sheet structure. *Proceedings of the National Academy of Sciences* 103(52):19754-19759.

128. Shewmaker F, Ross ED, Tycko R, & Wickner RB (2008) Amyloids of Shuffled Prion Domains That Form Prions Have a Parallel In-Register β-Sheet Structure†. *Biochemistry* 47(13):4000-4007.
129. Shewmaker F, Kryndushkin D, Chen B, Tycko R, & Wickner RB (2009) Two prion variants of Sup35p have in-register parallel β-sheet structures, independent of hydration. *Biochemistry* 48(23):5074-5082.
130. Diaz-Avalos R, King C-Y, Wall J, Simon M, & Caspar DL (2005) Strain-specific morphologies of yeast prion amyloid fibrils. *Proceedings of the National Academy of Sciences of the United States of America* 102(29):10165-10170.
131. Chen B, Thurber KR, Shewmaker F, Wickner RB, & Tycko R (2009) Measurement of amyloid fibril mass-per-length by tilted-beam transmission electron microscopy. *Proceedings of the National Academy of Sciences* 106(34):14339-14344.
132. Ross ED, Edskes HK, Terry MJ, & Wickner RB (2005) Primary sequence independence for prion formation. *Proceedings of the National Academy of Sciences of the United States of America* 102(36):12825-12830.
133. Wickner RB, Shewmaker F, Kryndushkin D, & Edskes HK (2008) Protein inheritance (prions) based on parallel in-register β-sheet amyloid structures. *Bioessays* 30(10):955-964.
134. Wetzel R (2002) Ideas of order for amyloid fibril structure. *Structure* 10(8):1031-1036.
135. Krishnan R & Lindquist SL (2005) Structural insights into a yeast prion illuminate nucleation and strain diversity. *Nature* 435(7043):765-772.
136. Yoder M & Jurnak F (1995) Protein motifs. 3. The parallel beta helix and other coiled folds. *The FASEB journal* 9(5):335-342.
137. Tessier PM & Lindquist S (2009) Unraveling infectious structures, strain variants and species barriers for the yeast prion [PSI+]. (Translated from eng) *Nat Struct Mol Biol* 16(6):598-605 (in eng).
138. Kishimoto A, *et al.* (2004) β-Helix is a likely core structure of yeast prion Sup35 amyloid fibers. *Biochemical and biophysical research communications* 315(3):739-745.

Dynamics and dimension of an amyloidogenic disordered state of human β_2-microglobulin

This work has been published in *European Biophysical Journal*

Reference: **Narang D**, Sharma PK, and Mukhopadhyay S (2013) Dynamics and dimension of an amyloidogenic disordered state of human β_2-microglobulin. *Eur Biophys J* 42: 767-776.

2.1 Introduction

Protein misfolding, aggregation and amyloid fibril formation are associated with a number of human disorders that include Alzheimer's, Parkinson's, Huntington's and prion diseases as well as type Π diabetes and dialysis related amyloidosis (1-5). In order to understand the molecular mechanism of amyloidogenesis, it is important to characterize the conformational behavior of the early monomeric state of amyloidogenic proteins that serve as precursor to toxic amyloids. Various studies on amyloidogenic proteins have indicated that the presence of intrinsically disordered or partially unfolded structure in the polypeptide chains play a pivotal role in initiating the process of amyloid assembly (6-12). There is an emerging consensus that the conformational properties of amyloidogenic disordered polypeptides are in sharp contrast to that of archetypal denatured state of proteins found in high concentration of chemical denaturant. One of the striking features of monomeric amyloidogenic disordered polypeptides is that they adopt an ensemble of collapsed states under the condition that favors amyloid association. A number of recent studies have revealed that the ensemble of collapsed polypeptide chains assemble to form obligatory oligomeric intermediates on the pathway to the formation of amyloid fibrils (8, 13-15).

In this work, we have characterized the structural and dynamical properties of the monomeric-form of human β_2-microglobulin (β_2m) under the amyloid-forming condition. β_2m is a light chain of class I major histocompatibility complex (MHC), which is non-covalently attached to the α chain of MHC I molecule. Amyloid fibril formation of β_2m is implicated in dialysis related amyloidosis, a disease reported among those patients who receive prolonged haemodialysis (16). It is a 99 amino acid residue protein, comprises seven β strands, a disulfide bond between Cys 25 and Cys 80 and contains two tryptophan residues at 60 and 95 positions of the polypeptide chain (17, 18) (Fig. 2.1). The tryptophan residue at 60 is largely exposed whereas that at 95 is partially buried (18). Previous studies have shown that the transition of β_2m from soluble state to insoluble aggregates can be triggered at low pH (pH < 5) with the accumulation of distinct intermediate states (19-25). A population of a partially unfolded intermediate, possessing the characteristics of molten-globule like state, builds up at pH 3.6 that has also been supported by nuclear magnetic resonance studies (24). This intermediate state is known to form short, highly curved fibrils (21, 25) that are morphologically distinct from those identified in *ex vivo* amyloid deposits (19, 22). On the contrary, at pH 2.5, β_2m attains an ensemble of highly disordered, yet compact, conformer which was extensively characterized using NMR techniques (23, 24). Acid induced

intermediate state of β_2m undergo a nucleation-dependent polymerization leading to the formation of long and straight amyloid fibrils as observed in *ex vivo* amyloid deposits (19, 21, 22). In the present investigation, we directed our efforts to characterize the amyloidogenic intermediate state of β_2m at pH 2.5 using a diverse array of fluorescence spectroscopic tools that allows us to monitor conformational dynamics and chain dimension at the low micromolar protein concentration regime. Our time-resolved fluorescence studies provide important dynamic signature of a compact disordered state of β_2m that is markedly different from that of the canonical unfolded states of proteins. Our various studies are able to distinguish various amyloidogenic states of β_2m proteins and provide excellent corroboration of results with that of NMR studies (23).

2.2 Experimental section

2.2.1 Materials

Glycine, citric acid, potassium chloride, Tris, sodium phosphate monobasic dihydrate, sodium phosphate dibasic dihydrate, EDTA (ethylene diamine tetraacetic acid), SDS (sodium dodecyl sulfate) and ANS (8-anilinonaphthalene, 1-sulfonic acid ammonium salt) were purchased from Sigma (St. Louis, MO) and used without any further purification. All buffers with different pH, i.e. KCl-HCl (pH 1.6-2.0), Glycine-HCl (pH 2.5), Citrate buffer (pH 3.0-6.0) Sodium phosphate buffer (pH 6.5-8.0), Tris. HCl (pH 8.5), were prepared in Milli-Q water as 0.5 M stock and the pH of buffers was adjusted using Metrohm (Herisau, Switzerland) 827 pH meter at 24±1 ºC, and diluted appropriately as per requirement. IPTG (Isopropyl-beta-thio-galactopyranoside) and antibiotics (Ampicillin and Chloramphenicol) were procured from Gold Biocom (USA).

2.2.2 Protein expression, purification and characterization

The pET-23a plasmid harboring human β_2m gene with a histidine tag (26) was sub-cloned to remove the tag and was then expressed in *E. coli* BL21 DE3-lysogen cells. A single colony harboring recombinant plasmid was inoculated primarily into 10 mL LB medium containing 100 µg/mL ampicillin and 35 µg/mL chloramphenicol, culture was grown overnight at 37 ºC. Next day, 10 mL of overnight grown culture was inoculated further into 1 L fresh LB medium containing appropriate concentration of antibiotics as mentioned above. Culture was induced in the log phase using 1 mM IPTG, and the over-expressed recombinant protein was purified from the inclusion bodies, as reported previously (21). Recombinant protein was purified on anion exchanger (Q-sepharose from GE) column, by performing fast flow protein liquid chromatography. Fractions showing single peak were separately pooled and further purified using Superdex 75 column (GE). The stock solution of purified recombinant protein was stored at 4 ºC.

2.2.3 Steady-state fluorescence measurements

Steady-state fluorescence measurements were carried out on a HORIBA Scientific FluoroMax 4 spectrofluorimeter. All measurements were carried out at room temperature (24±1 ºC). Protein samples (10 µM) mixed with buffer solutions of different pH (1.6-7.0, 20 mM each) were equilibrated for 1 h at room temperature. For constant wavelength tryptophan fluorescence intensity measurements, λ_{ex} and λ_{em} were set to 295 nm (bandpass 0.8 nm) and

345 nm (bandpass 4.0 nm), respectively. The path length of the cuvette was 4 mm. The fluorescence intensities were recorded with an integration time of 1 sec. Tryptophan fluorescence anisotropy was measured by setting λ_{ex} and λ_{em} to 295 nm (bandpass 1.5 nm) and 345 nm (bandpass 12 nm), respectively. An integration time of 1 sec was used to obtain a satisfactory signal-to-noise ratio. Perpendicular components were always corrected using a G-factor that was independently recorded. The steady-state fluorescence anisotropy was collected using the following relationship.

$$r = (I_{\parallel} - I_{\perp}G) / (I_{\parallel} + 2I_{\perp}G) \quad (2.1)$$

For ANS-binding experiments, the samples were excited at 350 nm (bandpass 0.8 nm) and the spectra were collected with a scan speed of 60 nm/ min (bandpass 6.0 nm) over the range of 400-550 nm. The spectra obtained were averaged over five scans. The final concentration of ANS was 10 μM for all the experiments.

2.2.4 Circular dichroism (CD) measurements

All CD measurements were performed using a Chirascan CD spectrometer (Applied Photophysics, UK). Far UV-CD spectra were collected in the wavelength range of 195-260 nm, by pre-incubating 20 μM protein in 10 mM buffer of pH 1.6-7.0 for 1 h at room temperature. All the CD spectra were corrected using buffer baseline for every pH and smoothed using Pro-Data software available with the Chirascan CD spectrometer. The path length of the cuvette used was 1 mm. All the studies were carried out at 24±1 ºC unless otherwise stated. For the variable temperature CD experiments, the temperature of the protein sample was varied from 25-90 ºC using a Peltier temperature controller (Temperature Control TC125, Quantum Northwest) with a 5 min equilibration time at each temperature. The plots were generated using Origin Pro 8 software.

2.2.5 Time-resolved fluorescence measurements

Time-resolved fluorescence decay measurements of the samples were performed using a time-correlated single photon counting (TCSPC) setup, Fluorocube from Horiba Jobin Yvon, NJ. The samples were excited using 295 nm nano LED (for Trp) and 375 nm nano LD (for ANS). The instrument response function was ~ 1 ns for 295 nm LED and ~ 200 ps for 375 nm laser diode. The fluorescence was detected at 345 nm with a band pass of 16 nm (for Trp) and 480 nm (for ANS). The time-resolved decay of fluorescence intensity was collected at the magic angle with respect to the polarization of incident light and amplitude-weighted lifetimes were obtained. For fluorescence anisotropy decay measurements, the time-

dependent decay of fluorescence were collected at 0° [$I_{\parallel}(t)$] and 90° [$I_{\perp}(t)$] with respect to the excitation polarization and the anisotropy decays were analyzed by globally fitting $I_{\parallel}(t)$ and $I_{\perp}(t)$ as described in our previous reports (8, 27). $I_{\perp}(t)$ was always corrected with the *G*-factor that was estimated independently using free dye in isotropic solution such as NATA in water and ANS in ethanol. The anisotropy decays were analyzed using a bi-exponential decay model that takes both fast and slow rotational correlation times into account.

$$r(t) = r_0 [\beta_{fast} \exp(-t/\phi_{fast}) + \beta_{slow} \exp(-t/\phi_{slow})] \quad (2.2)$$

where r_0: intrinsic fluorescence anisotropy; ϕ_{fast} & ϕ_{slow}: fast and slow rotational correlation times; β_{fast} & β_{slow}: amplitudes associated with fast and slow rotational time.

The global (slow) rotational correlation time (ϕ_{slow}) is related to molecular volume (V) and viscosity (η) as follows:

$$\phi_{Slow} = \eta V/kT \quad (2.3)$$

$$V = {}^{4}/_{3}\, \pi R_h^{3} \quad (2.4)$$

Where R_h is the hydrodynamic radius of the molecule.

2.2.6 Stopped-flow fluorescence measurements

Stopped-flow mixing experiments were carried out on a spectrometer (Chirascan, Applied Photophysics) connected to a stopped-flow apparatus (SF. 3, Applied Photophysics) as reported in our previous study (27). A pH jump from pH 7 $\rightarrow$ 2.5 was achieved by rapidly mixing a β_2m stock in pH 7.0 (10 mM phosphate buffer) with pH 2.5 (50 mM of Glycine-HCl buffer) in 1:10 ratio, with a final protein concentration of 5 μM. The dead time of mixing was ~ 3 ms. For tryptophan fluorescence kinetics, samples were excited at 295 nm and fluorescence was collected using a 320 nm long pass filter, whereas, for ANS fluorescence kinetics, samples were excited at 350 nm and fluorescence was collected using 455 nm long pass filter. The final ANS concentration used in the experiment was 10 μM. The kinetic traces were acquired for 5 sec with 10000 time points and were averaged over 10 data sets to get a satisfactory signal-to-noise ratio. Native baselines were collected by mixing the protein stock with pH 7 buffer without a pH jump and were used for determining the amplitude of burst-phase. The multiple data sets were averaged and the data up to 5 sec were fitted mono-exponentially in Origin or ProData software to obtain the observed rate.

2.3 Results and discussion

2.3.1 Expression and purification of human β_2m

After purification of β_2m, protein was run on the SDS-PAGE to confirm the purity of the purity and size of the protein.

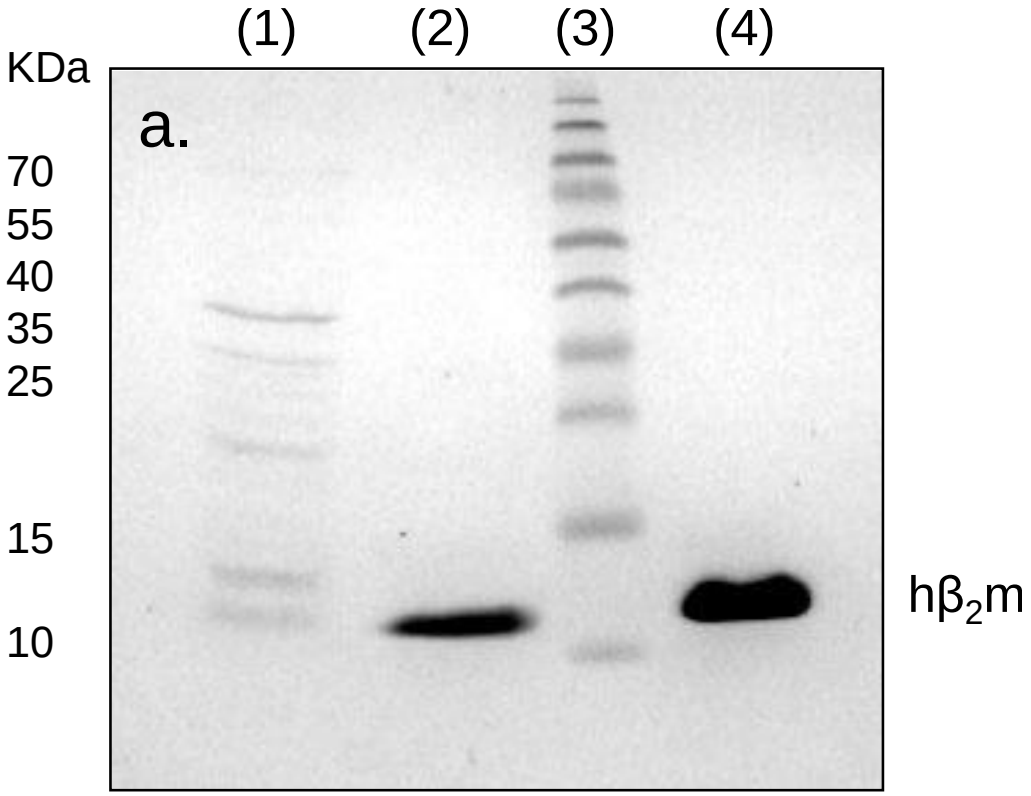

Figure 2.1 SDS-PAGE (15% Acrylamide) analysis of purified human β_2m. Lane (1) uninduced sample (2) induced sample (3) Protein ladder (4) purified protein.

2.3.2 pH-induced conformational transitions investigated using steady-state fluorescence

Human β_2m contains two tryptophan residues at 60 (exposed) and 95 (partially buried) residue positions (Fig. 2.2). We first investigated the changes in intrinsic tryptophan fluorescence of β_2m from the native to an acid unfolded state as a function of pH (28). Under native condition, tryptophan fluorescence showed a peak at ~ 337 nm that corresponds to partially exposed tryptophans. At low pH down to pH 1.6, the emission maximum demonstrated a red shift of ~8 nm (Fig. 2.3 *a*). These data revealed that the average level of exposure of the tryptophans increases upon acid-induced structural transition. Additionally, the change in tryptophan fluorescence intensity monitored at 337 nm, suggested a cooperative structural transition of β_2m as a function of pH (Fig. 2.3 *b*). In order to probe the overall changes in the dimension of β_2m, we measured the steady-state fluorescence anisotropy of tryptophan that showed a substantial decrease at low pH compared to that at neutral pH (Fig. 2.3 *c*). Together, these results indicated a cooperative structural loss of β_2m at low pH.

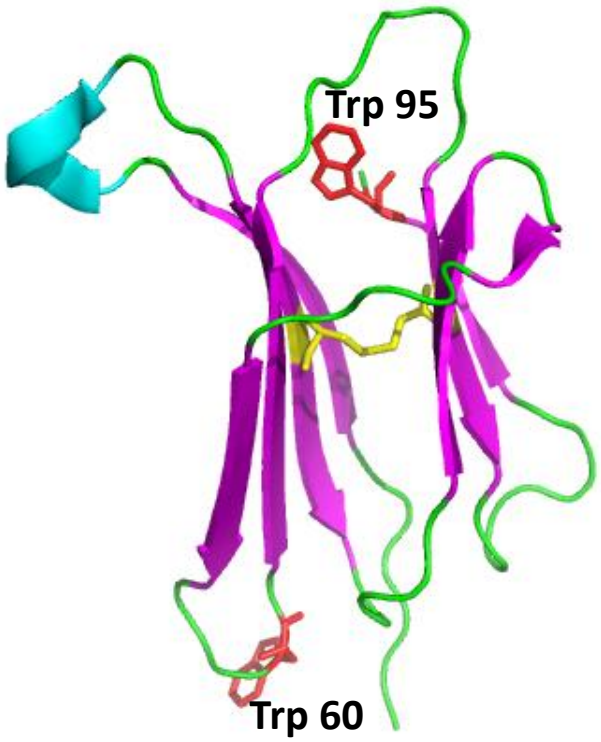

Figure 2.2 Ribbon diagram of human β_2-microglobulin generated using PyMol (Delano Scientific LLC, CA) from the Protein Data Bank (PDB ID: 1LDS). The tryptophans (Trp 60 and Trp 95) and the single disulfide bond (Cys 25-Cys 80) are shown as red and yellow sticks, respectively.

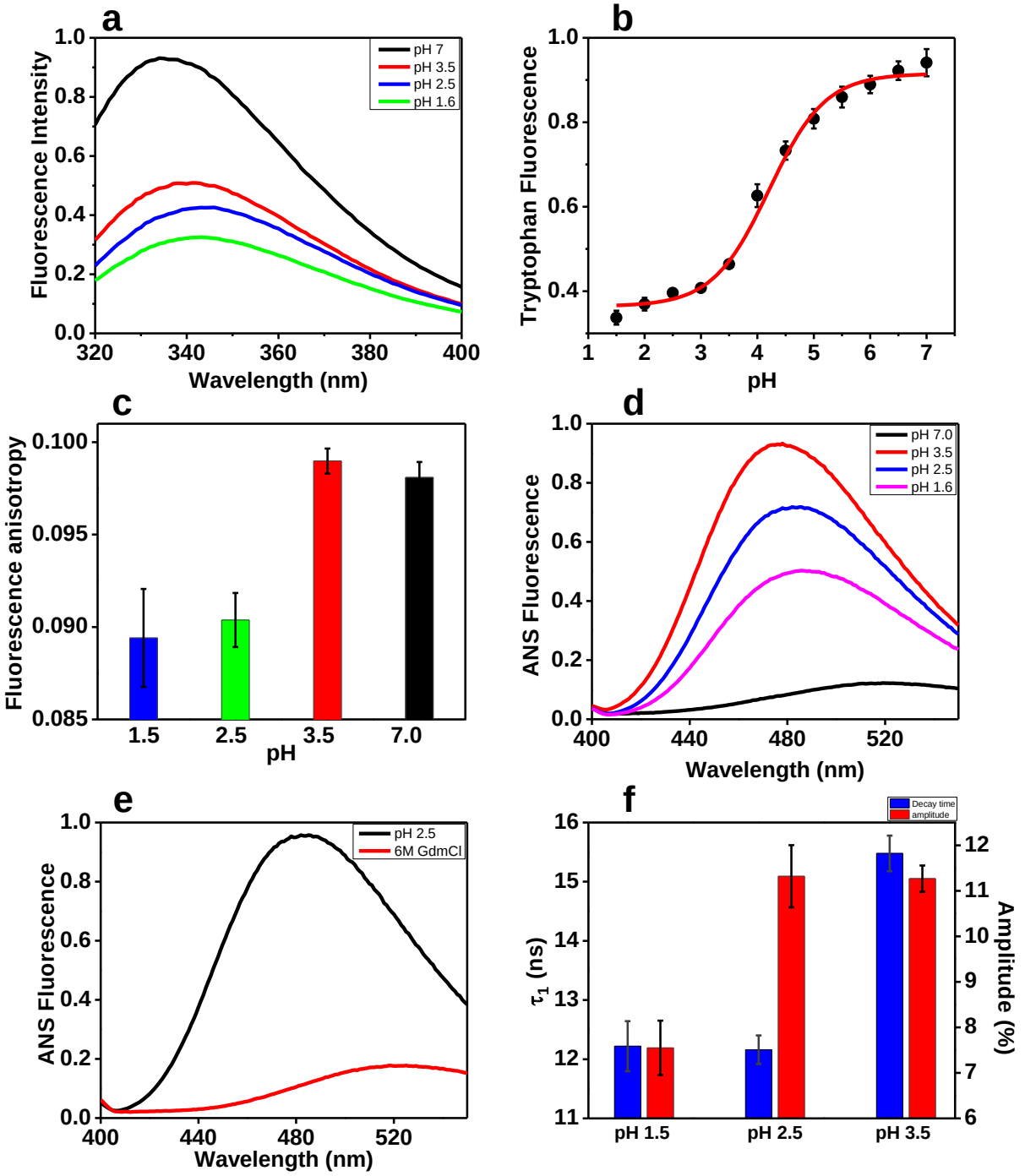

Figure 2.3 (a) Tryptophan fluorescence spectra of β_2m (10 µM) at different pH. (b) Changes in the tryptophan fluorescence intensity at 337 nm (filled circle) and the red solid line represents the sigmoidal fit. (c) Tryptophan anisotropy monitored at 345 nm as a function of pH. (d) ANS emission spectra in the presence of β_2m at different pH. (e) Comparison of ANS fluorescence spectra bound to 6 M GdmCl (red line) induced unfolded state of β_2m with that of pH 2.5 form (5 µM; black line). (f) change in the long lifetime component of ANS (blue) and its amplitude (red) bound to different states of β_2m.

Next, we investigated the protein conformational changes by ANS, which fluoresces strongly when bound to hydrophobic environment (29). At neutral pH, ANS does not show any binding to the native β_2m. Upon lowering the pH, the ANS fluorescence increases and peaks at pH 3.5 indicating the presence of a molten-globule like intermediate of β_2m with highest number of accessible hydrophobic sites (Fig. 2.3 *d*). This observation is in accordance with previous results (21). The ANS fluorescence drops from pH 3.5 to 2.5 that further decreases from pH 2.5 to 1.6 indicating a partial disruption of hydrophobic patches at much lower pH possibly due to further unfolding of the molten-globule state. However, the low pH form is ANS active unlike the denatured state of the protein (Fig. 2.3 *e*). The measurement of ANS fluorescence lifetime revealed that the long lifetime component was shorter in case of the pH 2.5 form when compared with the molten-globule form at pH 3.5. Upon transition from pH 2.5 to 1.6, the protein underwent further denaturation that diminished the contribution of the long lifetime component. This intermediate state of β_2m at pH 2.5 consists of lower degree of structure while having high binding affinity towards ANS and is different from either the molten-globule like intermediate populated at ~ pH 3.5 or the GdmCl induced unfolded state (Fig 2.3 *f*). We also compared ANS fluorescence observed for the intermediate of β_2m at pH 2.5 with a model molten-globule state of α-lactalbumin (30) which revealed that the former showed significantly lower ANS fluorescence (Fig. 2.4). These results provide support to the conjecture that β_2m adopts a disordered, yet compact ANS active state at pH 2.5.

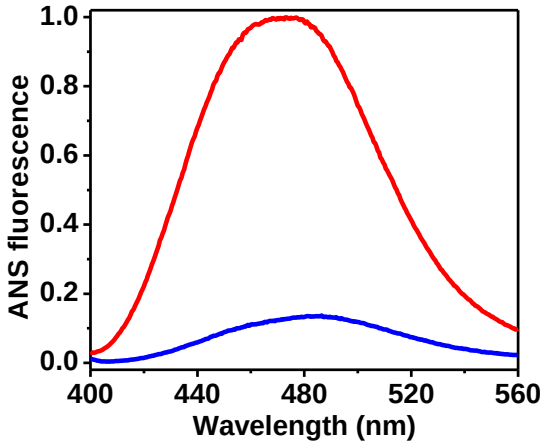

Figure 2.4 Comparison of ANS fluorescence spectra bound to an archetypal molten-globule state of α-lactalbumin (5 μM; red solid line) with that of pH 2.5 form of β_2m (5 μM; blue solid line).

2.3.3 Structural transition investigated using circular dichroism

In order to obtain insights into the changes in the secondary structural contents during pH-induced structural transition, we performed far-UV circular dichroism measurements (Fig. 2.5). Native β_2m displayed strong negative ellipticity band at ~ 218 nm and a positive band at ~ 200 nm indicating a characteristic feature of β-sheet proteins (21). Upon lowering the pH, the negative ellipticity signal became more pronounced than that of the native protein (Fig. 2.5 *a*). The ellipticity at 200 nm as a function of pH titration depicts the loss of structure in a cooperative fashion (Fig. 2.5 *b*). The ratiometric CD plot ($\theta_{200}/\theta_{218}$) indicated an increase in the disorderedness at the expense of the loss in β-sheet structure (Fig. 2.5 *c*). Thermal unfolding of β_2m, monitored over a range of temperature (20-90 ºC) at neutral pH illustrated a cooperative thermal unfolding (Fig. 2.5 *d,f*). The thermal unfolding of the molten-globule form of β_2m at pH 3.5 showed a non-cooperative transition as a function of temperature (Fig. 2.6). In a sharp contrast to this, thermal denaturation of the intermediate at pH 2.5 does not show significant changes in the CD spectra as a function of temperature (Fig. 2.5 *e,f*).

A closer look at the CD data allowed us to gain more structural insights into the disordered state. Previously, a CD double-wavelength plot of the mean residue molar ellipticity (θ in deg.cm^2.dmol^{-1}) at two wavelengths ($\theta_{200\ nm}$ *vs.* $\theta_{222\ nm}$) has been used to empirically assess and distinguish among highly denatured, collapsed pre-molten globule and molten globule state of disordered proteins (31). Our CD double-wavelength analysis revealed that at the pH 3.5 form represents a molten-globule like form ($\theta_{200\ nm}$ ~ -4663 and $\theta_{222\ nm}$ ~ -3570), whereas, the pH 2.5 form resembles a pre-molten-globule like ($\theta_{200\ nm}$ ~ -7442 and $\theta_{222\ nm}$ ~ -3741). These results indicate that β_2m attains a disordered state at pH 2.5 with an element of residual structure that lies between partially structured molten-globule like and unfolded state and are consistent with recent reports (32, 33). Therefore, the CD data in combination with fluorescence data indicate that at pH 2.5, β_2m adopts a collapsed, pre-molten globule like non-canonical denatured state. In order to gain dynamic insights into this state, we further performed time-resolved fluorescence experiments.

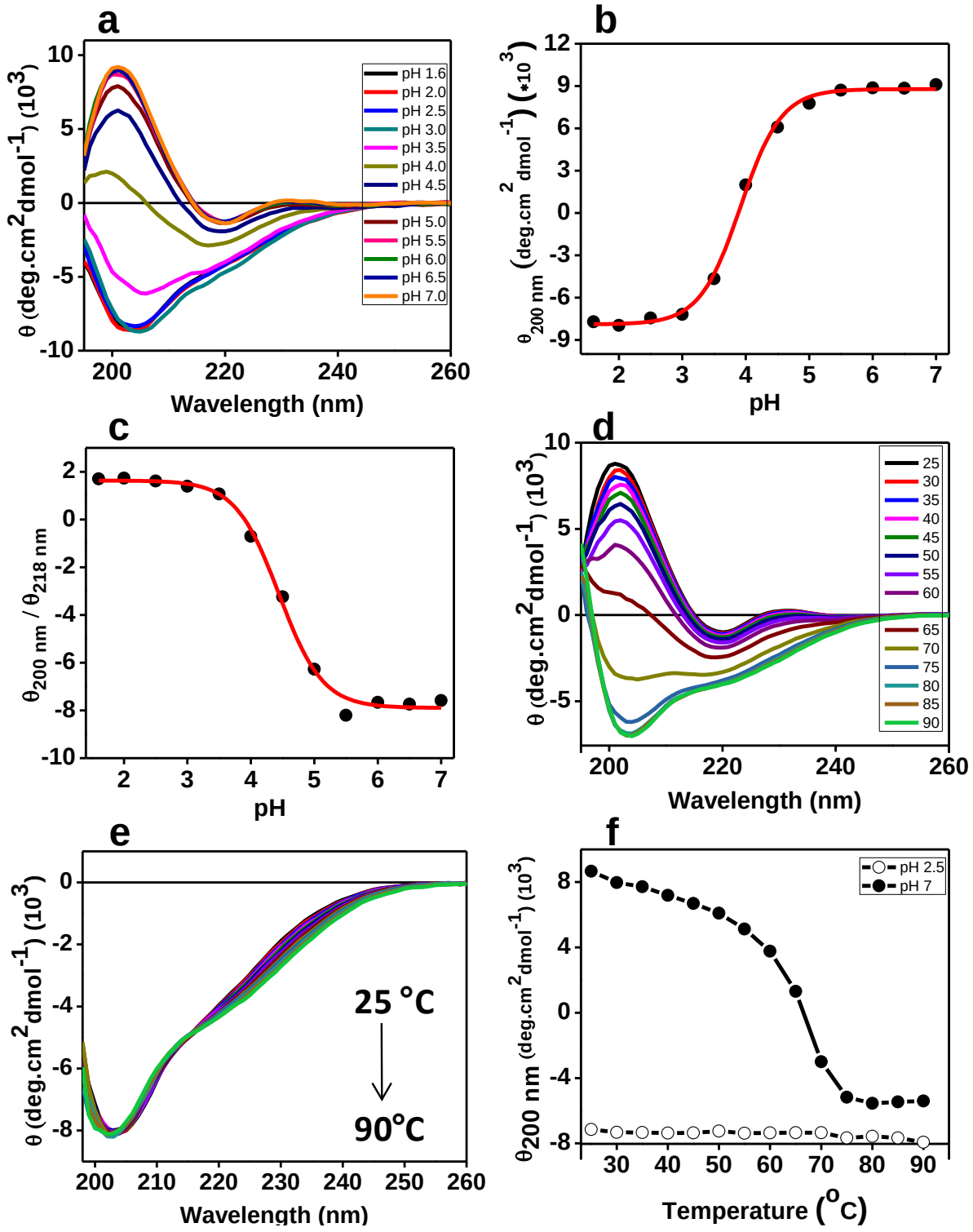

Figure 2.5 (a) Far-UV CD spectra of β_2m (20 μM) at different pH. (b) Changes in the mean residue molar ellipticity at 200 nm as a function of pH. (c) A ratiometric ellipticity plot at 200 nm (random coil) to 218 nm (β-sheet) as a function of pH. The red solid lines in (b) and (c) represent the sigmoidal fit. Thermal unfolding of β_2m (from 25-90 °C) in the native (pH 7) (d), and intermediate state (pH 2.5) (e). (f) Variation in the mean residue molar ellipticity at 200 nm for native (pH 7; filled circle) and the intermediate forms (pH 2.5; open circle) as a function of temperature. The solid line serves as an eye-guide.

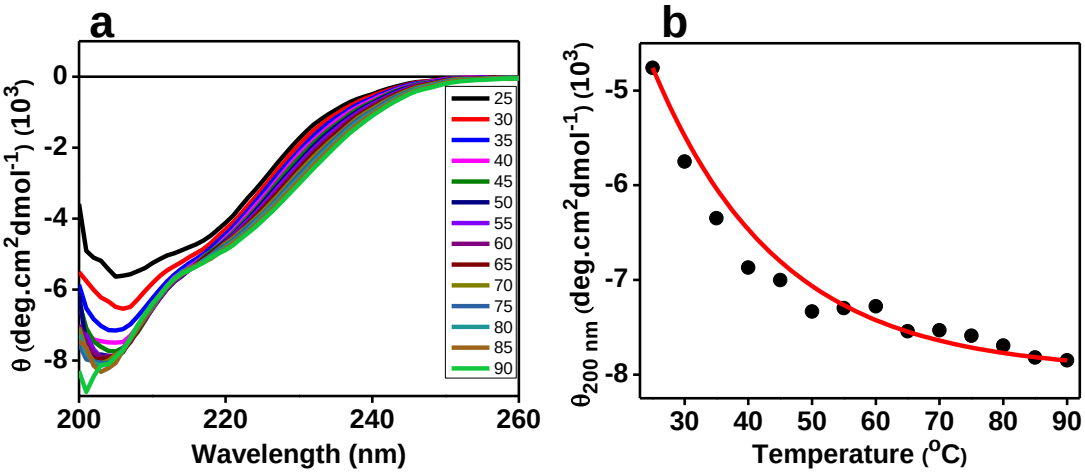

Figure 2.6 (a) Far UV-CD spectra of thermal unfolding of β_2m (from 25-90 °C) in the molten-globule like intermediate state (pH 3.5) collected in the wavelength range of 200-260 nm. (b) Variation in the mean residue molar ellipticity at 200 nm for intermediate form (pH 3.5) as a function of temperature. The red solid line is merely a guiding line for viewing.

2.3.4 Monitoring structural changes by fluorescence lifetime measurements

Time-resolved fluorescence measurements allowed us to determine the fluorescence lifetime of tryptophan that is very sensitive to protein structural changes (28). The tryptophan residues in β_2m displayed two and three lifetime components under native and at pH 2.5, respectively. The mean fluorescence lifetime (τ_m) of tryptophan decreased from ~ 2.5 ns (native) to ~ 2.1 ns (pH 2.5) and the fast sub-nanosecond decay component was seen at pH 2.5 indicating that the tryptophans become more exposed to aqueous environment (Fig. 2.7 *a,b* & Table 2.2). These results are consistent with the evidences that β_2m adopts a more disordered state at pH 2.5 in which tryptophans are more exposed to bulk water.

Next, we determined the lifetime of ANS bound to the acid unfolded intermediate and compared with other pH conformational states. The ANS-protein complex at pH 2.5 showed high fluorescence intensity (Fig 2.7 *d*). ANS is practically non-fluorescent in water and shows mono-exponential decay in aqueous solution with a typical fluorescence lifetime of 0.25 ns (34). ANS bound to the pH 2.5 form of β_2m yielded three lifetime components with a mean lifetime of ~ 2.3 ns. The longer lifetime components of ANS (12 ns and 3.4 ns) can be correlated with two different complexes having different solvent accessibility. The longer lifetime component (τ > 10 ns) of ANS fluorescence decay reflects a complex in which ANS molecules appear to be well protected from the water molecules, hence indicating the presence of hydrophobic core patches.

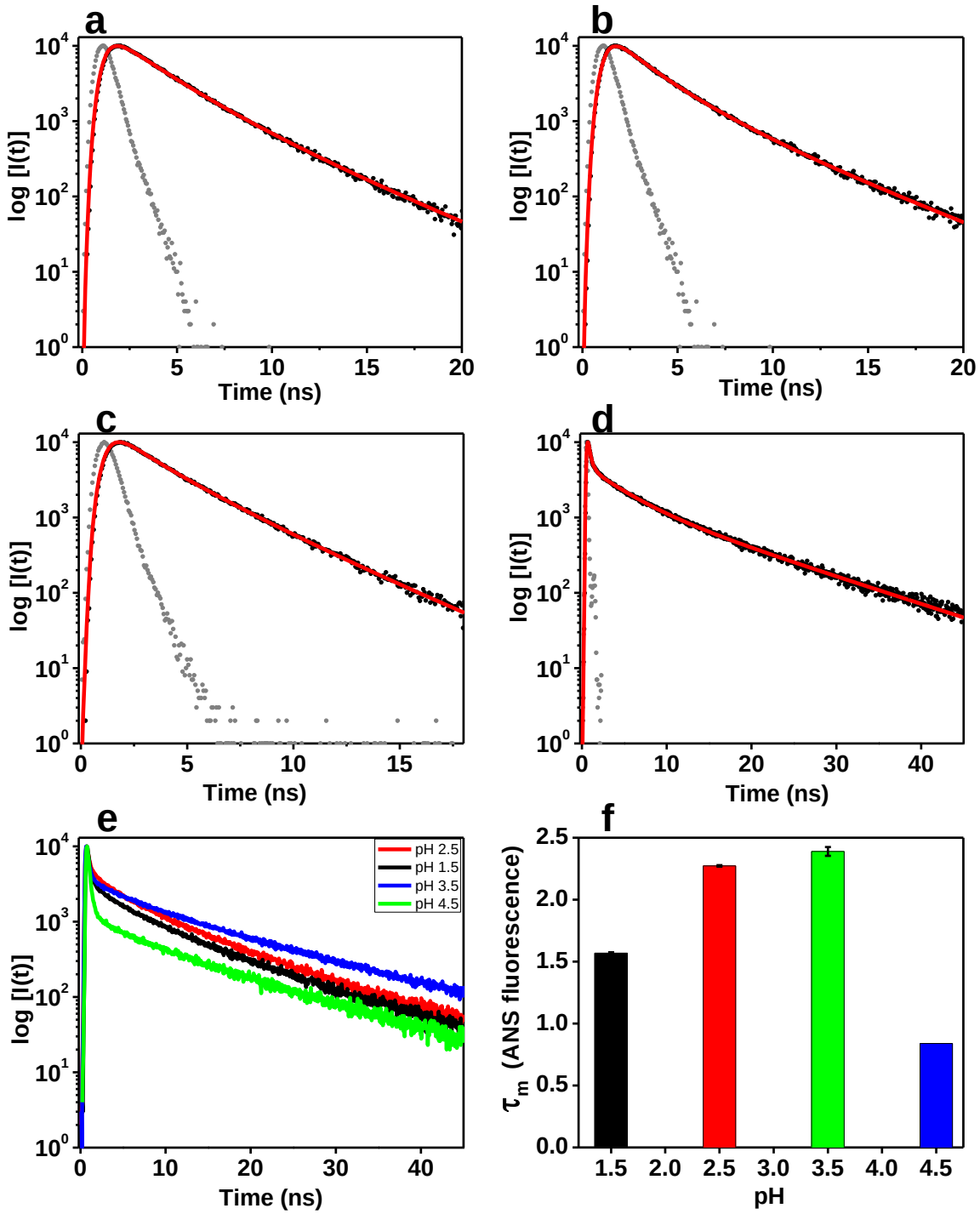

Figure 2.7 Time-resolved fluorescence intensity decay profiles of β_2m (20 μM) under different denaturing conditions. Tryptophan fluorescence intensity decays of β_2m at native (pH 7) (a), intermediate (pH 2.5) (b), and 3M GdmCl (c), states, respectively. ANS fluorescence intensity decay bound to intermediate state of β_2m at pH 2.5 (d) and to intermediate states at different pH values (1.5, 2.5, 3.5, and 4.5) (e). (f) Mean fluorescence lifetime of ANS bound to different intermediates of β_2m. For recovered parameters, see Table 2.1 and 2.2. In all the fluorescence intensity decay profiles, the scatter line represents the instrument response function and the observed decay and the red solid line represents the fitted data.

However, the shorter lifetime component ($\tau < 6$ ns) is characteristic of the dye molecules that interact with the superficial hydrophobic patches which can be accessible to solvent molecules (34) (Fig. 2.7 *d* & Table 2.1). These results indicate that at pH 2.5, β_2m adopts a disordered, yet compact state that is capable of binding to hydrophobic fluorescent dye such as ANS. This state, albeit ANS active, has much lower binding affinity compared to an archetypal molten-globule state such as the low pH form of bovine α-lactalbumin that confers much longer (> 10 ns) mean fluorescence lifetime of ANS (34). The mean fluorescence lifetime of ANS bound to β_2m showed an increase from pH 4.5 to pH 3.5 and decreased with further decrease in the pH (Fig. 2.7 *e,f* & Table 2.1). This indicates the presence of two structural transitions involving from native-like structure to molten- globule and from molten-globule to pre-molten globule like compact disordered structure, which undergoes continuous expansion upon acidification.

Table 2.1: Time-resolved fluorescence lifetimes of ANS in intermediate conformations of β_2m.

Conditions (Probes)	Fluorescence lifetime in ns (amplitude)			τ_m	χ^2
	τ_1 (α_1)	τ_2 (α_2)	τ_3(α_3)		
pH 4.5 (ANS)	13.7 (0.03)	4.6 (0.03)	0.25 (0.94)	0.84	1.07
pH 3.5 (ANS)	15.6 (0.1)	5 (0.1)	0.27 (0.8)	2.43	0.99
pH 2.5 (ANS)	12 (0.12)	3.4 (0.17)	0.29 (0.71)	2.27	1.19
pH 1.5 (ANS)	12.25 (0.07)	4.23 (0.1)	0.27 (0.83)	1.56	1.03

2.3.5 Insights into polypeptide chain dynamics and dimension using fluorescence anisotropy decay measurements

Time-resolved fluorescence anisotropy provides important information about the dynamics and dimension of the polypeptide chain (28, 35-37). The time-resolved decay of fluorescence anisotropy often yields two rotational correlation times that allows one to distinguish the dynamics at different timescales. The fast (ϕ_{fast}) and the slow (ϕ_{slow}) rotational correlation times represent the local probe dynamics and the global macromolecular dynamics, respectively. The slower (global) correlation time (ϕ_{slow}) can be used to estimate the hydrodynamic size of the protein (Eq. 2.2-2.4 in section 4.5). Our time-resolved anisotropy data of tryptophan showed that the amplitude of the fast correlation time (β_{fast}) increased from ~ 37% to ~ 61% depicting an increased conformational flexibility of the tryptophans in the low pH form of β_2m. The slow rotational correlation time (ϕ_{slow}) that corresponds to global rotational motion of the protein increased from ~ 5.9 ns to ~ 8.8 ns upon changing the pH from 7 to 2.5 indicating an increase in the mean hydrodynamic volume of the protein (Fig. 2.8 *a,b* & Table 2.2). The increase in ϕ_{slow} upon structural loss is in sharp contrast to archetypal unfolded (denatured) states of a protein that demonstrates a decrease in slow rotational correlation time. Our time-resolved fluorescence anisotropy measurements on guanidinium chloride denatured β_2m showed a much shorter ϕ_{slow} (~ 3.6 ns; Fig. 2.8 *c*). This ϕ_{slow} cannot account for the global rotational motion of the denatured protein since the mean hydrodynamic volume of a denatured protein is expected to be much larger. Therefore, ϕ_{slow} in the denatured state represents the segmental chain mobility arising out of enhanced conformational flexibility of the polypeptide chain. On the contrary, at pH 2.5, albeit the loss in the secondary and tertiary structures, the polypeptide chain adopts a collapsed conformation that does not allow the chain to undergo any detectable segmental motion and therefore, the tryptophan dynamics demonstrates only two well separated components representing the local and global rotational motion. We would like to point out that the absence or presence of the segmental mobility might be useful to distinguish between collapsed disordered and archetypal denatured states of proteins. Therefore, collapsed disordered chains are expected to display longer rotational correlation times that correspond to their average volume of the collapsed globule as observed earlier by us for an amyloidogenic intrinsically disordered protein (8).

The hydrodynamic radii (R_h) calculated from the respective slow rotational correlation times showed an increase from ~ 1.9 nm (native) to ~ 2.1 nm (pH 2.5

intermediate). Since the mean fluorescence lifetime of tryptophan (~ 2.1 ns) is shorter compared to the longer rotational correlation time of the protein (ϕ_{slow}), we also measured ANS fluorescence anisotropy decay to estimate the longer rotational correlation time with a better precision (Fig. 2.8 *d*). The slow rotational correlation time measured from ANS fluorescence having longer fluorescence lifetime is ~ 9.9 ns and the corresponding R_h was estimated to be ~ 2.2 nm that corroborates with the previously reported R_h (36). The respective hydrodynamic volume of the protein increases from ~ 27 nm^3 (native) to ~ 46 nm^3 (pH 2.5). This volume expansion (~ 70%) in the low pH form compared to that of the native form is higher than it is generally observed for transition from native- to molten-globule state of proteins (35-60%) (27, 38). All of the above results indicated an increased conformational flexibility and swelling of protein structure at pH 2.5 leading to a collapsed form of β_2m and corroborated the results obtained in the previous investigation (23). Our results demonstrated that time-resolved fluorescence can be a powerful tool to directly monitor the local, segmental and global protein dynamics and obtain both the dynamic signature and the size information of amyloidogenic proteins under monomeric condition at considerably low micromolar protein concentrations.

Table 2.2: Typical parameters associated with the time-resolved fluorescence intensity and anisotropy decays of tryptophan and ANS[a]

Conditions (probes)	Fluorescence lifetime in ns (amplitude)			τ_m	χ^2	Rotational correlation times in ns (amplitude)		r_o	χ^2
	τ_1 (α_1)	τ_2 (α_2)	τ_3(α_3)			ϕ_{fast} (β_{fast})	ϕ_{slow} (β_{slow})		
pH 7 (Tryptophan)	4.10 (0.24)	2.01 (0.76)	-	2.54	1.01	0.37 (0.37)	5.93 (0.63)	0.193	1.15
pH 2.5 (Tryptophan)	4.45 (0.17)	2.24 (0.45)	0.97 (0.38)	2.10	1.01	0.35 (0.61)	8.84 (0.39)	0.193	1.25
3M GdmCl (Tryptophan)	3.95 (0.44)	1.80 (0.56)	-	2.75	1.05	0.31 (0.62)	3.6 (0.38)	0.196	1.19
pH 2.5 (ANS)	12 (0.12)	3.4 (0.17)	0.29 (0.71)	2.27	1.19	0.10 (0.3)	9.97 (0.7)	0.359	1.60

[a]Typical errors in the analyses of time-resolved fluorescence intensity and anisotropy decays are as follows: $\tau_m \leq 0.05$ ns; $\varphi_{fast} \leq 0.1$ ns; $\varphi_{slow} \leq 0.5$ ns; $\beta_{fast} \leq 0.05$; $\beta_{slow} \leq 0.05$.

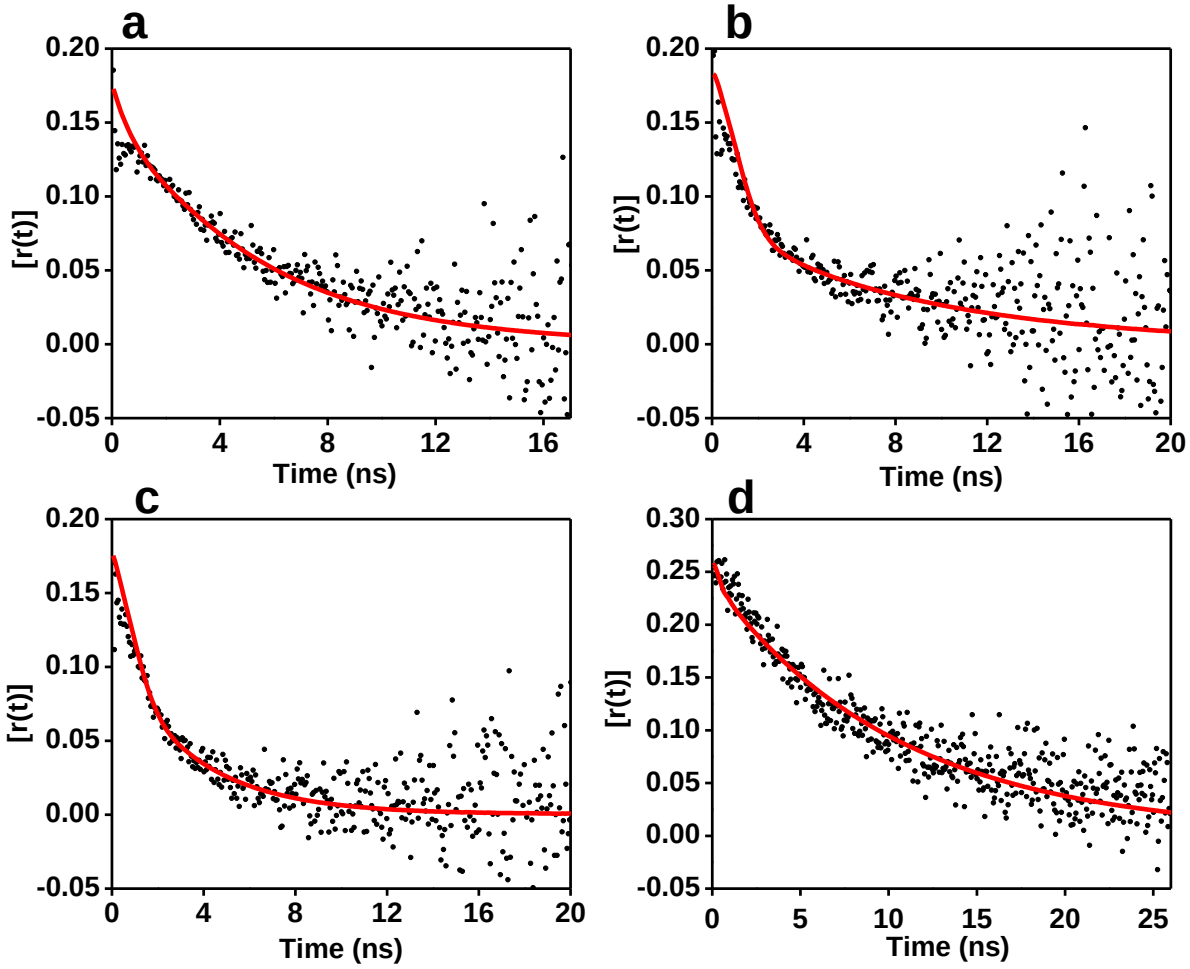

Figure 2.8 Time-resolved fluorescence anisotropy decays of Trp of β_2m at pH 7 (a), pH 2.5 (b), and 3M GdmCl (c), respectively. (d) Time-resolved fluorescence anisotropy decay of ANS bound to pH 2.5 intermediate. In all the fluorescence anisotropy decay profiles, the scatter line represents the instrument response function and the observed decay and the red solid line represents the fitted data.

2.3.6 Kinetics of conformational change using stopped-flow fluorescence

All the equilibrium studies established that the intermediate state of β_2m formed at pH 2.5 adopts a compact disordered state and represents a non-canonical unfolded state. Additionally, from the CD double-wavelength plot analysis, we believe that this pH 2.5 state shares the conformational characteristics of an empirically described pre-molten globule-like state (31). Next, we investigated the kinetics of conformational transition from the natively folded β_2m to the disordered pre-molten globule like state by performing a pH jump from pH 7 $\rightarrow$ 2.5. Upon rapid mixing, the tryptophan fluorescence demonstrated burst phase (~ 78%) in which a sharp drop in the total fluorescence intensity was observed within the dead-time of mixing (~ 3 ms). The resolved phase could satisfactorily be described by a mono-exponential kinetics with a rate constant $\approx$ 1.5 s^{-1} (Fig. 2.9 *a* & Table 2.3). The kinetics of tryptophan

fluorescence depicting the protein structural changes reveal that the formation of pH 2.5 state of β_2m proceeds via multiple steps involving a very fast unresolved sub-millisecond phase followed by a slow phase leading to polypeptide chain expansion that causes the decrease in the tryptophan fluorescence. Next we asked the question as to how the kinetics of protein structural changes is related to the time evolution of ANS fluorescence, which reports the genesis of the accessible hydrophobic patches upon the loss in structure. When we jumped the pH of a mixture containing ANS and β_2m from pH 7 $\rightarrow$ 2.5, the time-evolution of ANS fluorescence demonstrated a burst phase (~ 30%) that is smaller compared with the burst phase (~ 78%) obtained from the kinetics of tryptophan fluorescence (Fig. 2.9 *b*). Therefore, within the dead time of mixing, the extent of structure loss probed tryptophan fluorescence by is much larger than that of the formation of accessible hydrophobic patches probed by ANS fluorescence. The resolved phase of ANS fluorescence kinetics can be satisfactorily described by a mono-exponential kinetics with a rate constant $\approx$ 2.1 s^{-1} (Table 2.3). Taken together, these results provide insights into the kinetics of acid-induced unfolding of β_2m leading to a compact disordered state that share some characteristics with a pre-molten globule state of intrinsically disordered proteins.

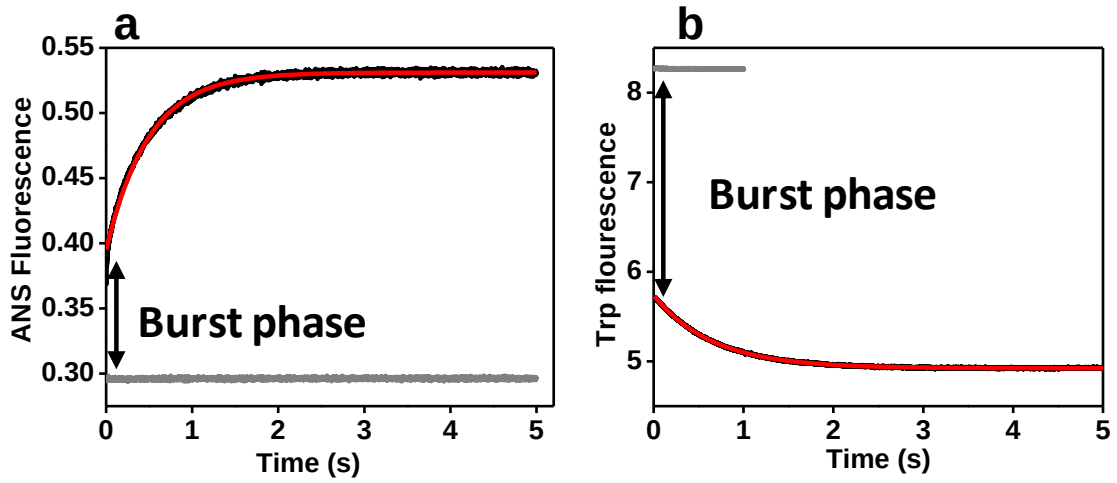

Figure 2.9: Stopped-flow fluorescence kinetics of β_2m monitored by a time-dependent change in the total fluorescence intensities of tryptophan (a), and ANS (b) as a function of pH jump from pH 7 to pH 2.5. The baseline is shown in grey. The data was fitted (black solid line) mono-exponentially (Red solid line) to recover the apparent rate constants. For recovered kinetic parameters, see Table 2.3.

Table 2.3: Recovered kinetic parameters from stopped-flow fluorescence experiments

Probes	% of burst phase	Rate (s^{-1})
Trp	78 ± 5	1.5 ± 0.1
ANS	30 ± 5	2.1 ± 0.1

2.4 Conclusion

In conclusion, we have provided structural and dynamical insights into the monomeric form of β_2m that are populated at low pH. Both our equilibrium and kinetics results show a structural transition from the native-form to a disordered, yet compact, state. The compact disordered state formed at pH 2.5 serves as a precursor to long and straight amyloid fibrils resembling the *ex vivo* deposits found in amyloidosis (21, 24). We suggest that at higher protein concentration and in the presence of salt, the exposed hydrophobic patches in the collapsed disordered polypeptide chains would facilitate oligomers formation that will conformationally mature into amyloid fibrils as proposed previously for an intrinsically disordered yeast prion protein (9, 14). Recently, molecular simulations have provided the mechanistic insights into the association of disordered polypeptide chains (15). Additionally, our time-resolved fluorescence anisotropy measurements provide important insights into both chain dimension and dynamics simultaneously. We believe that a combination of fluorescence techniques described here will be extremely useful to delineate the structural and dynamical signatures of amyloidogenic proteins.

2.5 References

1. Eichner T & Radford SE (2011) A diversity of assembly mechanisms of a generic amyloid fold. *Molecular cell* 43(1):8-18.
2. Eisenberg D & Jucker M (2012) The amyloid state of proteins in human diseases. *Cell* 148(6):1188-1203.
3. Lee J, Culyba EK, Powers ET, & Kelly JW (2011) Amyloid-β forms fibrils by nucleated conformational conversion of oligomers. *Nature chemical biology* 7(9):602-609.
4. Luheshi LM, Crowther DC, & Dobson CM (2008) Protein misfolding and disease: from the test tube to the organism. *Current opinion in chemical biology* 12(1):25-31.
5. Moreno-Gonzalez I & Soto C (2011) Misfolded protein aggregates: mechanisms, structures and potential for disease transmission. *Seminars in cell & developmental biology*, (Elsevier), pp 482-487.
6. Crick SL, Jayaraman M, Frieden C, Wetzel R, & Pappu RV (2006) Fluorescence correlation spectroscopy shows that monomeric polyglutamine molecules form collapsed structures in aqueous solutions. *Proceedings of the National Academy of Sciences* 103(45):16764-16769.
7. Drescher M, Huber M, & Subramaniam V (2012) Hunting the Chameleon: Structural Conformations of the Intrinsically Disordered Protein Alpha-Synuclein. *ChemBioChem* 13(6):761-768.
8. Jain N, Bhattacharya M, & Mukhopadhyay S (2011) Chain collapse of an amyloidogenic intrinsically disordered protein. *Biophysical journal* 101(7):1720-1729.
9. Mukhopadhyay S, Krishnan R, Lemke EA, Lindquist S, & Deniz AA (2007) A natively unfolded yeast prion monomer adopts an ensemble of collapsed and rapidly fluctuating structures. *Proceedings of the National Academy of Sciences* 104(8):2649-2654.
10. Trexler AJ & Rhoades E (2010) Single molecule characterization of α-synuclein in aggregation-prone states. *Biophysical journal* 99(9):3048-3055.
11. Uversky VN (2009) Intrinsically disordered proteins and their environment: effects of strong denaturants, temperature, pH, counter ions, membranes, binding partners, osmolytes, and macromolecular crowding. *The protein journal* 28(7-8):305-325.

12. Uversky VN & Fink AL (2004) Conformational constraints for amyloid fibrillation: the importance of being unfolded. *Biochimica et Biophysica Acta (BBA)-Proteins and Proteomics* 1698(2):131-153.
13. Pappu RV, Wang X, Vitalis A, & Crick SL (2008) A polymer physics perspective on driving forces and mechanisms for protein aggregation. *Archives of biochemistry and biophysics* 469(1):132-141.
14. Serio TR, *et al.* (2000) Nucleated conformational conversion and the replication of conformational information by a prion determinant. *Science* 289(5483):1317-1321.
15. Vitalis A & Pappu RV (2011) Assessing the contribution of heterogeneous distributions of oligomers to aggregation mechanisms of polyglutamine peptides. *Biophysical chemistry* 159(1):14-23.
16. Gorevic PD, *et al.* (1986) Polymerization of intact beta 2-microglobulin in tissue causes amyloidosis in patients on chronic hemodialysis. *Proceedings of the National Academy of Sciences* 83(20):7908-7912.
17. Saper M, Bjorkman P, & Wiley D (1991) Refined structure of the human histocompatibility antigen HLA-A2 at 2.6 Å resolution. *Journal of molecular biology* 219(2):277-319.
18. Trinh CH, Smith DP, Kalverda AP, Phillips SE, & Radford SE (2002) Crystal structure of monomeric human β-2-microglobulin reveals clues to its amyloidogenic properties. *Proceedings of the National Academy of Sciences* 99(15):9771-9776.
19. Gosal WS, *et al.* (2005) Competing pathways determine fibril morphology in the self-assembly of β 2-microglobulin into amyloid. *Journal of molecular biology* 351(4):850-864.
20. Katou H, *et al.* (2002) The role of disulfide bond in the amyloidogenic state of β2-microglobulin studied by heteronuclear NMR. *Protein science* 11(9):2218-2229.
21. McParland VJ, *et al.* (2000) Partially unfolded states of β2-microglobulin and amyloid formation in vitro. *Biochemistry* 39(30):8735-8746.
22. Naiki H, *et al.* (1997) Establishment of a kinetic model of dialysis-related amyloid fibril extension in vitro. *Amyloid* 4(4):223-232.
23. Platt GW, McParland VJ, Kalverda AP, Homans SW, & Radford SE (2005) Dynamics in the unfolded state of β 2-microglobulin studied by NMR. *Journal of molecular biology* 346(1):279-294.

24. Skora L, Becker S, & Zweckstetter M (2010) Molten globule precursor states are conformationally correlated to amyloid fibrils of human β-2-microglobulin. *Journal of the American Chemical Society* 132(27):9223-9225.
25. Smith DP, Jones S, Serpell LC, Sunde M, & Radford SE (2003) A systematic investigation into the effect of protein destabilisation on beta 2-microglobulin amyloid formation. *Journal of molecular biology* 330(5):943-954.
26. Dalal V, Bhattacharya M, Narang D, Sharma PK, & Mukhopadhyay S (2012) Nanoscale fluorescence imaging of single amyloid fibrils. *The Journal of Physical Chemistry Letters* 3(13):1783-1787.
27. Bhattacharya M & Mukhopadhyay S (2011) Structural and dynamical insights into the molten-globule form of ovalbumin. *The Journal of Physical Chemistry B* 116(1):520-531.
28. Lakowicz JR (2013) *Principles of fluorescence spectroscopy* (Springer Science & Business Media).
29. Semisotnov G, *et al.* (1991) Study of the "molten globule" intermediate state in protein folding by a hydrophobic fluorescent probe. *Biopolymers* 31(1):119-128.
30. Kuwajima K (1996) The molten globule state of alpha-lactalbumin. *The FASEB journal* 10(1):102-109.
31. Uversky VN (2002) Natively unfolded proteins: a point where biology waits for physics. *Protein science* 11(4):739-756.
32. Mukaiyama A, *et al.* (2013) The Molten Globule of β 2-Microglobulin Accumulated at pH4 and Its Role in Protein Folding. *Journal of molecular biology* 425(2):273-291.
33. Yanagi K, *et al.* (2012) The monomer–seed interaction mechanism in the formation of the β2-microglobulin amyloid fibril clarified by solution NMR techniques. *Journal of molecular biology* 422(3):390-402.
34. Uversky VN, Winter S, & Löber G (1996) Use of fluorescence decay times of 8-ANS-protein complexes to study the conformational transitions in proteins which unfold through the molten globule state. *Biophysical chemistry* 60(3):79-88.
35. Krishnamoorthy G (2012) Motional dynamics in proteins and nucleic acids control their function: revelation by time-domain fluorescence. *Curr Sci* 102:266-276.
36. Millar DP (1996) Time-resolved fluorescence spectroscopy. *Current opinion in structural biology* 6(5):637-642.
37. Mukhopadhyay S, Nayak PK, Udgaonkar JB, & Krishnamoorthy G (2006) Characterization of the formation of amyloid protofibrils from barstar by mapping

residue-specific fluorescence dynamics. *Journal of molecular biology* 358(4):935-942.

38. Ptitsyn O (1995) Molten globule and protein folding. *Advances in protein chemistry* 47(83229.8).

Kinetics of pH-induced unfolding of human β_2-microglobulin

3.1 Introduction

Human β_2-microglobulin (β_2m) is a light chain of the major histocompatibility complex class I (MHC-I) (1). During the recycling of MHC class I molecules from the cell surface, β_2m is released into the bloodstream and is degraded by the kidneys. β_2m accumulates in the blood of the patients suffering from renal failure and undergoing prolonged hemodialysis. The increase in the concentration of β_2m results in the formation and deposition of amyloid fibrils in joints, bones and tendons resulting in a disease namely, dialysis-related amyloidosis (2, 3). However, β_2m monomer remains soluble *in vitro* even at a fairly high concentration under the physiological condition (4). In order to accomplish β_2m aggregation *in vitro*, several conditions have been reported which includes low pH (< pH 4) (5) or addition of denaturing agents or organic solvents (6-8) or metal cations like Cu^{2+} (4, 9). These studies have suggested that the key step is the partial unfolding of the monomeric protein. This type of partially unfolded species are known to assemble to form obligatory oligomeric intermediates that are capable of maturing into amyloid fibrils via nucleated conformational conversion (10-12). Among various solution conditions known to promote fibril formation, low pH is the most widely used condition since the morphological characteristics of fibrils formed at pH 2.5 are similar to that of *ex-vivo* fibrils isolated from the patients (13-15). At pH 2.5, monomeric β_2m exists as an ensemble of highly disordered yet compact conformers (16), resembling a pre-molten-globule like state (17). The pre-molten-globule state is empirically described by the circular dichroism (CD) double-wavelength plot (18) and is more disordered compared to an archetypal molten-globule state observed for many proteins at low pH (19-22). This compact disordered state of β_2m acts as the amyloidogenic precursor to fibrils (5, 13, 16, 23).

β_2m consists of, a disulfide bond and two tryptophan residues, one in the connecting loop between the D and E strands (W60) and the other one (W95) near the C-terminal region (Fig. 3.1) (1, 24). The DE loop containing W60 has been under intense scrutiny due to its important role in amyloidogenesis (25). W60 is solvent-exposed in the native state and is highly conserved due to its functional role in enhancing the conformational flexibility of DE loop that is essential for the optimal binding of β_2m to the MHC-I heavy chain (25, 26). It has been shown that W60G/V mutations in β_2m increase the protein stability compared to that of wild-type (wt) protein and does not promote aggregation under mild conditions (27, 28). On the contrary, W95 is buried inside the hydrophobic pocket at the end of β-strand G, enclosed by Ser11, Asn21, Leu23, Phe70, Pro72 and Tyr78, is involved in the stabilization of the

native protein and has less relevance in fibrillogenesis (29). The previous studies have shown the effect of various mutations (Trp residues) on β_2m stability and aggregation propensity, but the detailed mechanism of pH-induced unfolding of β_2m still remains elusive. In this work, we investigated the pH-induced structural changes of β_2m by utilizing the intrinsic Trp and extrinsic fluorescence and CD spectroscopy. We created single Trp mutants (a) W60 (W95F) and (b) W95 (W60F) for our studies. Our results indicate that the unfolding happens in a stepwise manner involving the initial non-uniform structural expansion of the protein followed by the core-solvation and the dissolution of the secondary structure.

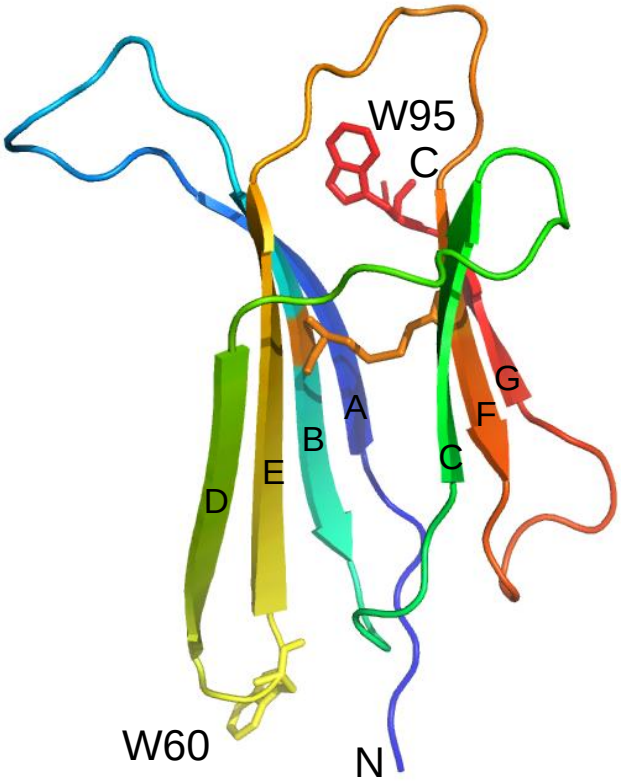

Figure 3.1 Ribbon diagram of human β_2-microglobulin generated from the PDB file 1LDS using PyMol (DeLano Scientific LLC, CA). The indole ring of W60 is exposed to the solvent while that of W95 is buried within the core of the native protein. The tryptophan residue W60 and W95 are shown in yellow and red respectively and the single disulfide bond (C25-C80) is shown as orange stick models. The N- and C-terminal ends are also indicated.

3.2 Experimental section

3.2.1 Materials

Acrylamide, Ethylenediaminetetraacetic acid (EDTA), Guanidine hydrochloride (GdmCl), Tris(hydroxymethyl) aminomethane (Tris), Glycine, Potassium Chloride, Sodium phosphate monobasic dihydrate, Sodium phosphate dibasic dihydrate, Sodium Dodecyl Sulphate (SDS) and 8-anilinonaphthalene-1-sulphonate (ANS) were purchased from Sigma (St. Louis, MO) and used without any additional purification. Isopropyl-β-thiogalactopyranoside (IPTG) and antibiotics (Ampicillin, Tetracycline, and Chloramphenicol) were obtained from Gold Biocom (USA). 6-acryloyl-2-dimethylaminonaphthalene (Acrylodan) was purchased from Molecular Probes, Invitrogen. Q-Sepharose and Superdex 75 10/300 GL column were procured from GE Healthcare Life Sciences (USA). Dialysis tubing (molecular weight cut-off 3.5 kDa) was obtained from Thermo Fisher Scientific (USA).

3.2.2 Cloning, expression, purification, and characterization of protein

β_2m single tryptophan mutants (W60 and W95) were created using overlap extension PCR. The constructs W60 (W95F) and W95 (W60F) was transformed into BL21 (DE3) pLysS *Escherichia coli* strain. Purification of wt protein and mutants were carried out using Q-Sepharose resin followed by gel filtration chromatography as described previously (17).

3.2.3 Steady-state fluorescence measurements

Steady-state fluorescence measurements were performed on FluoroMax-4 (Horiba Jobin Yvon NJ). All measurements were carried out at 24±1 ^{o}C. Protein concentration of 10 µM was used for fluorescence studies and buffer strength was 20mM. For Trp fluorescence experiments, the excitation wavelength was set at 295 nm and excitation and emission bandpass were 0.8 nm and 4 nm, respectively. All the spectra were buffer subtracted. Trp fluorescence anisotropy measurements were performed by setting λ_{ex} at 295 nm (bandpass 1.5 nm) and λ_{em} to 340 nm (bandpass10 nm). An integration time of 1 sec was used to obtain a satisfactory signal-to-noise ratio. The steady-state fluorescence anisotropy was estimated using parallel ($I_{\|}$) and perpendicular ($I_{\perp}$) intensities and the G-factor as follows (30):

$$r = (I_{\|} - I_{\perp}G) / (I_{\|} + 2I_{\perp}G) \quad (3.1)$$

3.2.4 CD measurements

All CD measurements were carried out using a Chirascan CD spectrometer (Applied Photophysics, UK). The concentration of the protein used was 20 μM and the path-length of the cuvette was 1 mm. For variable-temperature CD experiments, the temperature of the protein sample was varied from 20 to 90 °C using a Peltier temperature controller (TC125; Quantum Northwest) with 5 minutes equilibration time at each temperature. The plots were generated using Origin Pro 8 software.

3.2.5 Fluorescence quenching experiments

For Trp fluorescence quenching by acrylamide, a 20μM protein concentration was used. The excitation wavelength was 295 nm (bandpass 0.8 nm) and emission was monitored at 345 nm (bandpass 6nm). The correction for the acrylamide absorbance at 295 nm was performed as reported earlier (31).

Quenching data were analyzed using Stern-Volmer equation (30):

$$F_o/F = 1 + K_{sv}[Q] = 1 + k_q\tau_o[Q] \quad (3.2)$$

Where, F and F_o are the fluorescence intensities in the presence and absence of quencher, respectively, K_{sv} is the Stern-Volmer quenching constant, [Q] is the quencher concentration, k_q is the bimolecular quenching constant and τ_o is the fluorescence lifetime of the fluorophore in the absence of quencher.

3.2.6 Time-resolved fluorescence measurements

The time-resolved fluorescence decay measurements of the samples were performed using a time-correlated single photon counting (TCSPC) setup, Fluorocube from Horiba Jobin Yvon, NJ. The samples were excited using a pulsed light emitting diode (NanoLED-295). The instrument response function was recorded using ludox as a scattering sample and was estimated to be ~ 1ns. The fluorescence was recorded at 345 nm with a slit width of 16 nm. Fluorescence lifetimes were collected at the magic angle (54.7°) with respect to the polarization of the incident light. For fluorescence anisotropy decay measurements, the time-dependent decays of fluorescence were collected at 0° [$I_{\parallel}(t)$] (parallel) and 90° [$I_{\perp}(t)$] (prependicular geometries) with respect to the excitation polarization, and the anisotropy decays were analyzed by globally fitting $I_{\parallel}(t)$ and $I_{\perp}(t)$ as described in our previous reports (32). *G*-factor correction was made for $I_{\perp}(t)$ independently using a free dye in an isotropic

solution such as NATA in water. The anisotropy decays were analyzed using a bi-exponential decay model that takes both fast and slow rotational correlation times into account.

$$r(t) = r_0 [\beta_{fast} \exp(-t/\phi_{fast}) + \beta_{slow} \exp(-t/\phi_{slow})] \quad (3.3)$$

Where r_0 is intrinsic fluorescence anisotropy; ϕ_{fast} &ϕ_{slow} is fast and slow rotational correlation times respectively; β_{fast} & β_{slow} is corresponding amplitudes associated with the fast and slow rotational times, respectively.

3.2.7 Stopped-flow CD and fluorescence experiments

The stopped-flow mixing experiments were carried out on a spectrometer (Chirascan, Applied Photophysics) connected to a stopped-flow apparatus (SF. 3, Applied Photophysics) as reported in our previous study (33). The dead time of mixing for the current setup was ~2.7 ms. The kinetic CD measurements were acquired at 222 nm and 263 nm for 1 sec, and the final protein (wt) concentration was 20 µM. For tryptophan fluorescence kinetics, samples were excited at 295 nm and the total fluorescence was detected using a 320 nm long pass filter. The kinetic traces were acquired for 1 sec with 10,000 time points and were averaged over multiple datasets to give a good signal-to-noise ratio. The final protein concentration used for fluorescence studies was 5 µM.

For acrylamide quenching and ANS binding, all the experiments were carried out on SFM2000 stopped-flow module (Biologic, France). The dead time of mixing is ~2.7 ms. Acrylamide quenching of W95 fluorescence was carried out at 5 µM protein and 200 µM acrylamide concentrations. For ANS binding experiments, wt protein sample was mixed with pH 2.5 buffer containing 10 µM ANS. The sample was excited at 350 nm and fluorescence was collected using a 455 nm long-pass filter. A pH jump from 7.4 $\rightarrow$ 2.5 was achieved by a rapid mixing of β_2m stock solution (10 mM phosphate buffer, pH 7.4) with 55 mM Glycine-HCl buffer (pH 2.5) in 1:10 ratio respectively. Baselines were also collected by mixing the protein stock with pH 7.4 buffer and were used for determining the amplitude of burst-phase. The multiple data sets were averaged, and the data were fitted with the exponential equation using Origin software to obtain the observed rates, and the goodness of fit were assessed by the residual plots.

To obtain the pH dependent titration curve of tryptophan fluorescence, various pH jump experiments were performed. The buffers used were KCl.HCl (1.5 to 2.0), Glycine.HCl (2.5), sodium citrate (3.0 to 6.0) and sodium phosphate (6.5 to 7.0) and the final

concentration of buffers used was 50 mM. The pK_{ax} values of ionizable groups were estimated by fitting the zero-time titration values using the following equation:

$$F_N\ (pH) = F_N^o + \Delta F_N \left[\frac{10^{(pK_{ax} - pH)}}{1 + 10^{(pK_{ax} - pH)}}\right] \quad (3.4)$$

where ΔF_N is the change in fluorescence intensity of tryptophan induced by protonation of the side chain groups, F_N is the fluorescence intensity of Trp in the native state and pK_{ax} is the pK_a values of the (unknown) ionizable side chain groups (34).

3.3 Results

3.3.1 Region-specific conformational changes at low pH

Wt-β_2m contains two Trp residues (W95 and W60), of which W60 is solvent exposed and the W95 is relatively buried. We first created single Trp mutants to monitor the regio-specific structural changes using fluorescence. In order to establish that these mutations do not significantly alter the stability, we carried out thermal denaturation of the variants of β_2m (Fig. 3.2 *a*). The melting temperatures (T_m values) were in accordance with the previous differential scanning calorimetry studies (25). We also showed that the fluorescence property of the individual Trp residues in the native condition and in pH 2.5 is not perturbed by the mutations (Fig. 3.2 *b,c*). Further, the mutants have similar ANS binding in the native as well as in the acid-unfolded state compared to wt (Fig. 3.2 *d,e*).

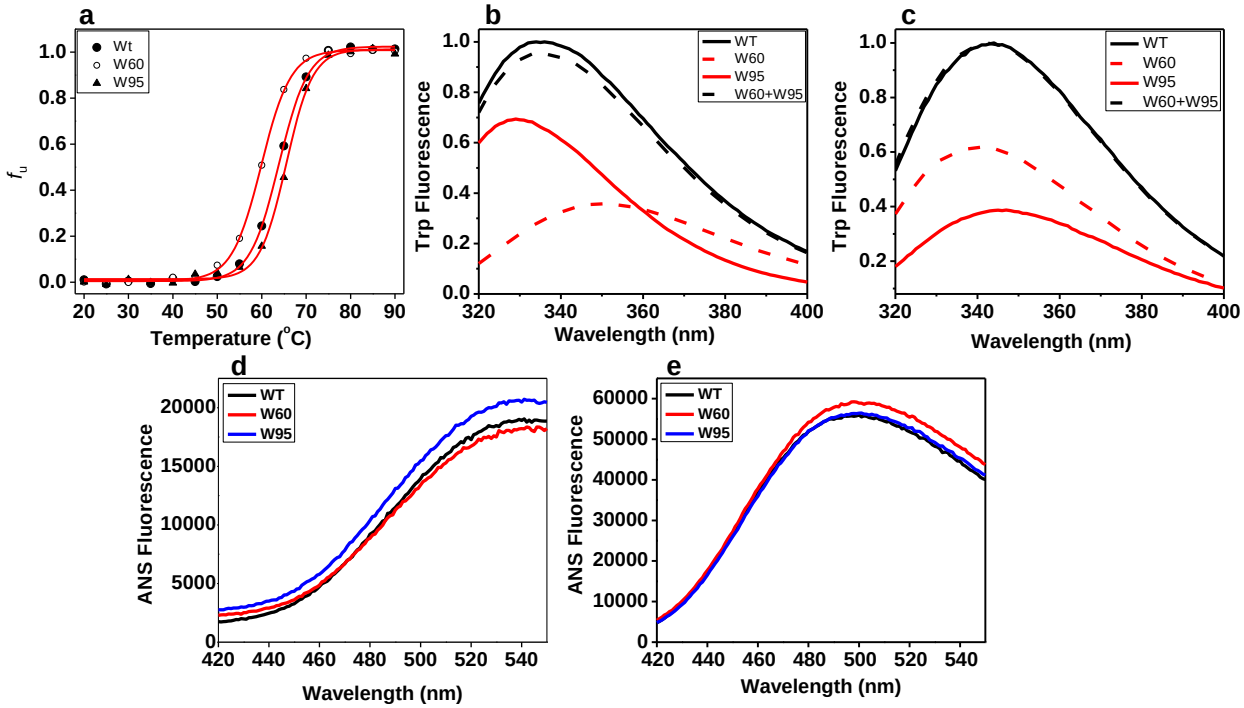

Figure 3.2 Thermal unfolding by CD and Trp fluorescence properties of the wt β_2m and its variants. (a) Changes in the mean residue molar ellipticity at 218 nm are converted to fraction unfolded and plotted as a function of temperature. The solid circle, hollow circle, triangle and inverted triangle in the plot represent the wt, W60 and W95 proteins, respectively. The solid red line through the data is a fit to a Boltzmann function. Changes in the Trp fluorescence spectra of wt and its variants at pH 7(b) and pH 2.5 (c). In each panel, the black solid line, solid red line, dashed red line and dashed black line represents the Trp fluorescence spectra of wt, W95, W60 and combined spectra of W60 and W95, respectively. ANS fluorescence of wt, W60 and W95 protein in the native (d) and pH 2.5 state (e).

After establishing that the single Trp mutants behave like wt-β_2m, we performed the Trp fluorescence measurements at equilibrium. The emission maximum of Trp fluorescence is sensitive to its local environment (30). In the native state at pH 7, W60 has an emission maximum ~350 nm, expected for a solvent exposed Trp, whereas, in the acid-unfolded state, it undergoes a blue shift to ~ 340 nm (Fig. 3.3 *a*) indicating that W60 residue gets partially buried. On the other hand, W95 exhibits a significant red-shift from ~330 nm in the native-form to ~346 nm at pH 2.5 (Fig. 3.3 *b*). This red-shift indicated that the region around W95 residue undergoes a significant loss in structure and is similar to that observed in the chemically denatured state. To further validate our tryptophan fluorescence results, we performed Trp quenching experiments using acrylamide (quencher) which also provides information about the local environment around tryptophan residues in proteins. The Stern-Volmer plots of W60 and W95 mutants under physiological and pH 2.5 conditions are shown in Fig. 3.3 *d,e*. The slope of such a plot provides the Stern-Volmer quenching constant (K_{sv}; Eq. 3.2; Materials and Methods and Table 3.1) which is related to the accessibility of the tryptophan to the quencher. Higher the K_{sv}, higher is the accessibility of fluorophore to the quencher. Since K_{sv} depends on the fluorescence lifetime, the bimolecular quenching constant (k_q) was estimated. (Eq. 3.2; Materials and Methods) (30). The k_q values (Fig. 3.3 *f* & Table 3.1) indicated that under the native condition, W60 residue is highly exposed to the solvent whereas W95 residue is buried inside the hydrophobic pocket of the protein. Upon lowering the pH to 2.5, W60 residue becomes less accessible to the quencher and W95 residue becomes more exposed. The drop in the k_q value at pH 2.5 for W60 signifies the reduced penetration of the quencher around the Trp residue which implies that the W60 residue gets buried into hydrophobic microenvironment. In order to assess the local flexibility of the two regions, we measured the steady-state fluorescence anisotropy of tryptophan. Upon acid-induced unfolding, W60 exhibited higher anisotropy as compared to that of the native state (Fig. 3.3 *c*). Whereas W95 showed lower anisotropy in the acid-unfolded state compared to the native state (Fig. 3.3 *c*). This set of experiments suggested that at low pH, the region around W60 residue attains some non-native local structure which is absent in the native state. On the contrary, the region around W95 is more solvent-exposed and highly flexible resembling the characteristics of the chemically denatured state.

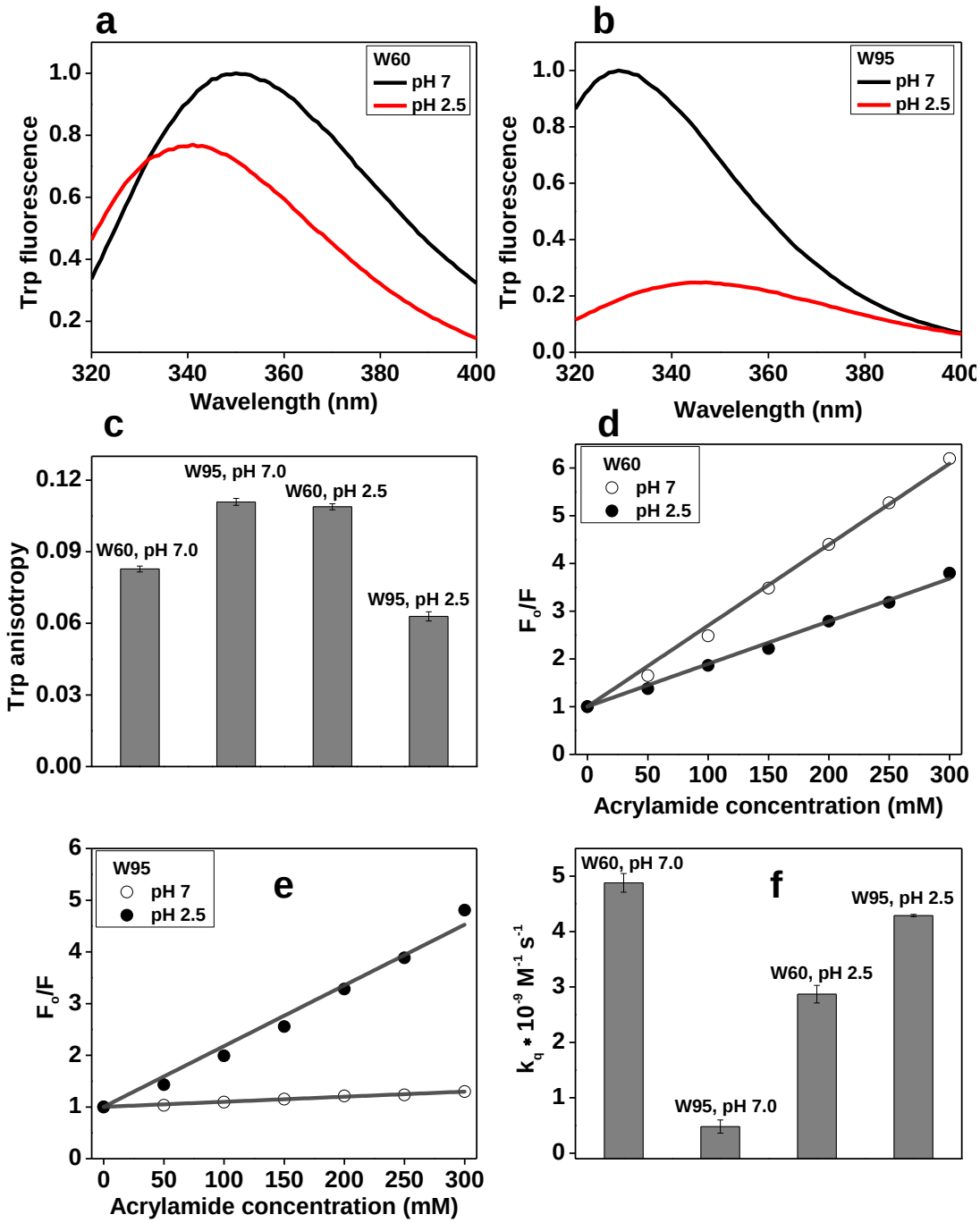

Figure 3.3 Comparison of Trp fluorescence spectra, anisotropy and acrylamide quenching of mutants under different solution conditions. Fluorescence emission spectra of W60 (a) and W95 (b) mutants in the native (pH 7) and acid-unfolded (pH 2.5) states. The spectra are normalized with respect to the native signal at its emission maximum. In each panel, the black solid line represents the fluorescence spectrum of the native and the red solid line represents the acid-unfolded states. (c) Change in the tryptophan fluorescence anisotropy of W60 and W95 mutants at native and acid-unfolded states. (d) Stern-Volmer plots for W60 quenching in the native (open circles) and the acid-unfolded states (solid circles). (e) Stern-Volmer plots for W95 quenching in the native (open circles) and the acid-unfolded states (solid circles). The grey solid lines through the data are fits to a linear equation. (f) Quenching constants for both W60 and W95 in the native and acid-unfolded states.

Table 3.1 Parameters obtained from quenching experiments:

Condition	K_{SV} (M^{-1})	k_q ($*10^9$) M^{-1} s^{-1}
W60, pH 7.0	16.6 ± 0.5	4.9 ± 0.2
W60, pH 2.5	9.3 ± 0.5	2.9 ± 0.2
W95, pH 7.0	1.2 ± 0.3	0.5 ± 0.1
W95, pH 2.5	11.8 ± 0.1	4.3 ± 0.02

3.3.2 Site-specific chain dynamics using fluorescence depolarization kinetics

Since the steady-state anisotropy cannot distinguish between the local and the global motion of the fluorophore, we carried out time-resolved fluorescence anisotropy decay measurements to examine the effects of pH on the rotational dynamics of the two Trp residues. The analysis of the time-resolved anisotropy data provides at least two rotational correlation times: the fast rotational correlation time (ϕ_{fast}) represents the (local) side-chain motion of Trp while the slow rotational correlation time (ϕ_{slow}) corresponds to the global tumbling of the entire protein molecule and is related to the hydrodynamic size by the Stokes-Einstein relationship (Eq. 3.3; Materials and Methods) (30, 35). The amplitude associated with the fast (local) rotational correlation time (β_{fast}) allows us to directly quantify the flexibility at the specific location (36). Under the native condition, both W60 and W95 mutants have similar ϕ_{slow} values (~ 6 ns) and are comparable to that of wt β_2m as reported earlier (Fig. 3.4 *a*,*c* & Table 3.2) (17). This ϕ_{slow} value is expected for native β_2m with the hydrodynamic radius of ~1.9 nm. When the pH of the solution was lowered to 2.5, there was an increase in ϕ_{slow} from ~6 ns to ~8 ns (Fig. 3.4 *b*,*d*). The increase in the global rotational correlation time indicated structural expansion of the protein at low pH from ~1.9 nm to ~ 2.2 nm and is consistent with our previous work on wt-β_2m. The changes in the amplitudes associated with the fast (local) correlation time (β_{fast}) of different single-Trp variants allowed us to monitor the changes in the local mobility upon lowering of pH. W60 exhibited a decrease in β_{fast} from ~0.5 to ~ 0.37 indicating more restricted motion of Trp in the low pH form. On the contrary, W95 showed a considerable increase in β_{fast} from ~ 0.36 to ~ 0.82 indicating significant loss in the local structure. Taken together, our time-resolved fluorescence anisotropy decay measurements suggested that DE loop region near W60 residue undergoes structural rearrangement to form a locally collapsed structure, whereas, the C-terminal region containing W95 undergoes an order-to-disorder transition that results in the increased mobility in the acid-induced state.

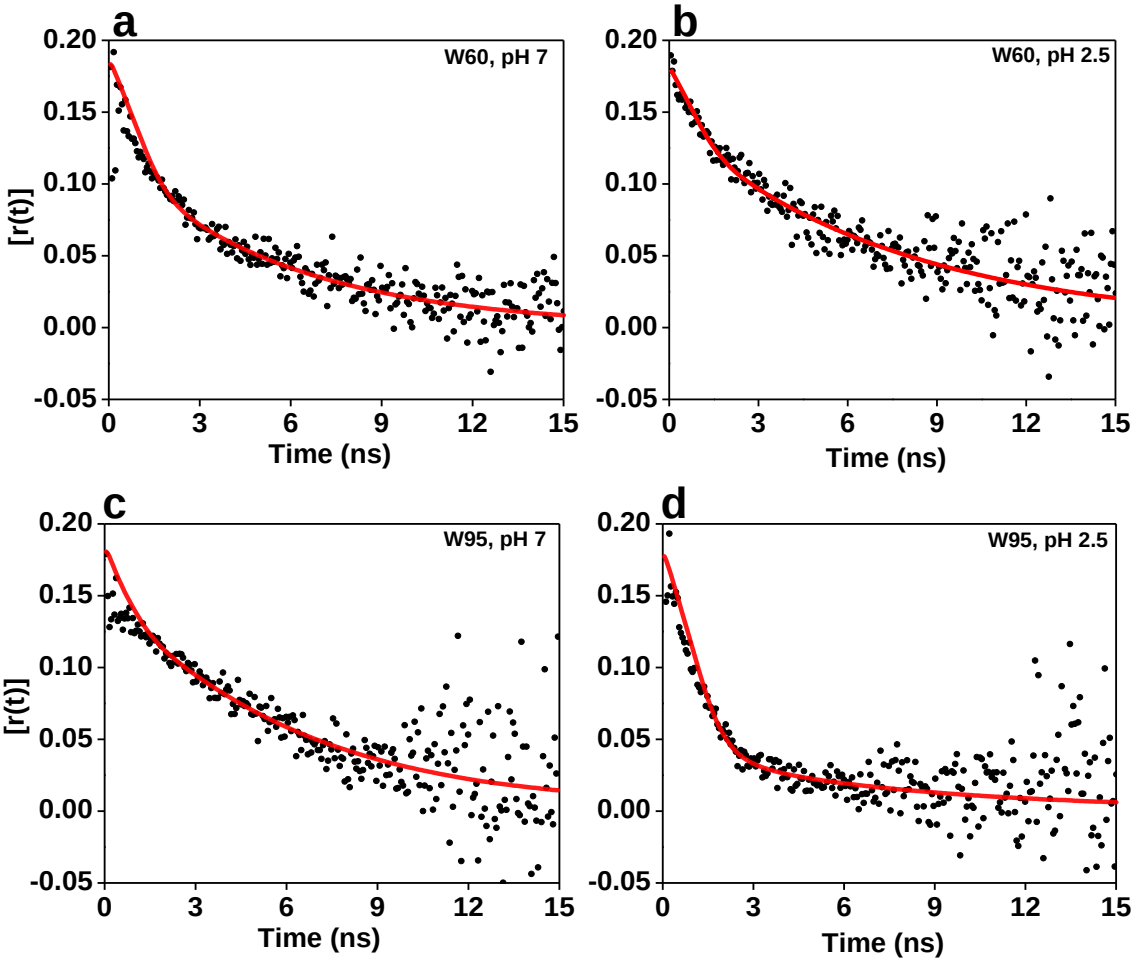

Figure 3.4: Time-resolved fluorescence decays of W60 and W95 in the native and the acid-unfolded states. Tryptophan fluorescence anisotropy decays of W60 mutant in the native (a), and the acid-unfolded (b) states. Tryptophan fluorescence anisotropy decays of W95 mutant in the native (c), and the acid-unfolded states (d). In all the anisotropy decay profiles, scatter points represent the observed decay and the dark red solid line represents the fitted data.

Table 3.2 Typical parameters associated with picosecond time-resolved fluorescence anisotropy decay measurements.

Locations/ Conditions	Rotational correlation times (Φ) and associated amplitudes (β)	
	Φ_{fast} [in ns] (β_{fast})	Φ_{slow} [in ns] (β_{slow})
W60, pH 7	0.3 ± 0.04 (0.5 ± 0.01)	5.5 ± 0.2 (0.5 ± 0.01)
W60, pH 2.5	0.38 ± 0.06 (0.37 ± 0.03)	8 ± 0.6 (0.63 ± 0.03)
W95, pH 7	0.14 ± 0.02 (0.36 ± 0.01)	6.1 ± 0.2 (0.64 ± 0.01)
W95, pH 2.5	0.35 ± 0.02 (0.82 ± 0.02)	7.5 ± 0.2 (0.18 ± 0.02)

3.3.3 Kinetics of chain expansion: the loss of local- and secondary structure

We next carried out pH jump experiments using stopped-flow mixing device to monitor the kinetics of conformational changes from the native- to an acid-unfolded state. To examine the early events of β_2m unfolding, both tryptophan fluorescence and far-UV CD traces were collected. β_2m unfolding was initiated by rapidly mixing the folded form of the protein into an excess of pH 2.5 buffer. Since W60 is solvent-exposed in the native state, we monitored the fluorescence properties of W95 only which is located in the structured region of the protein. Fluorescence intensity of W95 demonstrated a monotonic decrease in fluorescence with a rate constant of ~ 2 s^{-1} after the burst-phase (Fig. 3.5 *a* & Table 3.3). The presence of a burst-phase during the fluorescence kinetics of W95 residue suggests the rapid formation of early intermediate(s). Next, in order to delineate the effects of pH-induced unfolding on the secondary structure, we measured the far-UV CD kinetics of the protein. The CD kinetics, devoid of any burst-phase, could be satisfactorily fitted using a mono-exponential decay (~ 1.8 s^{-1}) that is similar to the unfolding of the C-terminal end of the protein (Fig. 3.5 *b* & Table 3.3). These results indicate that the burst-phase intermediate has an intact secondary structure.

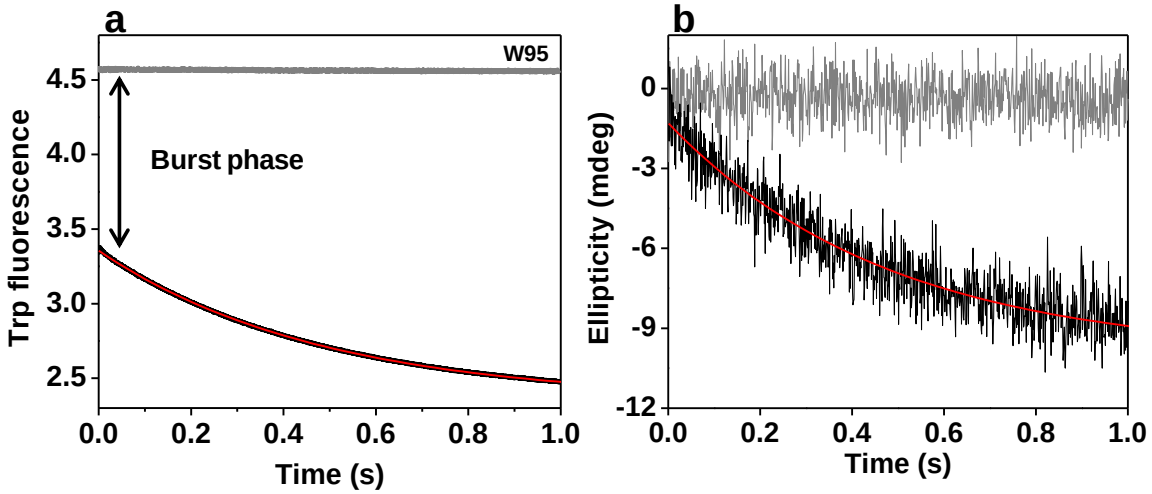

Figure 3.5 Unfolding of protein structure monitored by multiple spectroscopic probes. Kinetic traces observed during unfolding monitored by Trp fluorescence intensity of W95 (a) and far-UV CD signal at 222 nm (b). In each panel, the black line represents the kinetic trace, the red line through the data is a fit to a single exponential equation and the grey line represents the protein baseline.

Table 1.3 Kinetic parameters from stopped-flow kinetic experiments

Structural probes	Burst-phase (%)	k (s^{-1})
W95 fluorescence	54 ± 7	2 ± 0.6
$CD_{@222\ nm}$	_	1.8 ± 0.4
ANS fluorescence	39 ± 6 (30 ± 5) †	2.05 ± 0.1 (2.1 ± 0.1) †

† Our previous work (Ref. 17)

3.3.4 Effect of side-chain protonation in the burst-phase

The sharp drop in the Trp fluorescence of W95 within the burst-phase can be due to water penetration as a result of local unfolding and/or quenching caused by protonation of side chains such as Glu and Asp (37, 38). Since, W95 is partly buried in the native state and therefore the drop in the fluorescence during the burst-phase can possibly be due to the solvation of the Trp residue and/or side-chain protonation of neighboring residues. In order to distinguish between the aforesaid possibilities, we recorded Trp fluorescence kinetics in the absence and in the presence of acrylamide (39). The value of F_o/F that indicates the extent of exposure of the fluorophore to the quencher is similar for both the native state and the burst-phase intermediate (Fig. 3.6 *a*,*b*) indicating the region around W95 is native-like in the burst phase intermediate. Therefore, it seems likely that W95 residue is not exposed to the solvent in the burst-phase intermediate; hence the drop in the fluorescence is possibly due to the side-chain protonation. We further investigated as to how the protonation of nearby residues affects the Trp fluorescence at zero-time (dead-time) as a consequence of pH changes. To obtain the zero-time fluorescence intensity curves for W95, the stopped-flow experiments were performed by mixing buffers of different pH with the native protein. The observed fluorescence changes at different pH values were fitted using a mono-exponential equation (Fig. 3.6 *c*). The zero-time values were extrapolated from the resolved phase and plotted as a function of pH for W95 protein (Fig. 3.6 *d*). The titration data for W95 was fitted by the equation 3.4 (Materials and Methods) and pK_{ax} (unknown groups) was calculated. The pK_{ax} value for W95 is obtained to be ~3.9 and is distinct from the wt β_2m (pK_{ax} 4.3) reported previously (34). This indicates that the protonation of side chains around W95 affects the Trp fluorescence differently compared to the wt protein.

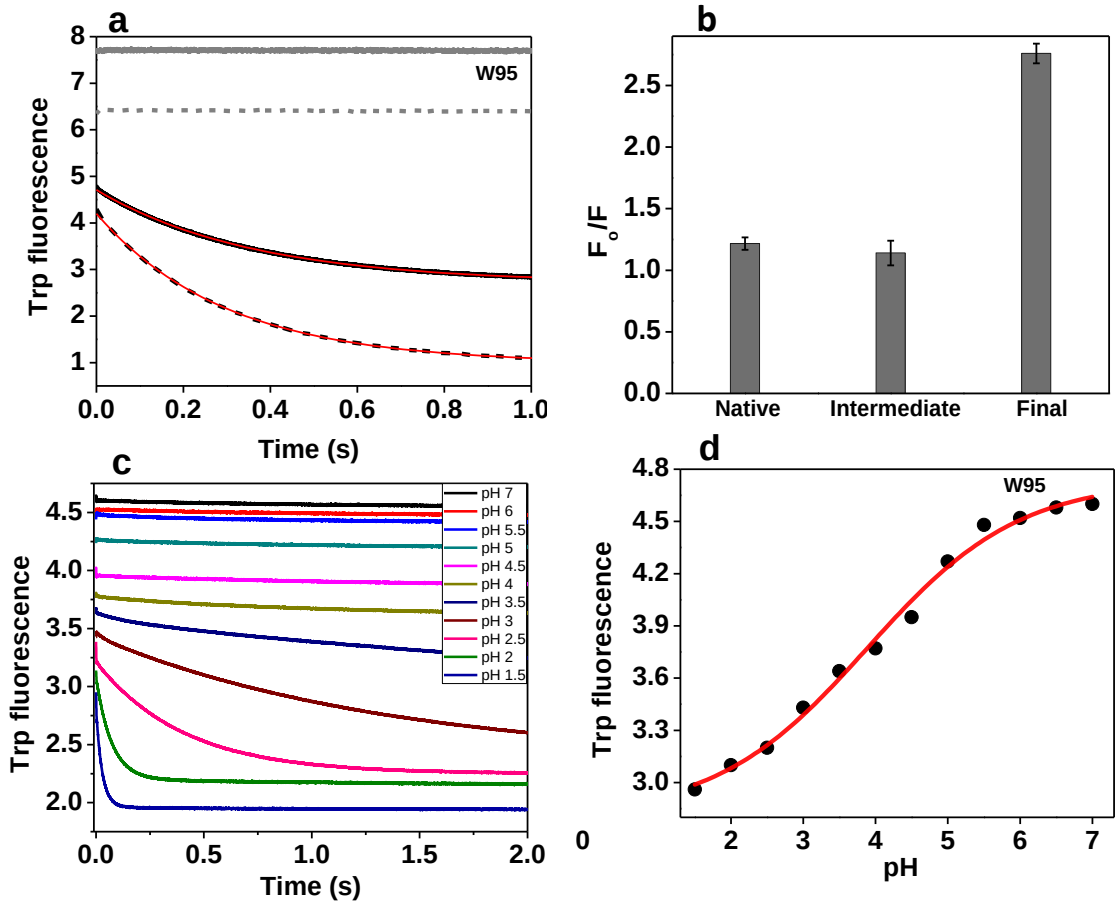

Figure 3.6 (*a*) Unfolding kinetic traces of W95 protein in the absence and presence of 0.2 M acrylamide. The solid and dashed grey lines represent the native signal in the absence and presence of the acrylamide, respectively. The solid and dashed black lines represent the unfolding kinetic traces in the absence and presence of 0.2 M acrylamide, respectively. The solid red line through the data represents the single exponential fit. (*b)* The value of F_o/F in the native, burst-phase intermediate and the end of the reaction. (*c*) Kinetic traces at various pH values were monitored by Trp fluorescence intensity of W95. (*d*) The zero-time fluorescence intensities of W95 protein (filled circles) was plotted as a function of pH. The red line through the data is the fitted titration curve obtained by Eq. 3.4 of Materials and Methods.

3.3.5 Loss of tertiary interaction and core solvation within the burst phase

Next, we used near-UV CD kinetics to monitor the tertiary structural changes within the burst-phase which indicates a rapid loss in the tertiary packing (Fig. 3.7 *a*). These results revealed the fast unpacking of the protein tertiary structure before the secondary structure unfolds and provide evidence for the formation of a expanded native-like burst-phase intermediate. In order to discern whether or not the early loss in the tertiary packing is associated with the solvation of the protein core, we carried out the stopped-flow kinetic

experiments using ANS. ANS fluorescence also exhibited biphasic kinetics (Fig. 3.7 *b*) and the recovered kinetic parameters are in accordance with our previous results (17). The presence of a significant fraction of burst-phase in the ANS fluorescence kinetics and the near-UV CD kinetics together indicates that the early sub-ms phase is likely to involve protein expansion, concomitant with interior solvation.

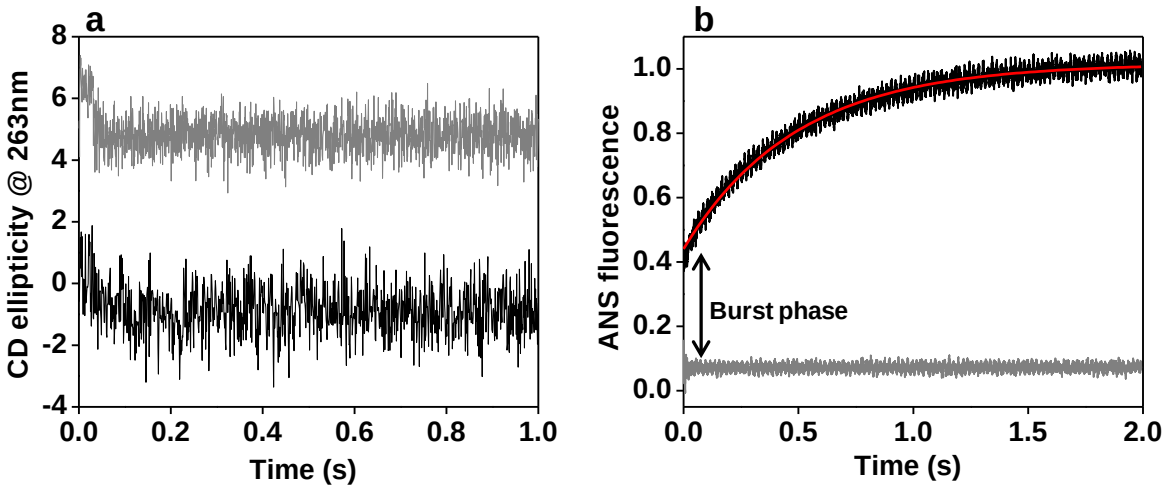

Figure 3.7 Loss of tertiary structure and solvation of the polypeptide chain. Kinetic traces of the unfolding monitored by near-UV CD at 263 nm (*a*). The black solid line represents the kinetic trace and the dark grey line represents the native baseline. (*b*) Change in the ANS fluorescence during pH-induced unfolding. The grey solid line represents the kinetic trace, the black line through the data is a fit to a single- exponential equation and the dark grey line represents the native baseline.

3.4 Discussion

In this work, we have used a series of spectroscopic readouts under equilibrium as well as under kinetic conditions to understand the structure, dynamics and the mechanism of pH-induced unfolding of β_2m. Single Trp and Cys variants allowed us to observe the conformational transitions occurring at various parts of the protein at pH 2.5 under the equilibrium condition. The steady-state and time-resolved Trp fluorescence results suggested that the middle region containing W60 attains a non-native local structure, while the C-terminal end having W95 becomes more solvent exposed and highly flexible at pH 2.5. The non-native local structure formation around W60 could be mediated by a 12-residue sequence stretch spanning from residue 60-71 that has six aromatic residues. This region is known to play an important role in aggregation and the mutations of these aromatic residues significantly affect the formation of residual structure at pH 2.5 (16). This pH-induced disordered state is structurally and dynamically different from the chemically denatured state and is a representative of a complex conformational ensemble that has been described for intrinsically disordered proteins with a persistence of structural preferences (18). The collapsed segments are characterized by a preference for higher chain-chain interactions compared to the chain-solvent interaction (40, 41) which can lead to protein aggregation.

Further, in our kinetic experiments, we have been able to elucidate the mechanism and characterize the early intermediates formed during the pH-induced unfolding. These results demonstrate that pH-induced unfolding of β_2m is not a two state- transition and occurs in two major kinetic phases: unresolved burst-phase (< 2.7 ms) and a slower (~ 500 ms) timescales. The burst-phase intermediate is characterized by intact secondary structural elements but significant loss in the tertiary packing. This early burst-phase intermediate also possesses exposed hydrophobic pockets that are capable of binding to ANS and therefore can be ascribed as a wet molten-globule like state (17). Typically, early unfolding of a protein can occur through the formation of a dry molten-globule that showcases the protein expansion without appreciable core-solvation, followed by the formation of wet-molten and swollen-globules (39, 42-44). In our stopped-flow experiments, the presence of burst-phase in near-UV CD and ANS fluorescence kinetics indicates that the early step involves a concerted unpacking and solvation and is likely to be devoid of a dry globule. Alternatively, it is possible that the dead-time of the stopped-flow mixer is unable to capture the formation of a dry globule. Our data reveal that the native β_2m undergoes a non-uniform expansion during the burst-phase that results in a molten-globule-like intermediate in which one half of the

protein is expanded and solvated, whereas, the C-terminal end harboring W95 experiences a native-like environment. We speculate that during the pH-induced unfolding, the side-chain protonation of β_2m in the burst-phase creates an electrostatic repulsion among the positively charged groups. The presence of electrostatic repulsion causes the loss of salt-bridge interactions leading to the unpacking of the tertiary interactions. The increase in the intramolecular distance and water penetration yield a molten-globule like intermediate that serves as a kinetic intermediate. Interestingly, the burst-phase intermediate shares some characteristics of a folding intermediate of β_2m, which is rarely populated under physiological condition and is a crucial precursor for amyloid fibril formation under physiological condition (45, 46). In the resolved kinetic phase, the structural rearrangement around the C-terminal end containing W95 take place on the similar time scale as compared to the overall dissolution of the secondary structure. Our results provide significant new insights into the mechanism of β_2m unfolding induced by pH change and suggest that local unfolding of the protein without distrupting the secondary structure can be a triggering factor for intermolecular interactions leading to the formation of more stable oligomers and aggregates.

3.5 References

1. Saper, M. A., P. J. Bjorkman, and D. C. Wiley. 1991. Refined structure of the human histocompatibility antigen HLA-A2 at 2.6 A resolution. *J. Mol. Biol.* 219:277-319.
2. Gejyo, F., S. Odani, T. Yamada, N. Honma, H. Saito, Y. Suzuki, Y. Nakagawa, H. Kobayashi, Y. Maruyama, Y. Hirasawa, and et al. 1986. Beta 2-microglobulin: a new form of amyloid protein associated with chronic hemodialysis. Kidney Int 30:385-390.
3. Floege, J., and M. Ketteler. 2001. beta2-microglobulin-derived amyloidosis: an update. Kidney international. Supplement 78:S164-171.
4. Morgan, C. J., M. Gelfand, C. Atreya, and A. D. Miranker. 2001. Kidney dialysis-associated amyloidosis: a molecular role for copper in fiber formation. J Mol Biol 309:339-345.
5. McParland, V. J., N. M. Kad, A. P. Kalverda, A. Brown, P. Kirwin-Jones, M. G. Hunter, M. Sunde, and S. E. Radford. 2000. Partially unfolded states of beta(2)-microglobulin and amyloid formation in vitro. Biochemistry 39:8735-8746.
6. Yamamoto, S., K. Hasegawa, I. Yamaguchi, S. Tsutsumi, J. Kardos, Y. Goto, F. Gejyo, and H. Naiki. 2004. Low concentrations of sodium dodecyl sulfate induce the extension of beta 2-microglobulin-related amyloid fibrils at a neutral pH. Biochemistry 43:11075-11082.
7. Yamamoto, S., I. Yamaguchi, K. Hasegawa, S. Tsutsumi, Y. Goto, F. Gejyo, and H. Naiki. 2004. Glycosaminoglycans enhance the trifluoroethanol-induced extension of beta 2-microglobulin-related amyloid fibrils at a neutral pH. J Am Soc Nephrol 15:126-133.
8. Yamaguchi, K., H. Naiki, and Y. Goto. 2006. Mechanism by which the amyloid-like fibrils of a beta 2-microglobulin fragment are induced by fluorine-substituted alcohols. J Mol Biol 363:279-288.
9. Eakin, C. M., J. D. Knight, C. J. Morgan, M. A. Gelfand, and A. D. Miranker. 2002. Formation of a copper specific binding site in non-native states of beta-2-microglobulin. Biochemistry 41:10646-10656.
10. Serio, T. R., A. G. Cashikar, A. S. Kowal, G. J. Sawicki, J. J. Moslehi, L. Serpell, M. F. Arnsdorf, and S. L. Lindquist. 2000. Nucleated conformational conversion and the replication of conformational information by a prion determinant. Science 289:1317-1321.

11. Knowles, T. P., M. Vendruscolo, and C. M. Dobson. 2014. The amyloid state and its association with protein misfolding diseases. Nat Rev Mol Cell Biol 15:384-396.
12. Lee, J., E. K. Culyba, E. T. Powers, and J. W. Kelly. 2011. Amyloid-β forms fibrils by nucleated conformational conversion of oligomers. Nature chemical biology 7:602-609.
13. Jahn, T. R., G. A. Tennent, and S. E. Radford. 2008. A common beta-sheet architecture underlies in vitro and in vivo beta2-microglobulin amyloid fibrils. J Biol Chem 283:17279-17286.
14. Platt, G. W., and S. E. Radford. 2009. Glimpses of the molecular mechanisms of beta2-microglobulin fibril formation in vitro: aggregation on a complex energy landscape. FEBS Lett 583:2623-2629.
15. Su, Y., C. J. Sarell, M. T. Eddy, G. T. Debelouchina, L. B. Andreas, C. L. Pashley, S. E. Radford, and R. G. Griffin. 2014. Secondary structure in the core of amyloid fibrils formed from human beta(2)m and its truncated variant DeltaN6. J Am Chem Soc 136:6313-6325.
16. Platt, G. W., V. J. McParland, A. P. Kalverda, S. W. Homans, and S. E. Radford. 2005. Dynamics in the unfolded state of beta2-microglobulin studied by NMR. J Mol Biol 346:279-294.
17. Narang, D., P. K. Sharma, and S. Mukhopadhyay. 2013. Dynamics and dimension of an amyloidogenic disordered state of human beta(2)-microglobulin. Eur Biophys J 42:767-776.
18. Uversky, V. N. 2002. Natively unfolded proteins: a point where biology waits for physics. Protein science 11:739-756.
19. Semisotnov, G. V., N. A. Rodionova, O. I. Razgulyaev, V. N. Uversky, A. F. Gripas, and R. I. Gilmanshin. 1991. Study of the "molten globule" intermediate state in protein folding by a hydrophobic fluorescent probe. Biopolymers 31:119-128.
20. Morozova, L. A., D. T. Haynie, C. Arico-Muendel, H. Van Dael, and C. M. Dobson. 1995. Structural basis of the stability of a lysozyme molten globule. Nat Struct Biol 2:871-875.
21. Kelkar, D. A., A. Chaudhuri, S. Haldar, and A. Chattopadhyay. 2010. Exploring tryptophan dynamics in acid-induced molten globule state of bovine alpha-lactalbumin: a wavelength-selective fluorescence approach. Eur Biophys J 39:1453-1463.

22. Bom, A. P., M. S. Freitas, F. S. Moreira, D. Ferraz, D. Sanches, A. M. Gomes, A. P. Valente, Y. Cordeiro, and J. L. Silva. 2010. The p53 core domain is a molten globule at low pH: functional implications of a partially unfolded structure. J Biol Chem 285:2857-2866.
23. Gosal, W. S., I. J. Morten, E. W. Hewitt, D. A. Smith, N. H. Thomson, and S. E. Radford. 2005. Competing pathways determine fibril morphology in the self-assembly of beta2-microglobulin into amyloid. J Mol Biol 351:850-864.
24. Becker, J. W., and G. N. Reeke, Jr. 1985. Three-dimensional structure of beta 2-microglobulin. *Proc. Natl. Acad. Sci. USA* 82:4225-4229.
25. Kihara, M., E. Chatani, K. Iwata, K. Yamamoto, T. Matsuura, A. Nakagawa, H. Naiki, and Y. Goto. 2006. Conformation of amyloid fibrils of beta2-microglobulin probed by tryptophan mutagenesis. J Biol Chem 281:31061-31069.
26. Hodkinson, J. P., T. R. Jahn, S. E. Radford, and A. E. Ashcroft. 2009. HDX-ESI-MS reveals enhanced conformational dynamics of the amyloidogenic protein beta(2)-microglobulin upon release from the MHC-1. J Am Soc Mass Spectrom 20:278-286.
27. Ricagno, S., M. Colombo, M. de Rosa, E. Sangiovanni, S. Giorgetti, S. Raimondi, V. Bellotti, and M. Bolognesi. 2008. DE loop mutations affect beta2-microglobulin stability and amyloid aggregation. Biochem Biophys Res Commun 377:146-150.
28. Santambrogio, C., S. Ricagno, M. Colombo, A. Barbiroli, F. Bonomi, V. Bellotti, M. Bolognesi, and R. Grandori. 2010. DE-loop mutations affect beta2 microglobulin stability, oligomerization, and the low-pH unfolded form. Protein Sci 19:1386-1394.
29. Raimondi, S., N. Barbarini, P. Mangione, G. Esposito, S. Ricagno, M. Bolognesi, I. Zorzoli, L. Marchese, C. Soria, R. Bellazzi, M. Monti, M. Stoppini, M. Stefanelli, P. Magni, and V. Bellotti. 2011. The two tryptophans of beta2-microglobulin have distinct roles in function and folding and might represent two independent responses to evolutionary pressure. BMC Evol Biol 11:159.
30. Lakowicz, J. R. 2007. Principles of fluorescence spectroscopy. Springer Science & Business Media.
31. Tallmadge, D. H., J. S. Huebner, and R. F. Borkman. 1989. Acrylamide quenching of tryptophan photochemistry and photophysics. Photochem Photobiol 49:381-386.
32. Jain, N., M. Bhattacharya, and S. Mukhopadhyay. 2011. Chain collapse of an amyloidogenic intrinsically disordered protein. Biophys J 101:1720-1729.
33. Bhattacharya, M., and S. Mukhopadhyay. 2012. Structural and dynamical insights into the molten-globule form of ovalbumin. J Phys Chem B 116:520-531.

34. Mukaiyama, A., T. Nakamura, K. Makabe, K. Maki, Y. Goto, and K. Kuwajima. 2013. The molten globule of beta(2)-microglobulin accumulated at pH 4 and its role in protein folding. J Mol Biol 425:273-291.
35. Jain, N., and S. Mukhopadhyay. 2015. Applications of Fluorescence Anisotropy in Understanding Protein Conformational Disorder and Aggregation. In Applied Spectroscopy and the Science of Nanomaterials. Springer. 41-57.
36. Mukhopadhyay, S., P. K. Nayak, J. B. Udgaonkar, and G. Krishnamoorthy. 2006. Characterization of the formation of amyloid protofibrils from barstar by mapping residue-specific fluorescence dynamics. Journal of molecular biology 358:935-942.
37. Ricci, R. W., and J. M. Nesta. 1976. Inter-and intramolecular quenching of indole fluorescence by carbonyl compounds. The Journal of Physical Chemistry 80:974-980.
38. Chen, Y., and M. D. Barkley. 1998. Toward understanding tryptophan fluorescence in proteins. Biochemistry 37:9976-9982.
39. Sarkar, S. S., J. B. Udgaonkar, and G. Krishnamoorthy. 2013. Unfolding of a small protein proceeds via dry and wet globules and a solvated transition state. Biophys J 105:2392-2402.
40. Pappu, R. V., X. Wang, A. Vitalis, and S. L. Crick. 2008. A polymer physics perspective on driving forces and mechanisms for protein aggregation. Archives of biochemistry and biophysics 469:132-141.
41. Mao, A. H., N. Lyle, and R. V. Pappu. 2013. Describing sequence-ensemble relationships for intrinsically disordered proteins. Biochem J 449:307-318.
42. Jha, S. K., and S. Marqusee. 2014. Kinetic evidence for a two-stage mechanism of protein denaturation by guanidinium chloride. Proc Natl Acad Sci U S A 111:4856-4861.
43. Finkelstein, A. V., and E. I. Shakhnovich. 1989. Theory of cooperative transitions in protein molecules. II. Phase diagram for a protein molecule in solution. Biopolymers 28:1681-1694.
44. Baldwin, R. L., C. Frieden, and G. D. Rose. 2010. Dry molten globule intermediates and the mechanism of protein unfolding. Proteins 78:2725-2737.
45. Jahn, T. R., M. J. Parker, S. W. Homans, and S. E. Radford. 2006. Amyloid formation under physiological conditions proceeds via a native-like folding intermediate. Nature structural & molecular biology 13:195-201.
46. Gershenson, A., L. M. Gierasch, A. Pastore, and S. E. Radford. 2014. Energy landscapes of functional proteins are inherently risky. Nat Chem Biol 10:884-891.

Effect of salt on the aggregation mechanism of human β_2-microglobulin

4.1 Introduction

Protein misfolding and aggregation can result in amyloid formation and is implicated in a large number of human diseases which includes cystic fibrosis, Type Π diabetes, dialysis-related amyloidosis and neurodegenerative diseases such as spongiform transmissible encephalopathy's, Alzheimer's and Parkinson's diseases (1, 2). The amyloid state of various proteins shares a common architecture in which the main β-strands run perpendicular to the fibril axis (3, 4). The fact that nearly all proteins can access the amyloid state, whether they are disease-associated or not, indicates that amyloid formation is a generic property and is independent of the native structure of the protein (5-9). Despite, the similarity in the cross-β diffraction pattern, fibrils formed from a single polypeptide chain can adopt distinct conformations which cause the differences in phenotypes and pathology (10-13). The conformational diversity in amyloid fibrils can originate due to differences in the number of protofilaments (14) or in the helicity (15) or arrangements of β-strands and turns in the β-sheets (16).

The amyloid assembly of proteins appear to proceed from the formation and accumulation of aggregation-competent partially folded conformations (17-19). The partially folded monomers associate together to form oligomers that are typically more toxic than the final amyloid state (20-22). The structures and properties of such oligomeric aggregates can be heterogeneous and this heterogeneity can be the potential reason for amyloid polymorphism. It is possible that certain conditions favor one type of oligomeric species over the other and give rise to distinct amyloid morphology and structure. The important variables that can induce amyloid polymorphism *in vitro* are salts (23, 24), trifluoroethanol (25, 26) and temperature (27). It is of great importance to understand the structure of these initial oligomers or nucleating species which regulates the amyloid formation and polymorphism.

Human β_2-microglobulin (β_2m) at pH 2.5 exists as a partially folded state with significant loss of secondary structure (28) resembling a pre-molten-globule like state (29) and acts as an amyloidogenic precursor for amyloid formation (24, 30, 31). In the presence of varying concentrations of salt (sodium chloride) at pH 2.5, β_2m forms amyloid fibrils with distinct morphologies. At low salt concentration (~50 mM), it forms long and straight fibrils, whereas at high salt (above 200 mM) concentrations, it forms worm-like fibrils (24).

In this study, we have investigated the effect of salt concentrations on the acid-unfolded state of β_2m using a diverse array of structural probes. Our 4-(dicyanovinyl)-julolidine (DCVJ) and dynamic light scattering results show that at low salt concentrations

(≤100 mM), β_2m remains as a monomer, whereas high salt concentrations facilitates oligomerization and is supported by glutaraldehyde crosslinking assay. Circular dichroism and 1-anilinonaphthalene-8-sulfonate (ANS) lifetime results imply that the oligomer formation is accompanied by an increase in α-helical content and hydrophobicity. Site-specific information obtained from single Trp mutants indicate that residue W60 gets buried in the hydrophobic structure as the salt concentration increases, while W95 remains exposed. The kinetics of oligomerization was further monitored by using DCVJ and ANS fluorescent probes. The drop in ANS fluorescence in the burst phase suggests the loss of existing hydrophobic patches. After the burst phase, both DCVJ and ANS fluorescence have similar rates indicating the concurrent formation of oligomers and hydrophobic patches.

4.2 Experimental section

4.2.1 Material

Ethylenediaminetetraacetic acid (EDTA), Urea, Tris(hydroxymethyl) aminomethane (Tris), Glycine, Sodium phosphate monobasic dihydrate, Sodium phosphate dibasic dihydrate, 8-anilinonaphthalene-1-sulphonate (ANS) and 9-(2,2-Dicyanovinyl) julolidine (DCVJ) were purchased from Sigma (St. Louis, MO) and used without any additional purification. Glutaraldehyde was purchased from spectrochem, India. Isopropyl-thiogalactopyranoside (IPTG) and antibiotics (Ampicillin, Tetracycline, and Chloramphenicol) were obtained from Gold Biocom (USA). Q-Sepharose and Superdex 75 10/300 GL column were procured from GE Healthcare Life Sciences (USA). Dialysis tubing (molecular weight cut-off 3.5 kDa) was obtained from Thermo Fisher Scientific (USA).

4.2.2 Steady-state fluorescence Measurements

Steady-state fluorescence measurements were carried out on FluoroMax-4 (Horiba Jobin Yvon NJ) spectrofluorometer at room temperature. All the readings for experiments were taken just after adding the salt in pH 2.5 protein solution. The final protein concentration was 20 µM and DCVJ concentration used was 5 µM. The buffer used was pH 2.5 Gly.HCl (25 mM) buffer. For Trp fluorescence experiments, the excitation wavelength (λ_{ex}) was set at 295 nm and excitation and emission bandpass were 0.8 nm and 5 nm, respectively. For DCVJ fluorescence experiments, the excitation wavelength was set at 453 nm and excitation and emission bandpass were 0.8 nm and 4 nm respectively.

4.2.3 Circular dichroism Measurements

All Far-UV CD spectra were recorded on a Chirascan CD spectrometer (Applied Photophysics, UK) at room temperature. The concentration of the protein used was 20 µM in Gly.HCl buffer (25 mM), pH 2.5. All the spectra were recorded in the range of 200-260 nm and buffer subtracted.

4.2.4 Dynamic light scattering

The DLS experiment was performed on a Malvern Instruments Zetasizer Nano-ZS instrument. This technique yields a hydrodynamic diameter calculated using the Stokes-Einstein equation. The mean particle diameter is calculated by the software from the particle

distributions measured. The protein concentration used was 50 µM and buffers were Gly.HCl buffer (25 mM), pH 2.5 and phosphate buffer (10 mM), pH 7.0.

4.2.5 Time-resolved fluorescence measurements

Time-resolved fluorescence decay measurements of the samples were performed using a time-correlated single photon counting (TCSPC) setup, Fluorocube from Horiba Jobin Yvon, NJ. All measurements were carried out at 25 ^{o}C. Protein and ANS concentrations used for the experiments were 20 µM each. The samples were excited using a 375 nm pulsed laser diode and the instrument response function was recorded using ludox as a scattering sample and was estimated to be ~ 250 ps. ANS fluorescence was collected at 520 nm with 6 nm bandpass. The fluorescence intensity decays (I(t) vs. t) were collected at the magic angle (54.7°) with respect to the polarization of the incident light.

4.2.6 Stopped-flow experiments

The stopped-flow mixing experiments were carried out on SFM 2000 stopped-flow module (Biologic, France). The dead-time of mixing is ~1.4 ms. For DCVJ and ANS binding, 40 µM protein solution in pH 2.5 Gly.HCl (25 mM) buffer was mixed with the same buffer containing salt and 10 µM of DCVJ or 20 µM ANS in a 1:1 ratio. After mixing in the stopped-flow apparatus, the concentrations of protein, DCVJ and ANS were 20 µM, 5 µM and 10 µM respectively. For DCVJ experiments, samples were excited at 453 nm and fluorescence was collected using a 475 nm long-pass filter. For ANS binding experiments, samples were excited at 350 nm and fluorescence was collected using a 455 nm long-pass filter. Baselines were also collected by mixing the protein solution with buffer containing dye and used for determining the amplitude of burst-phase. The multiple data sets were averaged, and the data were fitted with the exponential equation using origin software to obtain the observed rates.

4.3 Results

4.3.1 Formation of oligomers monitored by DCVJ fluorescence, light scattering and glutaraldehyde crosslinking

The probe, DCVJ, is a molecular rotor and shows reasonable binding affinity to the early amyloidogenic oligomers (32). It consists of a fluorescent julolidine moiety and an intrinsic dicyano quencher. In solution, the freely rotating cyanide group quenches the fluorescence, whereas binding to oligomers imparts rotational constraints that result in concomitant increase in the fluorescence quantum yield. We employed DCVJ fluorescent probe to investigate the initial β_2m oligomer formation as a function of varying salt concentrations. Fluorescence spectra of DCVJ bound to oligomers formed at different salt concentrations are shown in Fig. 4.1 *a*. The DCVJ probe has a poor binding affinity to the acid-unfold state in the absence and the presence of low salt concentrations (≤ 100 mM) (Fig. 4.1 *b*). Above 100 mM salt concentrations, DVCJ fluorescence increases significantly indicating the formation of oligomeric species (Fig. 4.1 *b*). The increase in DCVJ fluorescence intensity as a function of salt indicates either an increase in the oligomers population or oligomer size or both. These results signify that at low salt concentrations (≤ 100 mM), β_2m predominantly remains in the monomeric form and begins to oligomerize at higher salt concentrations (≥ 100 mM).

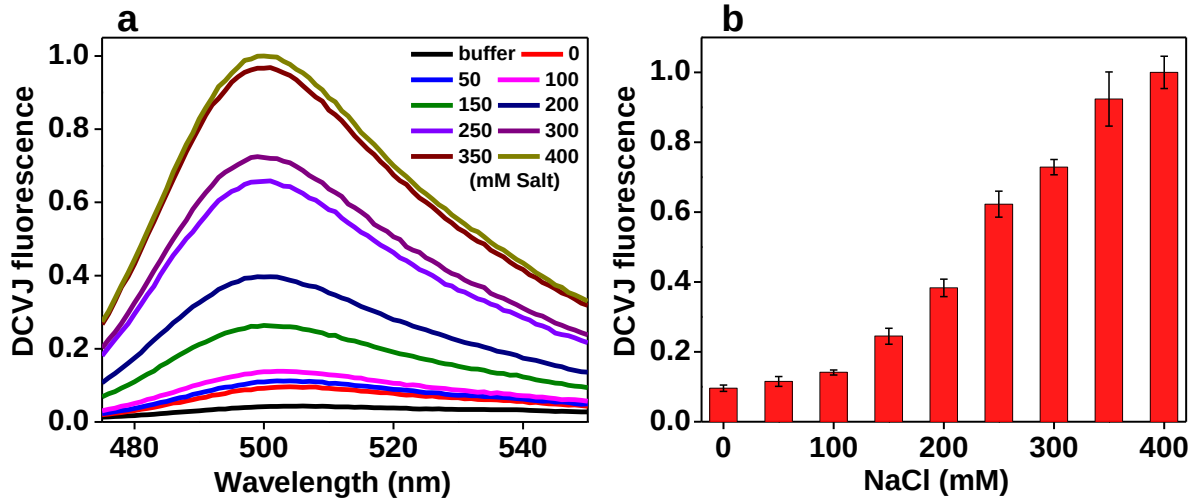

Figure 4.1 Salt-induced oligomers formation monitored by DCVJ fluorescence and dynamic light scattering. (a) DCVJ fluorescence spectra of the acid-unfolded state as a function of increasing salt concentrations. (b) DCVJ fluorescence intensity at 500 nm wavelength as a function of increasing salt concentrations.

Next, in order to monitor the size of the oligomers formed, we used dynamic light scattering. The intensity size distributions of the protein were measured in the native and acid-unfolded state in the absence and presence of different salt concentrations. In the native state, the intensity distribution presents a single peak with the average hydrodynamic diameter (D_H) ~ 4.2 nm (Fig. 4.2 *a*). In the acid-unfolded state and in the presence of 50 mM salt, the intensity distribution curve shows a peak ~ 6.5 nm signifying the formation of expanded polypeptide chain due to protein unfolding (Fig. 4.2 *a*). On the contrary at 400 mM salt concentration, the intensity size distribution shows a broad peak ~ 11.7 nm (Fig. 4.2 *a*). The increase in the average hydrodynamic diameter at higher salt concentration indicates the formation of oligomers which corroborates well with the DCVJ fluorescence measurements. Further, our glutaraldehyde cross-linking assay suggests the formation of high molecular weight species at 400 mM salt concentration, whereas in the absence and at low salt concentrations, there were no detectable high molecular weight oligomers (Fig. 4.2 *b*).

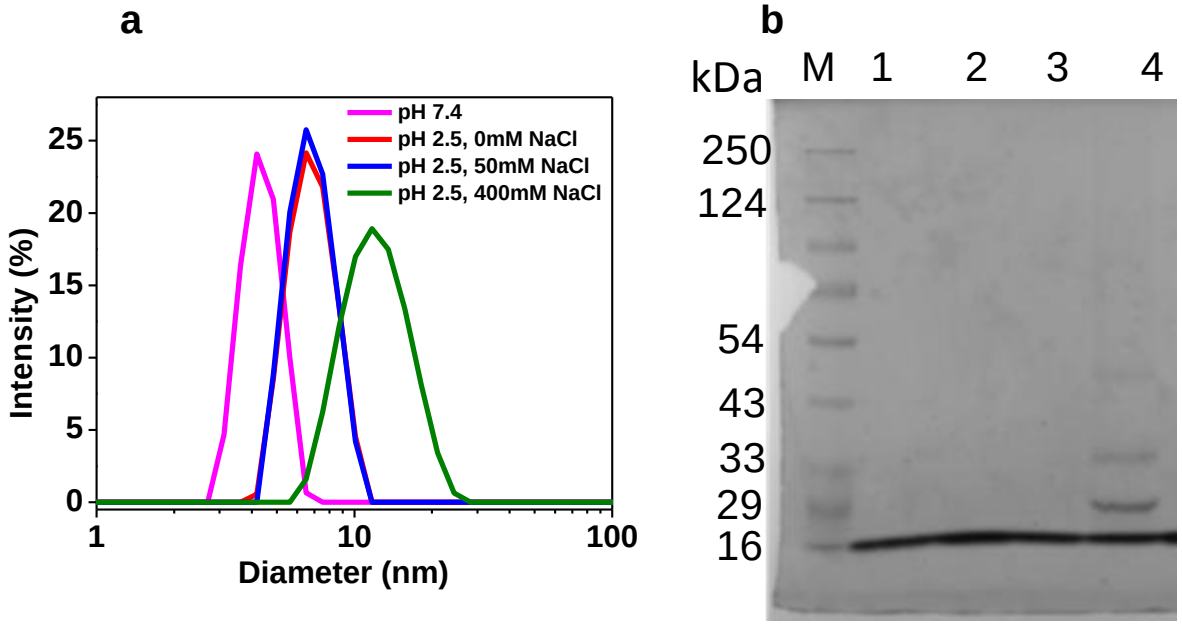

Figure 4.2 (a) The mean hydrodynamic diameter of wt β_2m at pH 7.0, pH 2.5 and pH 2.5 in the presence of 50 mM and 400 mM salt. (b) SDS-PAGE analysis of 0.1% glutaraldehyde crosslinking of 50 µM β_2m protein. The reaction was carried at room temperature for 10 min. After 10 min, SDS-PAGE loading dye was added to the reaction mixture and the samples were boiled at 100 °C for 5 min. Then the samples were allowed to run on 12 % SDS-PAGE. Lane: (M) Protein ladder (1) β_2m in pH 7.4 buffer (2) β_2m in pH 2.5 buffer (3) β_2m in pH 2.5 buffer and 50 mM salt (4) β_2m in pH 2.5 buffer and 400 mM salt. The samples in lane 2, 3 and 4 have 0.1% glutaraldehyde

4.3.2 Structural changes probed by ANS fluorescence and circular dichroism

To gain insights into the structural changes upon oligomerization, we assessed their hydrophobicity and secondary structural content. ANS probe has a highly environment-sensitive fluorescence and shows high quantum yield when bound to hydrophobic patches (33). We monitored the ANS fluorescence lifetime bound to different states of β_2m formed under varying salt concentrations. Fig. 4.3 *a* shows the ANS fluorescence intensity decay bound to β_2m at different salt concentrations. At pH 2.5 without salt, the mean fluorescence lifetime of the acid-unfolded state is ~2.3 ns similar to previously reported values (29). Upto to 100 mM salt, there is no significant increase in the mean ANS fluorescence lifetime, whereas beyond 100 mM salt, there is progressive increase in the ANS lifetime indicating the formation of more hydrophobic patches in the molten globule oligomers (Fig. 4.3 *b*).

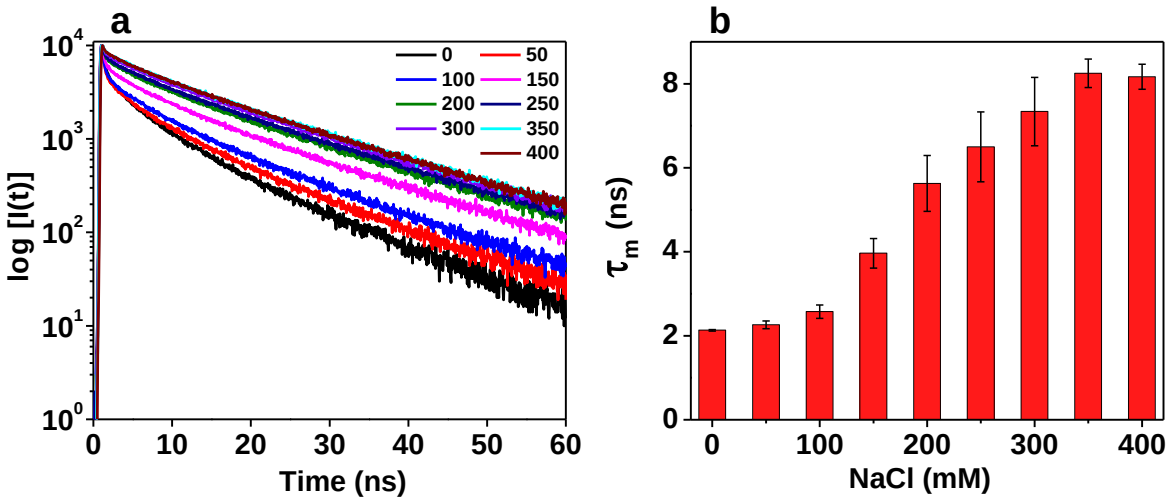

Figure 4.3 Salt-induced hydrophobicity changes in the acid-unfolded state of β_2m (a) Time-resolved fluorescence intensity decay of ANS bound to β_2m at salt concentrations ranging from 0 to 400 mM. (b) Mean fluorescence lifetime of ANS bound to β_2m.

To understand whether these hydrophobic patches are solvent exposed or buried, we compared the components of ANS fluorescence lifetime. The ANS in water shows mono-exponential decay with a typical fluorescence lifetime of 0.25 ns (34). Upon binding to a protein, ANS fluorescence shows two longer lifetime components that reflect the two different dye-protein complexes. The shorter lifetime component (τ < 10 ns) of ANS fluorescence decay arises from the fluorophores that are bound to water-exposed superficial hydrophobic patches. However, the long lifetime component (τ > 10 ns) of ANS fluorescence decay is a characteristic of dye molecules which interact with the solvent-protected hydrophobic core patches (34). As the salt concentration increases, there is a significant

enhancement in the lifetime of the two components from ~4 ns to ~7 ns and ~12 ns to ~18 ns demonstrating that the hydrophobic patches are becoming more solvent-protected (Table 4.1). Moreover, the contribution of the long lifetime component ($\tau > 10$ ns) increases from ~10% to 36%, whereas the contribution of the short lifetime ($\tau < 10$ ns) component remain the same (Table 4.1). Therefore, these results suggest that during oligomerization, there is an increase in the fraction of solvent-protected hydrophobic patches, whereas the fraction of surface-exposed hydrophobic patches remains the same.

Table 4.1 Time-resolved fluorescence lifetimes of ANS bound to β_2m at different salt concentrations.

Condition [NaCl] (mM)	ANS fluorescence lifetime in ns (amplitude)			τ_m (ns)	λ^2
	τ_1 (α_1)	τ_2 (α_2)	τ_3 (α_3)		
0	12.4 (0.09)	4.0 (0.2)	0.29 (0.71)	2.13	1.27
50	14.0 (0.10)	4.5 (0.16)	0.28 (0.75)	2.26	1.26
100	15.2 (0.11)	5.1 (0.15)	0.28 (0.74)	2.57	1.19
150	16.8 (0.17)	5.7 (0.17)	0.27 (0.66)	3.96	1.17
200	17.5 (0.24)	6.2 (0.19)	0.27 (0.56)	5.63	1.21
250	17.7 (0.28)	6.4 (0.21)	0.30 (0.51)	6.50	1.11
300	17.9 (0.32)	6.8 (0.22)	0.32 (0.46)	7.34	1.14
350	17.9 (0.36)	6.8 (0.23)	0.32 (0.40)	8.25	1.20
400	17.9 (0.36)	6.9 (0.23)	0.27 (0.41)	8.12	1.18

Next, we investigated the secondary structural changes upon oligomers formation facilitated by the salt. At pH 2.5, β_2m exhibits an unfolded state with loss of most of the secondary structure content. As the salt concentration increases, the far-UV CD measurements indicated the formation of α-helical content in the oligomers (Fig. 4.4 *a*). The ratiometric CD plot (222/208) also indicated an increase in the α-helical content in the oligomers (Fig. 4.4 *b*). Taken together, these results signify that the oligomer formation is accompanied by the rearrangement of protein structure to form new hydrophobic and α-helical rich structures.

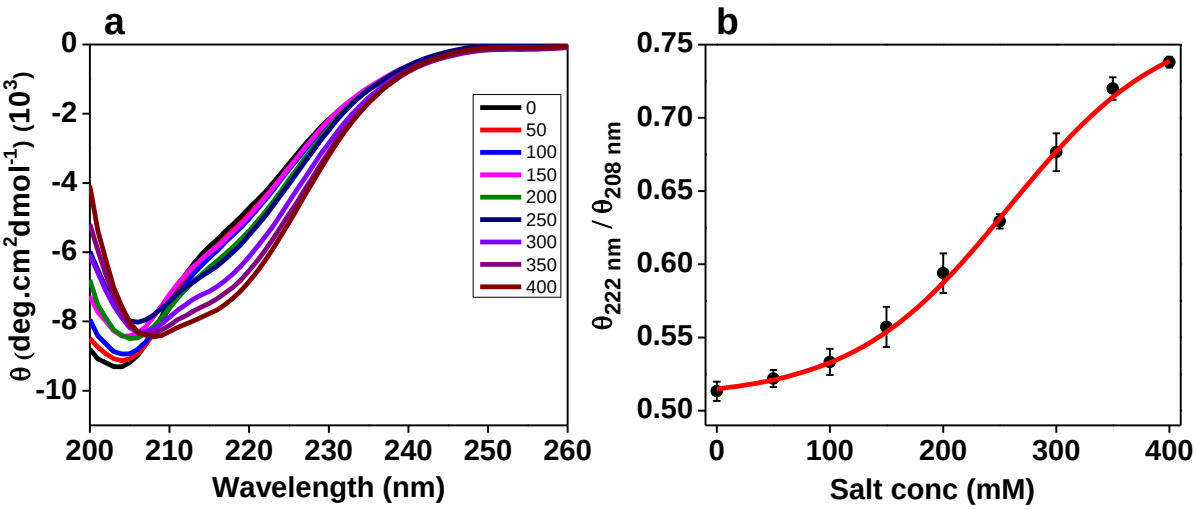

Figure 4.4 Salt-induced conformational changes in the acid-unfolded state of β_2m at pH 2.5 (*a*) Far-UV CD spectra of β_2m at different salt concentrations. (b) Ratiometric ellipticity plot at 222 nm to 208 nm as a function of increasing salt concentrations.

4.3.3 Salt-induced conformational transitions investigated using Trp fluorescence

Next, we probed the intrinsic fluorescence properties of single tryptophan (W60 & W95) mutants, in which Trp residue is located at different regions of the protein. First, we validated that the Trp mutation is not affecting the oligomers formation by comparing the DCVJ binding of wt with W60 and W95 proteins which suggest that mutants have similar propensity to form oligomers in presence of salt (Fig. 4.5).

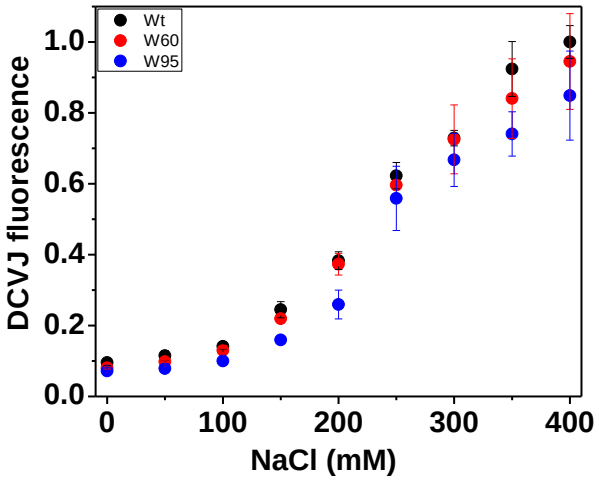

Figure 4.5 DCVJ fluorescence intensity at 500 nm wavelength of wild-type β_2m (black dots) and mutants (W60- red dots & W95- blue dots) as a function of increasing salt concentrations.

Tryptophan fluorescence is sensitive to the polarity of its immediate environment (35). In the acid-unfolded state of β_2m, W60 and W95 proteins have an emission maxima ~341 nm and ~346 nm respectively. As the salt concentration increases, W60 protein exhibits a significant blue shift in fluorescence emission maxima with a total shift of ~9 nm (Fig. 4.6 *a*,*b*). On the contrary, the region around W95 remains solvent exposed even at 400 mM salt concentration (Fig. 4.6 *c*,*d*). The blue shift in the fluorescence emission maxima of W60 signifies that the region around W60 residue gets buried during the oligomers formation, while the region around W95 remains solvent exposed.

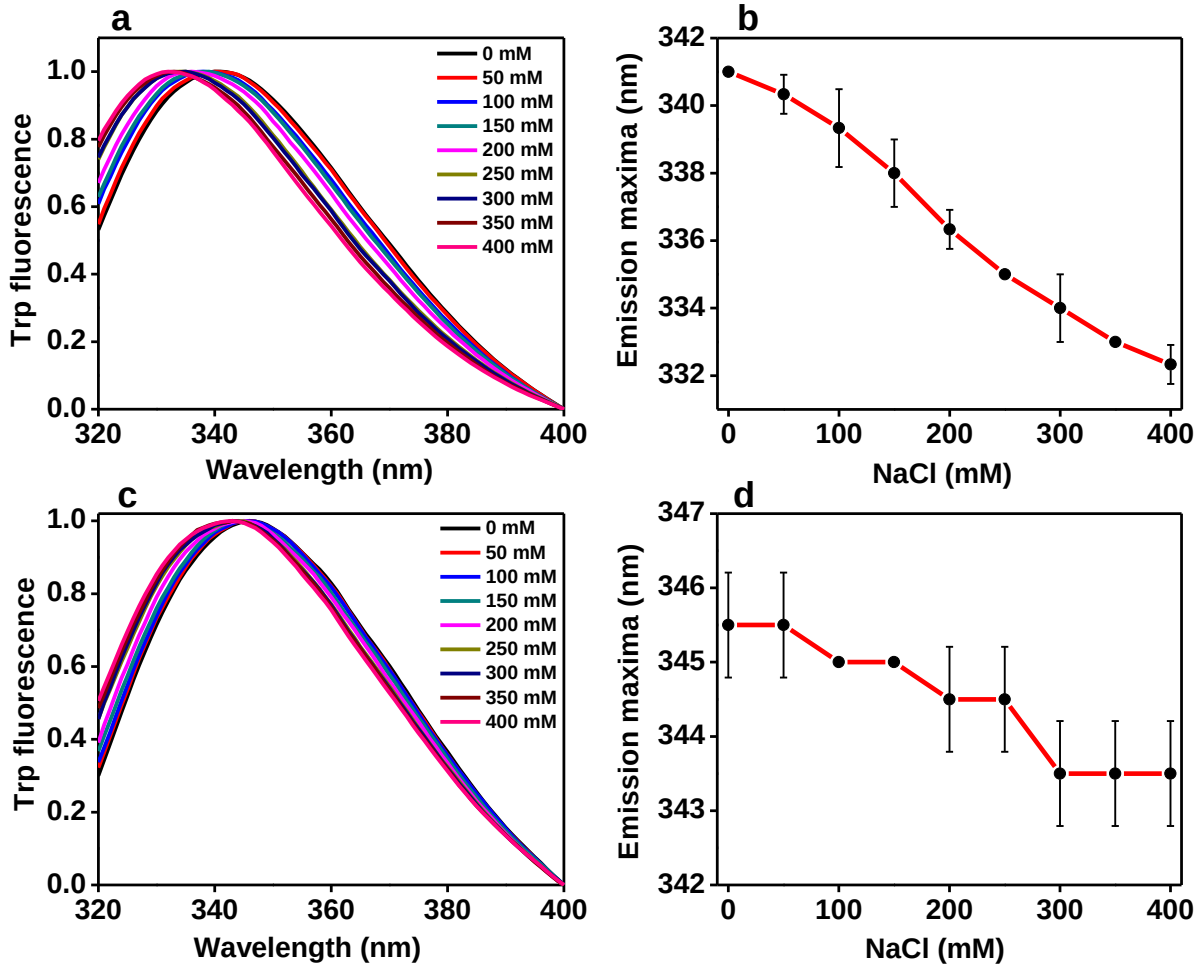

Figure 4.6 Trp fluorescence spectra and emission maxima of β_2m mutants at different salt concentrations. Fluorescence emission spectra of W60 (*a*) and W95 (*c*) proteins in the acid-unfolded (pH 2.5) state and in presence of different salt concentrations. Fluorescence emission maxima shift of W60 (b) & W95 (d) proteins as a function of varying salt concentrations.

4.3.4 Kinetics of salt-induced oligomer formation probed by DCVJ and ANS fluorescence

Our equilibrium data established that higher salt concentrations promote the oligomerization of acid-unfolded state. Interestingly, the increase in oligomer population corroborates well with the formation of hydrophobic patches and α-helical secondary structure. Next, we investigated the kinetics of oligomer formation from an acid-unfolded state at high salt concentration using DCVJ and ANS fluorescence. Upon rapid mixing of pH 2.5 protein solution with high salt concentration buffer, DCVJ fluorescence showed a burst phase (28%) that could not be resolved within the dead-time of mixing. The burst phase is followed by a bi-exponential increase in fluorescence intensity with rate constants of ~20 s^{-1} and ~1 s^{-1} (Fig. 4.7 *a* & Table 4.2). The presence of burst phase indicates the rapid formation of early oligomers in the sub-millisecond time. On the contrary, ANS fluorescence demonstrated a drop in fluorescence in the burst phase followed by bi-exponential increase in fluorescence with rate constants of ~19 s^{-1} and ~ 1 s^{-1} (Fig. 4.7 *b* & Table 4.2). The drop in ANS fluorescence in the burst phase suggests the loss of hydrophobic patches during the initial intermolecular associations between the polypeptide chains. The similar kinetics of the resolved phase of both ANS and DCVJ indicate that the formation of oligomers and hydrophobic patches take place simultaneously. Taken together, these results provide new insights into the kinetics of salt-induced oligomer formation from an acid-unfolded state.

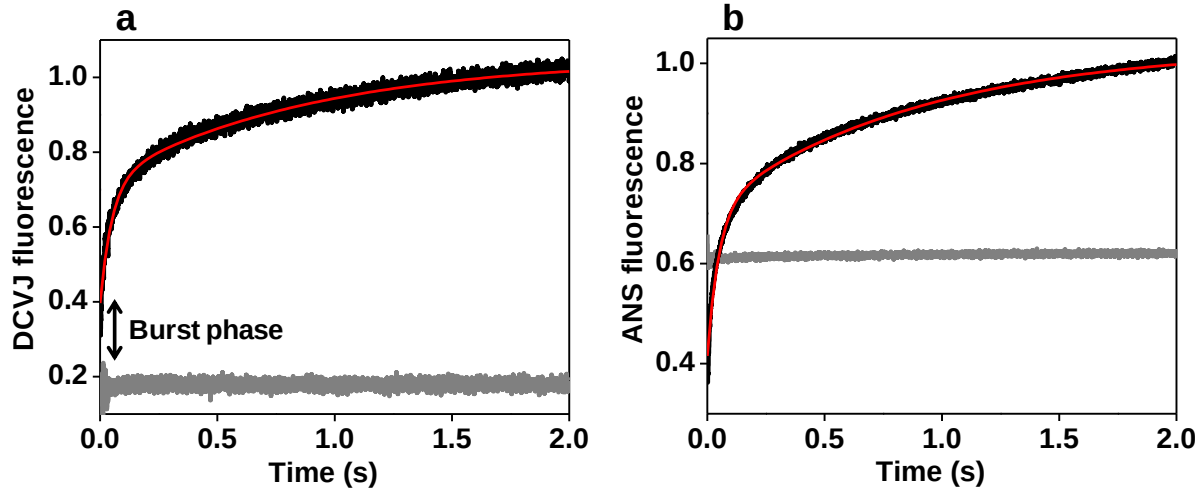

Figure 4.7 Salt-induced oligomer formation from an acid-unfolded state of β_2m monitored by DCVJ and ANS probes. Kinetic traces observed during oligomers formation monitored by DCVJ (*a*) and ANS (*b*) fluorescence intensity. Protein baseline was collected with pH 2.5 protein solution. In each panel, the black line represents the kinetic trace, the red line through the data is a fit to a bi-exponential equation and the grey line represents the protein baseline at pH 2.5.

Table 4.2 Recovered kinetic parameters from stopped-flow fluorescence experiments

Structural probes	Burst phase (%)	k_{fast} (s^{-1}) (Amplitude)	k_{slow} (s^{-1}) (Amplitude)
ANS fluorescence	*	19.2 ± 0.89 (0.47 ± 0.02)	1.1 ± 0.07 (0.53 ± 0.02)
DCVJ fluorescence	28 ± 4	19.8 ± 0.90 (0.48 ± 0.01)	1.1 ± 0.03 (0.52 ± 0.01)

***** Could not be estimated

4.4 Discussion

The ability of proteins and peptides to form amyloid fibrils is increasingly being recognized as a generic property of all polypeptides irrespective of their amino acid sequences (1). However, the basic amyloid fold is same for different proteins, a single polypeptide chain can give rise to amyloid fibrils with distinct supramolecular morphologies (36). For example amyloid fibrils of Amyloid-β (Aβ) peptide and α-synuclein protein show distinct morphologies in transmission electron microscopy (TEM) images (36). Since, majority of the amyloid fibrils are made up of multiple β-sheets, the differences in arrangements of these sheets could be the mere cause for amyloid polymorphism (37). However, many studies indicate that each polymorphic form has distinct packing of proteins in the cross-β structure that can propagate itself (38-40). Self-propagating, protein-level packing differences in amyloid fibrils could be the underlying mechanism for the occurrence of distinct prion strains in transmissible spongiform encephalopathies (41-43).

It has been shown that the physico-chemical factors such as pH, temperature, agitation and salt can modulate the final fibril morphologies (24, 27). Therefore, it is very important to understand how changes in fibril growth conditions lead to amyloid polymorphism which can provide valuable insights into the basis of the structural heterogeneity inherent in amyloids. In the present investigation, we have shown that high salt concentrations can strongly modulate the conformations of early oligomeric intermediates formed prior to the amyloid state.

Despite the increasing understanding of the mechanisms by which salts affect the amyloid formation, structural elucidation of early oligomers formed during salt-induced aggregation process has not been studied in great detail. In this work, we provided new structural insights into the mechanism of oligomer formation at high salt concentrations. Both DCVJ fluorescence and dynamic light scattering results indicate that at high salt concentrations, the acid-unfolded state of β_2m oligomerizes to form multimers. The formation of oligomers could be driven by charge screening that will minimize the charge repulsion, allowing protein molecules to come together, which, in turns, favors the hydrophobic interactions. Further, the increase in the amplitude of the long component of ANS fluorescence lifetime with an increase in salt concentration suggests the formation of new hydrophobic structures which are solvent protected. Far-UV CD measurements indicated that the ionic strength induces a change in the secondary structure of β_2m from a predominantly random coil to α-helical which could be a precursor to worm-like fibrils. Taken together,

these findings indicate that salt-induced oligomerization is accompanied by an increase in structural order which upholds with the CD and ANS data. Further, the region around W60 residue is buried whereas W95 residue remains exposed in the salt-induced α-helical rich oligomers. The blue shift in the emission maximum of W60 could be attributed to the change in Trp environment caused by the self-association of β_2m at high ionic strength. Further, kinetics of oligomer formation monitored by DCVJ and ANS fluorescence provide new insights into the early structural changes induced by salt. Interestingly, ANS kinetics data show a decrease in the ANS fluorescence in the burst phase which suggests the loss of hydrophobic patches during the initial phase of oligomerization. This could be due to inter-molecular associations between the polypeptide chains which disrupts the existing hydro-phobic patches. The observed kinetics of both DCVJ and ANS fluorescence are similar suggesting that both oligomer and hydrophobic structure formation take place simultaneously. In conclusion, these salt-induced oligomers are rich in hydrophobic patches and marginal increase in α-helical structure and could be the driving force for the formation of worm-like fibrils.

4.5 References

1. Knowles TP, Vendruscolo M, & Dobson CM (2014) The amyloid state and its association with protein misfolding diseases. *Nature Reviews Molecular Cell Biology* 15(6):384-396.
2. Dobson CM (2004) Principles of protein folding, misfolding and aggregation. (Translated from eng) *Semin Cell Dev Biol* 15(1):3-16 (in eng).
3. Sunde M, *et al.* (1997) Common core structure of amyloid fibrils by synchrotron X-ray diffraction. (Translated from eng) *J Mol Biol* 273(3):729-739 (in eng).
4. Sunde M & Blake C (1997) The structure of amyloid fibrils by electron microscopy and X-ray diffraction. *Advances in protein chemistry* 50:123.
5. Guijarro JI, Sunde M, Jones JA, Campbell ID, & Dobson CM (1998) Amyloid fibril formation by an SH3 domain. *Proceedings of the National Academy of Sciences* 95(8):4224-4228.
6. Chiti F, *et al.* (1999) Designing conditions for in vitro formation of amyloid protofilaments and fibrils. *Proceedings of the National Academy of Sciences* 96(7):3590-3594.
7. Fändrich M, Fletcher MA, & Dobson CM (2001) Amyloid fibrils from muscle myoglobin. *Nature* 410(6825):165-166.
8. Chiti F & Dobson CM (2009) Amyloid formation by globular proteins under native conditions. *Nature chemical biology* 5(1):15-22.
9. Fändrich M, *et al.* (2003) Myoglobin forms amyloid fibrils by association of unfolded polypeptide segments. *Proceedings of the National Academy of Sciences* 100(26):15463-15468.
10. Collinge J (2001) Prion diseases of humans and animals: their causes and molecular basis. *Annual review of neuroscience* 24(1):519-550.
11. Chien P, Weissman JS, & DePace AH (2004) Emerging principles of conformation-based prion inheritance. *Annual review of biochemistry* 73(1):617-656.
12. Paravastu AK, Leapman RD, Yau W-M, & Tycko R (2008) Molecular structural basis for polymorphism in Alzheimer's β-amyloid fibrils. *Proceedings of the National Academy of Sciences* 105(47):18349-18354.
13. Nekooki-Machida Y, *et al.* (2009) Distinct conformations of in vitro and in vivo amyloids of huntingtin-exon1 show different cytotoxicity. *Proceedings of the National Academy of Sciences* 106(24):9679-9684.

14. Serpell LC, Blake CC, & Fraser PE (2000) Molecular structure of a fibrillar Alzheimer's Aβ fragment. *Biochemistry* 39(43):13269-13275.
15. Goldsbury C, Frey P, Olivieri V, Aebi U, & Müller SA (2005) Multiple assembly pathways underlie amyloid-β fibril polymorphisms. *Journal of molecular biology* 352(2):282-298.
16. Apostol M, *et al.* (2007) Atomic structures of amyloid cross-beta spines reveal varied steric zippers. *Nature* 447(7143):453457Selkoe.
17. Kelly JW (1998) The alternative conformations of amyloidogenic proteins and their multi-step assembly pathways. *Current opinion in structural biology* 8(1):101-106.
18. Fraser PE, *et al.* (1997) Instability, unfolding and aggregation of human lysozyme variants underlying amyloid fibrillogenesis.
19. Uversky VN & Fink AL (2004) Conformational constraints for amyloid fibrillation: the importance of being unfolded. *Biochimica et Biophysica Acta (BBA)-Proteins and Proteomics* 1698(2):131-153.
20. Benilova I, Karran E, & De Strooper B (2012) The toxic A [beta] oligomer and Alzheimer's disease: an emperor in need of clothes. *Nature neuroscience* 15(3):349-357.
21. Glabe CG (2008) Structural classification of toxic amyloid oligomers. *Journal of Biological Chemistry* 283(44):29639-29643.
22. Drescher M, Huber M, & Subramaniam V (2012) Hunting the Chameleon: Structural Conformations of the Intrinsically Disordered Protein Alpha-Synuclein. *ChemBioChem* 13(6):761-768.
23. Jain S & Udgaonkar JB (2010) Salt-induced modulation of the pathway of amyloid fibril formation by the mouse prion protein. *Biochemistry* 49(35):7615-7624.
24. Gosal WS, *et al.* (2005) Competing pathways determine fibril morphology in the self-assembly of β 2-microglobulin into amyloid. *Journal of molecular biology* 351(4):850-864.
25. Chatani E, Yagi H, Naiki H, & Goto Y (2012) Polymorphism of β2-microglobulin amyloid fibrils manifested by ultrasonication-enhanced fibril formation in trifluoroethanol. *Journal of Biological Chemistry* 287(27):22827-22837.
26. Kumar S & Udgaonkar JB (2009) Structurally distinct amyloid protofibrils form on separate pathways of aggregation of a small protein. *Biochemistry* 48(27):6441-6449.

27. Tanaka M, Chien P, Naber N, Cooke R, & Weissman JS (2004) Conformational variations in an infectious protein determine prion strain differences. *Nature* 428(6980):323-328.
28. Platt GW, McParland VJ, Kalverda AP, Homans SW, & Radford SE (2005) Dynamics in the unfolded state of β 2-microglobulin studied by NMR. *Journal of molecular biology* 346(1):279-294.
29. Narang D, Sharma PK, & Mukhopadhyay S (2013) Dynamics and dimension of an amyloidogenic disordered state of human β2-microglobulin. *European Biophysics Journal* 42(10):767-776.
30. McParland VJ, *et al.* (2000) Partially unfolded states of β2-microglobulin and amyloid formation in vitro. *Biochemistry* 39(30):8735-8746.
31. Hong D-P, Gozu M, Hasegawa K, Naiki H, & Goto Y (2002) Conformation of β2-microglobulin amyloid fibrils analyzed by reduction of the disulfide bond. *Journal of Biological Chemistry* 277(24):21554-21560.
32. Lindgren M, Sörgjerd K, & Hammarström P (2005) Detection and characterization of aggregates, prefibrillar amyloidogenic oligomers, and protofibrils using fluorescence spectroscopy. *Biophysical journal* 88(6):4200-4212.
33. Semisotnov G, *et al.* (1991) Study of the "molten globule" intermediate state in protein folding by a hydrophobic fluorescent probe. *Biopolymers* 31(1):119-128.
34. Uversky VN, Winter S, & Löber G (1996) Use of fluorescence decay times of 8-ANS-protein complexes to study the conformational transitions in proteins which unfold through the molten globule state. *Biophysical chemistry* 60(3):79-88.
35. Lakowicz JR (2013) *Principles of fluorescence spectroscopy* (Springer Science & Business Media).
36. Tycko R (2014) Physical and structural basis for polymorphism in amyloid fibrils. *Protein science* 23(11):1528-1539.
37. Tycko R (2015) Amyloid Polymorphism: Structural Basis and Neurobiological Relevance. *Neuron* 86(3):632-645.
38. Bousset L, *et al.* (2013) Structural and functional characterization of two alpha-synuclein strains. *Nature communications* 4.
39. Frederick KK, *et al.* (2014) Distinct prion strains are defined by amyloid core structure and chaperone binding site dynamics. *Chemistry & biology* 21(2):295-305.
40. Gath J, *et al.* (2014) Unlike twins: an NMR comparison of two α-synuclein polymorphs featuring different toxicity.

41. Safar J, *et al.* (1998) Eight prion strains have PrPSc molecules with different conformations. *Nature medicine* 4(10):1157-1165.
42. Wickner RB, *et al.* (2010) Prion amyloid structure explains templating: how proteins can be genes. *FEMS yeast research* 10(8):980-991.
43. Toyama BH & Weissman JS (2011) Amyloid structure: conformational diversity and consequences. *Annual review of biochemistry* 80.

Structural differences between amyloid fibrils of yeast prion probed by tryptophan fluorescence

5.1 Introduction

Prions are self-propagating amyloids and an element of protein-based inheritance (1). A intriguing feature of prions and many other amyloid forming proteins is the ability of a polypeptide chain to adopt multiple conformations in the amyloid state with different physical and biological properties. Fibrils with distinct structures are faithfully transmitted and show varied biological phenotypes. These conformational variants of prions are called prion strains (2, 3). The first evidence for amyloid polymorphism came from the study of prion protein (PrP) in mice where the isolated PrP^{Sc} (Scrapie form) from different mice showed different protease-resistant cores (4, 5). Many amyloids associated neurodegenerative diseases also show amyloid polymorphism (6).

Yeast prions provide a good model system to study many properties of prions such as strain phenomenon and its inheritance. The propagation and inheritance of [*PSI*$^+$] prion in yeast is well-studied and is formed by the conversion of soluble functional Sup35p, a translation termination factor, into non-functional amyloid fibrils (7, 8). Sup35 protein consists of three structural domains: N-terminal domain (N, residues 1-123), middle domain (M, residues124-253) and C-terminal domain (C, residues 254-685). The N domain is Q/N rich (residues 1-40) and is responsible for both prion induction and maintenance (9, 10). The M domain is rich in positively charged residues (K/E) (11) and maintains the solubility of the non-prion form of Sup35 and is sufficient along with the N domain (SupNM domain) for prion-based inheritance. The C domain is essential and sufficient for translation termination (10, 12).

In vitro, Sup35NM aggregate at different temperatures (4 and 37 °C) to form amyloid fibrils with distinct molecular structures (13). The amyloid core of 4 °C fibrils is shorter and thermodynamically less stable as compared to fibrils formed at 37 °C (14, 15). Interestingly, when introduced into yeast cells, 4 °C fibrils (Sc4) show strong [*PSI*$^+$] phenotype, whereas 37 °C fibrils (Sc37) show weak [*PSI*$^+$] phenotype (13, 15). The Sc represents the *Saccharomyces cerevisiae*. The Sc4 amyloid is physically less stable and hence is efficiently broken by chaperone machinery providing new seeds for converting the soluble pool of Sup35. Whereas, Sc37 conformation is structurally strong and are less efficiently broken that decreases the number of free ends for the further polymerization of soluble Sup35 making it weak [*PSI*$^+$] phenotype (16). Hsp104 and other chaperones such as Hsp70 and Hsp40 play an important role in the propagation and inheritance of the [*PSI*$^+$] (17, 18). The deletion and overexpression of the Hsp104 lead to the curing of [*PSI*$^+$] prion. However,

the mechanism of curing by Hsp104 is different for both deletion and overexpression. All the yeast prions requires Hsp104 for their propagation (19).

Based on different methodologies, two distinct models of Sup35NM fibrils were proposed. One model which is suggested is parallel in-register β-sheets. According to this model, the identical residues of different molecules are aligned and stacked on top of each other. This model was proposed based on various studies such as scrambling of the amino acid sequence of Sup35, mass per unit length measurements and solid state NMR studies and X-ray diffraction of 8 to 10 Å which is predicted only by the parallel in-register β-sheets (20-24). Whereas, the other model proposed is β-helix architecture (25). According to this model, only the head (top) and tail (bottom) regions of the adjacent molecules form the intermolecular contacts and the central core region contains intramolecular contacts (26). This model was proposed based on fluorescence studies using pyrene and acrylodan fluorescence. Since, pyrene and acrylodan with linker are large dyes as compared to the packing of β-strands in the β-sheets, there can be a possibility that these dyes might be precluded by the structure of the amyloid and provide less accurate results.

In this work, we studied the structural differences in two strains of Sup35 prion. Since Sup35NM is devoid of tryptophan residue, we introduced single Trp residue at 19 different positions in the polypeptide chain. Out of these residues, 15 residues were previously mutated to cysteine and labelled with pyrene for fluorescence experiments. Our studies using various single Trp mutants suggest that two different conformations of Sup35NM amyloid have different side-chain packing arrangement in the fibrillar state and can have implication in the propagation of the fibrils.

5.2 Experimental section

5.2.1 Materials

Guanidine Hydrochloride (GdmCl), Tris(hydroxymethyl) aminomethane (Tris), Sodium Chloride, Sodium phosphate monobasic dihydrate, Sodium phosphate dibasic dihydrate, Sodium Dodecyl Sulphate (SDS), Ethylenediaminetetraacetic acid (EDTA) and urea were purchased from Sigma (St. Louis, MO) and used without any additional purification. Isopropyl-β-thiogalactopyranoside (IPTG) and antibiotics (Ampicillin, Tetracycline, and Chloramphenicol) were obtained from Gold Biocom (USA). NiNTA resin and Q-Sepharose were procured from GE Healthcare Life Sciences (USA).

5.2.2 Cloning and site directed mutagenesis

A DNA fragment encoding Sup35NM was amplified from yeast genomic DNA using appropriate primers and cloned into the pET 23a expression vector (Table 5.1). Single Trp residue was introduced at different positions using overlap extension PCR. The primer sequences for various mutations are given in Table 5.1.

5.2.3 Protein expression and purification

The protein was overexpressed in BL21 (DE3)/pLysS cells using 0.4 mM concentration of IPTG. Cells suspended in lysis buffer (10 mM Tris.Cl, 1 mM EDTA, pH 8.0) were incubated in boiling water for 10 minutes. The boiled lysate was centrifuged at 11,500 rpm for 30 minutes to remove the cell debris. The supernatant was precipitated using equal volume of saturated solution of ammonium sulphate. The pellet formed was dissolved in a buffer containing 8 M GdmCl, 20 mM phosphate buffer, pH 8.0 and kept at 4 °C overnight. Next day, lysate was centrifuged to remove any insoluble particles and supernatant was used for NiNTA purification. After NiNTA purification, protein was further purified on the Q-sepharose column. The purified protein was concentrated and precipitated using methanol. The protein pellet was resuspended in 70% methanol and kept at -80 °C.

5.2.4 Fibrillation assay

Spontaneous fibril formation was performed by 100 times dilution of protein stock in aggregation buffer (5 mM phosphate, 150 NaCl, pH7.4) and by slow (10 rpm) overhead rotation for 24 hours. Aggregation buffer was pre-equilibrated at 4 °C and 37 °C for fibril formation and final protein concentration was 5 µM. After the fibrils formation, they are

passed through 50 kDa to remove any monomer and supernatant is used for the experiments. For thioflavin-T (ThT) binding studies, 2.5 μM of protein concentration was used and kept at 100 rpm for stirring.

5.2.5 Steady-state fluorescence measurements

Steady-state fluorescence measurements were performed on FluoroMax-4 (Horiba Jobin Yvon NJ). For Trp fluorescence spectra, excitation wavelength was set at 295 nm, excitation and emission slit widths were 0.8 nm and 4 nm, respectively. All the spectra were buffer subtracted to remove any contribution due to the solvent Raman scattering. Trp fluorescence anisotropy measurements were performed by setting λ_{ex} at 295 nm (bandpass 1.5 nm) and λ_{em} to 345 nm (bandpass 10 nm). An integration time of 0.5 sec was used to obtain a satisfactory signal-to-noise ratio. The steady-state fluorescence anisotropy was estimated using parallel ($I_{\parallel}$) and perpendicular ($I_{\perp}$) intensities and the G- factor as follows (27):

$$r = (I_{\parallel} - I_{\perp}G) / (I_{\parallel} + 2I_{\perp}G) \quad (5.1)$$

All measurements were carried out at 24±1 ^{o}C.

5.2.6 Time-resolved fluorescence measurements

Time-resolved fluorescence decay experiments were carried out using picosecond rhodamine 6G dye laser (Spectra Physics, Mountain View, CA) coupled to a time-correlated single-photon counting (TCSPC) setup. A mode-locked frequency doubled Nd:YAG laser (Millenia X, Spectra Physics) was used to pump a dye laser and the generated laser pulses were frequency doubled to 295 nm by using a KDP crystal. The instrument response function (IRF) at 295 nm was collected using a colloidal suspension of dried non-dairy coffee whitener and the width (full width at half maximum) of the IRF was ~ 60 ps. The emission of Trp fluorescence was collected using a microchannel plate photomultiplier (2809u, Hamamatsu, Hamamatsu City, Japan). For time-resolved fluorescence intensity decay and anisotropy decay measurements, emission monochromator was fixed at 345 nm. The time-resolved fluorescence intensity decay was collected at magic angle (54.7°) with respect to the excitation polarizer and the peak count was ~20,000. For time-resolved fluorescence depolarization kinetics, emission was collected at 0° (parallel) and 90° (perpendicular) with respect to the excitation polarizer set at 0° (parallel). The perpendicular component of fluorescence intensity was always corrected for G-factor. A biexponential decay model was

used to analyze the anisotropy decays which give fast and slow rotational correlation times as follows (28):

$$r(t) = r_0 [\beta_{fast} \exp(-t/\phi_{fast}) + \beta_{slow} \exp(-t/\phi_{slow})] \quad (5.2)$$

where r_0 is the intrinsic fluorescence anisotropy, ϕ_{fast} and ϕ_{slow} are the short and long rotational correlation time and the β_{fast} and β_{slow} are the amplitudes associated with the short and long correlation time.

Table 5.1: Sup35NM Primers

aa-> W	Forward Primer 5' -3'	Reverse Primer 5' -3'
wt	TACATATGTCGGATTCAAACCAAGGC	GACTCGAGATCGTTAACAACTTCGTCATCC
S2W	GGAGATATACATATGTGGGATTCAAACCAAGGC	GCCTTGGTTTGAATCCCACATATGTATATCTCC
G7W	CGGATTCAAACCAATGGAACAATCAGCAAAAC	GTTTTGCTGATTGTTCCATTGGTTTGAATCCG
G21W	CAATACAGCCAGAACGGTTGGCAACAACAAGGTAACAAC	GTTGTTACCTTGTTGTTGCCAACCGTTCTGGCTGTATTG
G25W	CGGTAACCAACAACAATGGAACAACAGATACCAAGG	CCTTGGTATCTGTTGTTCCATTGTTGTTGGTTACCG
G31W	GGTAACAACAGATACCAATGGTATCAAGCTTACAATGCTC	GAGCATTGTAAGCTTGATACCATTGGTATCTGTTGTTACC
G51W	GGTACTACCAAAATTACCAATGGTATTCTGGGTACCAACAAGG	CCTTGTTGGTACCCAGAATACCATTGGTAATTTTGGTAGTACC
G58W	CTGGGTACCAACAATGGGGCTATCAACAGTAC	GTACTGTTGATAGCCCCATTGTTGGTACCCAG
G68W	CAGTACAATCCCGACGCCTGGTACCAGCAACAGTATAATC	GATTATACTGTTGCTGGTACCAGGCGTCGGGATTGTACTG
G77W	GCAACAGTATAATCCTCAATGGGGCTATCAACAGTACAATCC	GGATTGTACTGTTGATAGCCCCATTGAGGATTATACTGTTGC
G86W	CAACAGTACAATCCTCAATGGGGTTATCAGCAGCAATTC	GAATTGCTGCTGATAACCCCATTGAGGATTGTACTGTTG
G96W	GCAATTCAATCCACAATGGGGCCGTGGAAATTAC	GTAATTTCCACGGCCCCATTGTGGATTGAATTGC
F104W	CCGTGGAAATTACAAAAACTGGAACTACAATAACAATTTGC	GCAAATTGTTATTGTAGTTCCAGTTTTTGTAATTTCCACGG
F117W	GGATATCAAGCTGGTTGGCAACCACAGTCTCAAG	CTTGAGACTGTGGTTGCCAACCAGCTTGATATCC
S121W	CTGGTTTCCAACCACAGTGGCAAGGTATGTCTTTGAAC	GTTCAAAGACATACCTTGCCACTGTGGTTGGAAACCAG
G129W	GTATGTCTTTGAACGACTGGCAAAAGCAACAAAAGCAG	CTGCTTTTGTTGCTTTTGCCAGTCGTTCAAAGACATAC
A137W	GCAACAAAAGCAGGCCTGGCCCAAACCAAAGAAGAC	GTCTTCTTTGGTTTGGGCCAGGCCTGCTTTTGTTGC
K184W	GAAACCAAAGAACCAACTTGGGAGCCAACAAAGGTCGAAG	CTTCGACCTTTGTTGGCTCCCAAGTTGGTTCTTTGGTTTC
S221W	GTAGAAGACCTTAAAATCTGGGAATCAACACATAATACC	GGTATTATGTGTTGATTCCCAGATTTTAAGGTCTTCTAC
V250W	-----	GCCTCGAGATCGTTAACCCATTCGTCATCCACTTCTT

5.3 Results

5.3.1 Site-specific structural insights using steady-state fluorescence

In order to monitor the structural differences in the polypeptide chain at the residue-level, we took advantage of the fact that Sup35NM lacks tryptophan (Trp) residue. We created 19 single Trp mutants distributed over the entire polypeptide chain (Fig. 5.1). For incorporating Trp, the residue position at 2, 7, 21, 25, 31, 51, 58, 68, 77, 86, 96, 121, 137, 184, 250 were chosen. These residues were previously mutated to cysteine and showed that mutations of these residues do not affect the prion propagation in yeast (14). Further, they labeled the cysteines with pyrene and acrylodan and showed that the presence of large dye molecule is also not affecting the kinetics of the fibrillation. Additionally, we created four more single Trp mutants at position (104, 117, 129 and 129) and out of four, 117 is previously used for the studies (29).

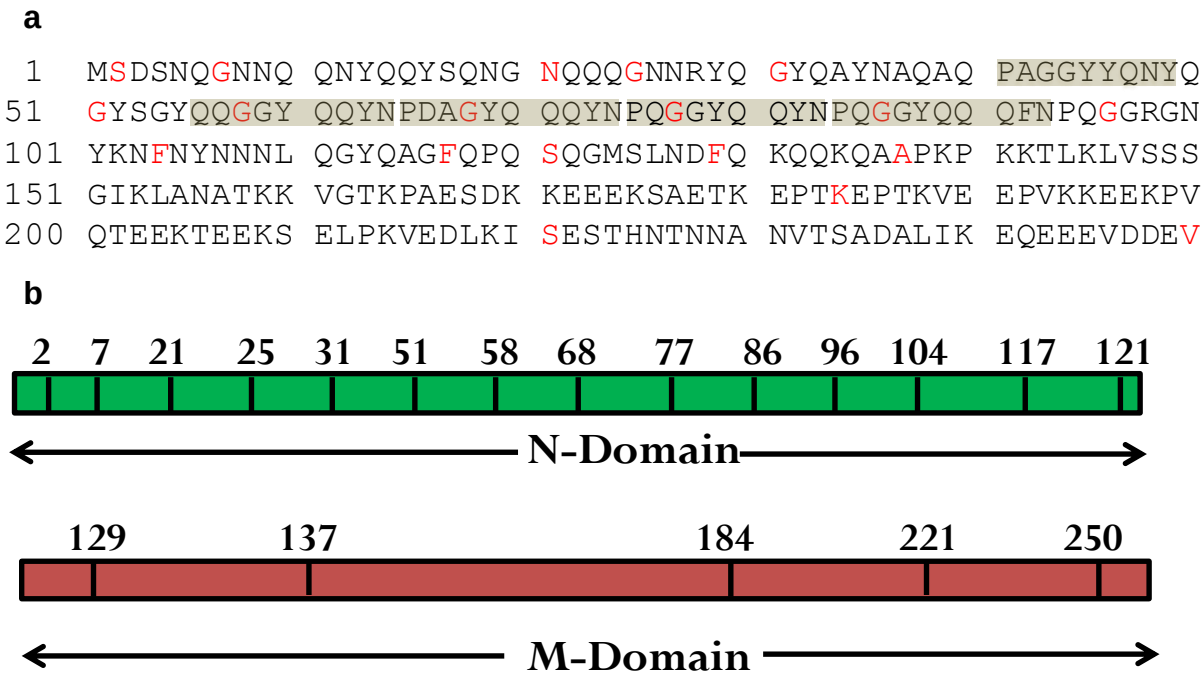

Figure 5.1 Protein sequence of Sup35NM and mutation sites. (a) The amino acid sequence showing residues mutated to tryptophan in red and the five imperfect oligopeptide repeats shaded in grey. (b) Various positions of the residues in the N and M domain mutated to Trp and indicated by black line.

First, we carried out thioflavin T binding assay of wt and 19 single Trp mutants to establish that all the mutants retain similar aggregation capability (Fig. 5.2).

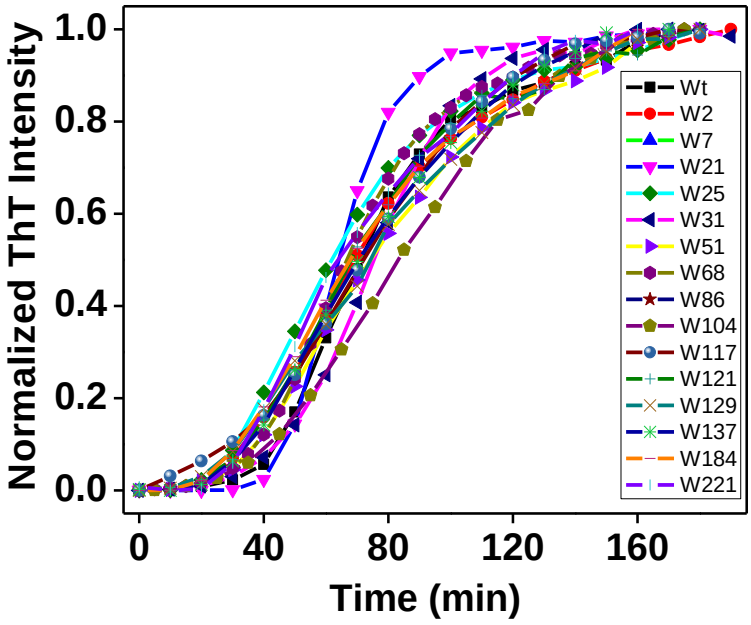

Figure 5.2 ThT fluorescence kinetics of wt and the mutants of Sup35NM during protein aggregation.

After demonstrating that the mutations do not affect the fibril kinetics, we monitored the changes in Trp fluorescence readouts to obtain region-specific structural information of protein molecules in the amyloid state of two different conformations. In the denatured state, Trp fluorescence emission spectra of all the mutants showed peak ~345 nm suggesting the solvent-exposed nature of the residues (Fig. 5.3).

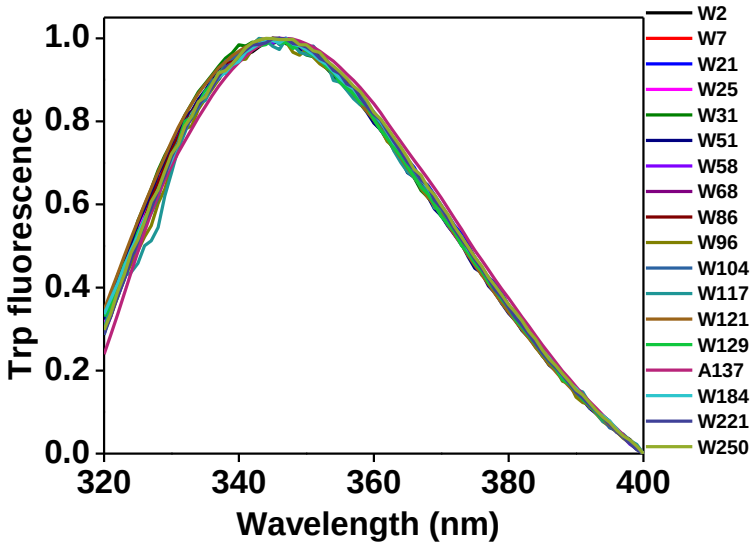

Figure 5.3 Normalized Trp fluorescence spectra of various mutants of Sup35NM in 8M urea.

Upon conversion into amyloid fibrils at 4 °C and 37 °C temperature, different locations of the polypeptide chain showed a varied extent of blue shift in emission maxima (Fig. 5.4 *a*,*b*). The residue positions at 21, 25 and 31 showed the largest blue shift in Trp fluorescence spectra in both Sc4 and Sc37 conformations indicating that they are well protected from the solvent and is consistent with the previous studies (Fig. 5.4 *c*). Whereas, other residues in the N domain and M domain (129, 137) remains partially exposed to the solvent. The residue positions at 184, 221 and 250 in M domain had no significant blue shift, indicating that these residues remained solvent exposed in the amyloid state (Fig. 5.4 *c*).

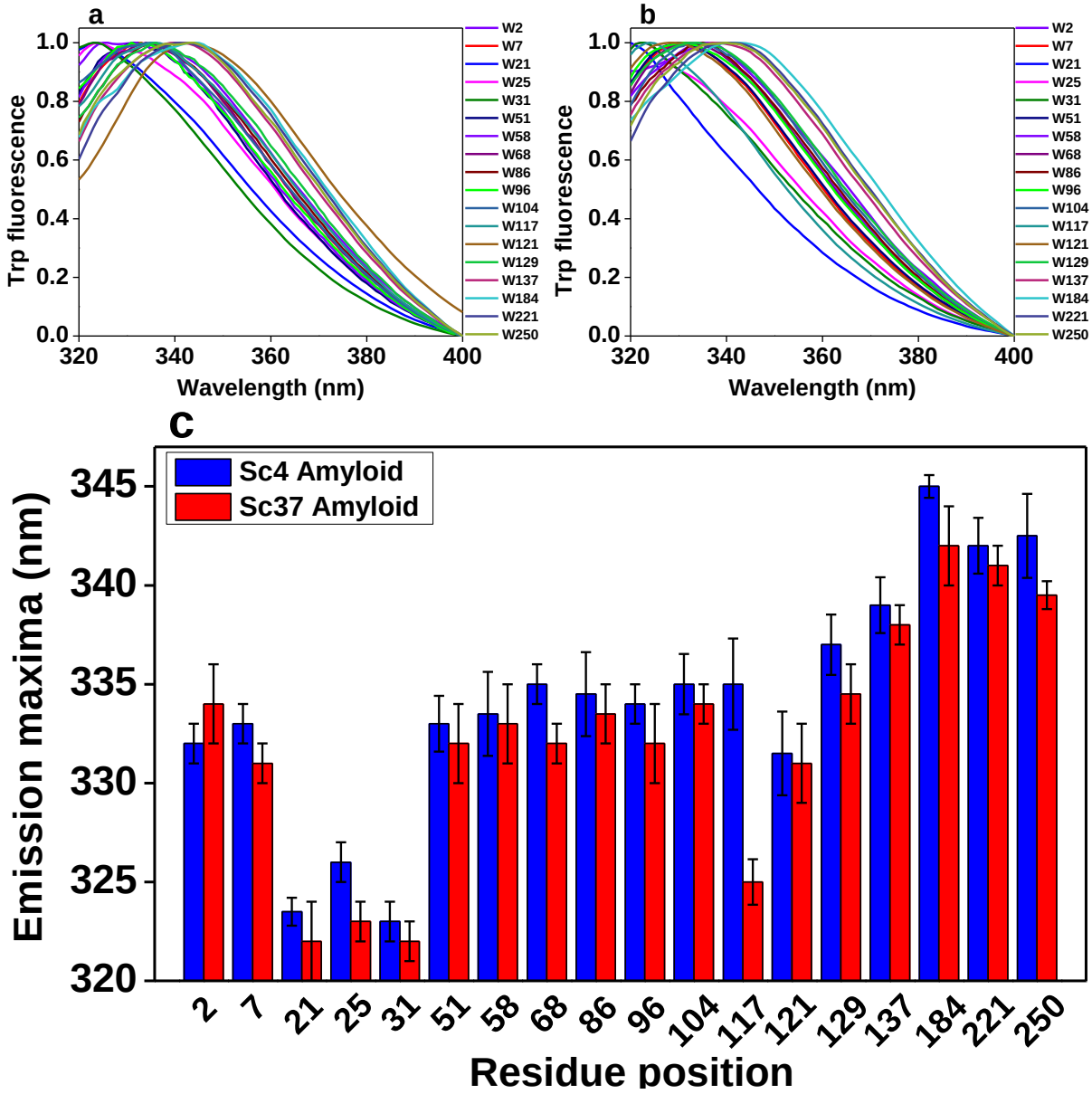

Figure 5.4 Distinct features of two distinct amyloid states (Sc4 and Sc37) of Sup35NM monitored by Trp fluorescence. Normalized Trp fluorescence spectra of various mutants in the Sc4 (a) and Sc37 amyloid conformations. (c) Variations in emission maxima along the mutated residues in two different amyloid conformations.

Next, we carried out steady-state fluorescence anisotropy which reports the structural dynamics at a given residue position. In the amyloid state, different residue positions of the polypeptide chain showed a varied extent of anisotropy in both conformation-independent and conformation-dependent manners (Fig. 5.5). The dampening in dynamics can be due to the structure formation around the residue location which causes rotational restrictions for the tryptophan. Based on the anisotropy measurements, residue positions from 2 to 31 showed high anisotropy whereas adjacent residues 51-86 showed low anisotropy indicating an increase in conformational flexibility compared to earlier residues. The residues from 96 to 117 again showed high anisotropy, whereas, adjacent residues from 121 to 137 showed low anisotropy (Fig. 5.5). The residue positions at 184, 221 and 250 in M domain had low anisotropy indicating that these residues are more unstructured as compared to other residues in the M domain. All these measurements indicated that residues in the central region from 51 to 86 are partially exposed and dynamic as compared to other residues in the N domain. Whereas, residues in the M domain are more structured in the Sc37 conformation compared to Sc4 (Fig. 5.5). Further, there are significant and measurable differences in anisotropy at residues positions 25, 31, 96 and 117 of two amyloid conformations indicating a presence of distinct local structures around these residues.

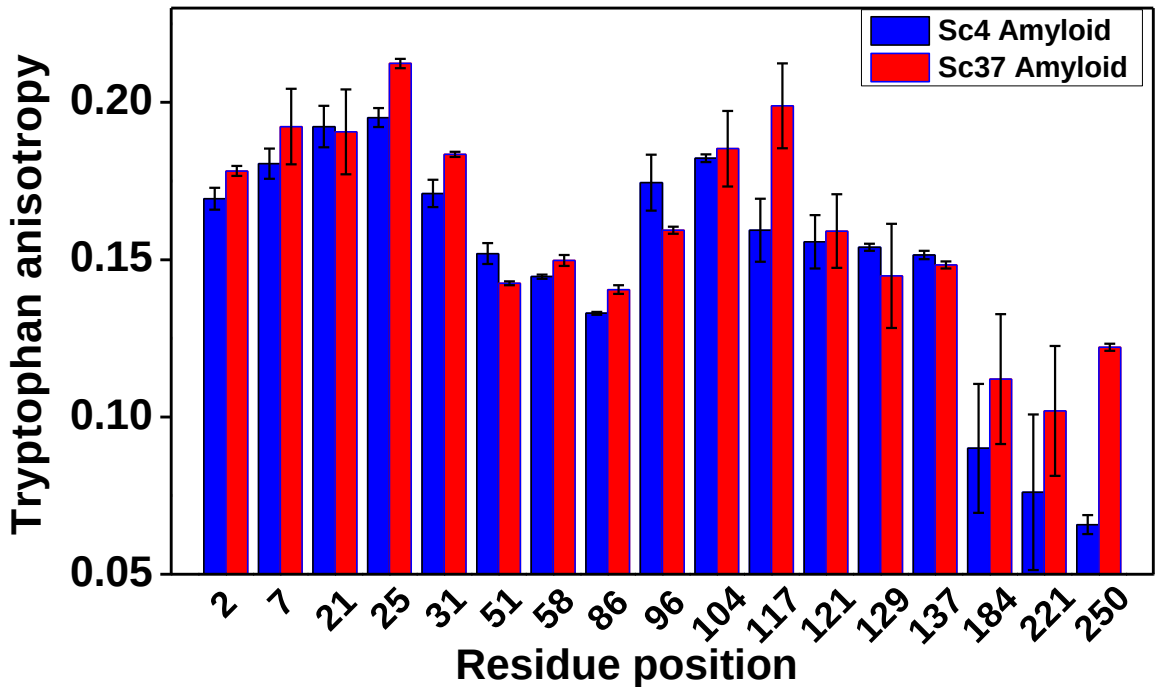

Figure 5.5 Steady-state Trp anisotropy of different mutants in two distinct amyloid states (Sc4 and Sc37) of Sup35NM.

5.3.2 Site-specific structural information using time-resolved fluorescence

In order to gain more structural insights into the amyloid conformations of Sup35, we have carried out picosecond-resolved fluorescence measurements. The fluorescence lifetime is an intrinsic property of the probe and depends upon the non-radiative decay rate. The two common quenchers of Trp fluorescence are water and side chains of an amino acid such as glutamine, asparagines, lysine and tyrosine (30). Tryptophan fluorescence from various residue positions in two different conformations demonstrated triexponential lifetime (Fig. 5.6). The residue positions from 2 to 31 showed shorter mean lifetime as compared to residues from 51 to 86. Since the residues from 2 to 31 are more buried and well protected from the solvent, they should have been expected to have longer mean lifetime (Fig. 5.6). However, the presence of Q/N residues in a stretch of sequence from residue 6 to 41 can be a key factor which can quench the Trp fluorescence. The residues adjacent to the central core from 96 to 121 again demonstrated shorter mean lifetime. The residues in the M domain have comparable lifetime except 221 which has a longer lifetime (Fig. 5.6). The residue positions 7, 21, 25, 31 104, 117 showed significant differences in the Trp lifetime of two distinct amyloid conformations.

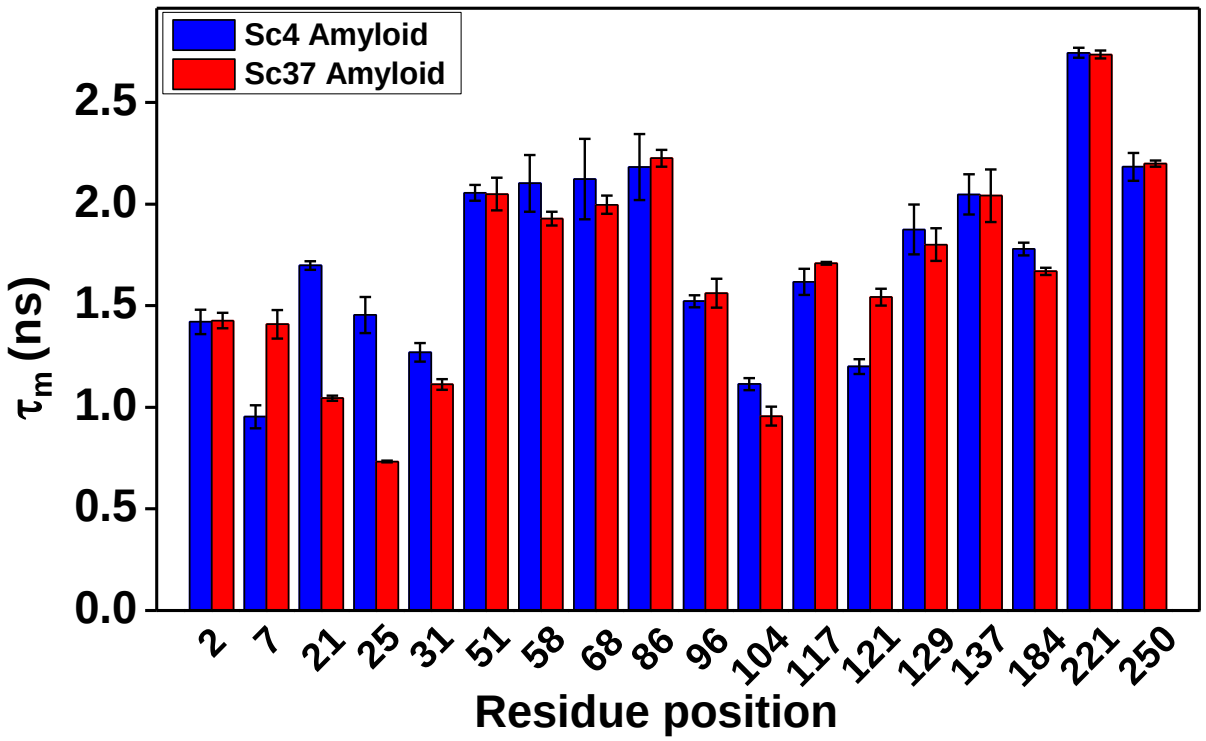

Figure 5.6 Mean fluorescence lifetime of Trp of different mutants in two different amyloid states (Sc4 and Sc37) of Sup35NM.

Next, we carried out time-resolved anisotropy decay measurements to obtain site-specific conformational flexibility in amyloid fibrils. The decay kinetics of various residue positions can be fitted to derive two rotational correlation times: a fast component (ϕ_{fast}) corresponds to the local motion of the fluorophore while the slow component (ϕ_{slow}) represents the global tumbling of the macromolecule. The time-resolved fluorescence depolarization kinetics of Trp mutants in the two amyloid conformations do not decay to zero because of large size of the fibrils (Fig. 5.7 *a-cc*). Therefore, the estimation of slow rotational correlation time (ϕ_{slow}) will be erroneous. The time scale (ϕ_{fast}) and the amplitude (β_{fast}) of fast rotational correlation time would give an idea about the site-specific local dynamics in two distinct amyloid conformations. The fast rotational correlation times for various positions in the amyloid state show no significant differences in both conformation-independent and conformation-dependent manners. Further, the amplitude of the fast rotational correlation time for the N domain residues is lower as compared to the M-domain residues which again suggest that N domain is more structured as compared to the M-domain (Fig. 5.7 *cc*). The amplitude of φ_{fast} for the residue positions 7, 21 25 (head region) and 104, 117 and 121 (tail region) in the N domain is lower for the Sc37 conformation as compared to the Sc4 suggesting higher extent of dampening of dynamics in the Sc37 conformation as a result of more ordered structure (Fig. 5.7 *cc*). The residue positions in the M domain show higher amplitude but the extent of increase is more for Sc4 conformation as compared to Sc37 conformation suggesting that M domain is more structured in the Sc37 conformation (Fig. 5.7 *cc*).

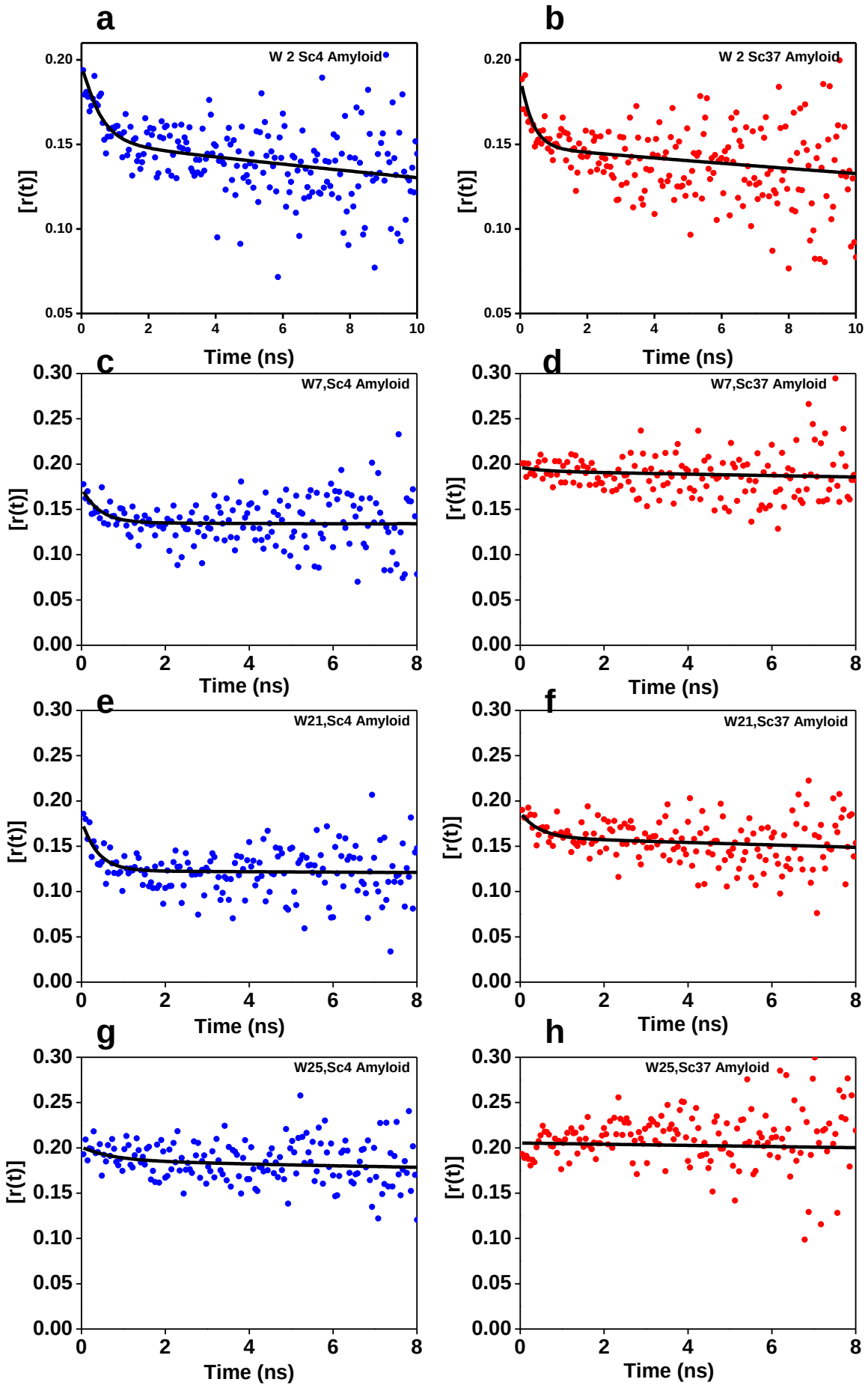
a
W 2 Sc4 Amyloid
b
W 2 Sc37 Amyloid
c
W7,Sc4 Amyloid
d
W7,Sc37 Amyloid
e
W21,Sc4 Amyloid
f
W21,Sc37 Amyloid
g
W25,Sc4 Amyloid
h
W25,Sc37 Amyloid
[r(t)]
Time (ns)

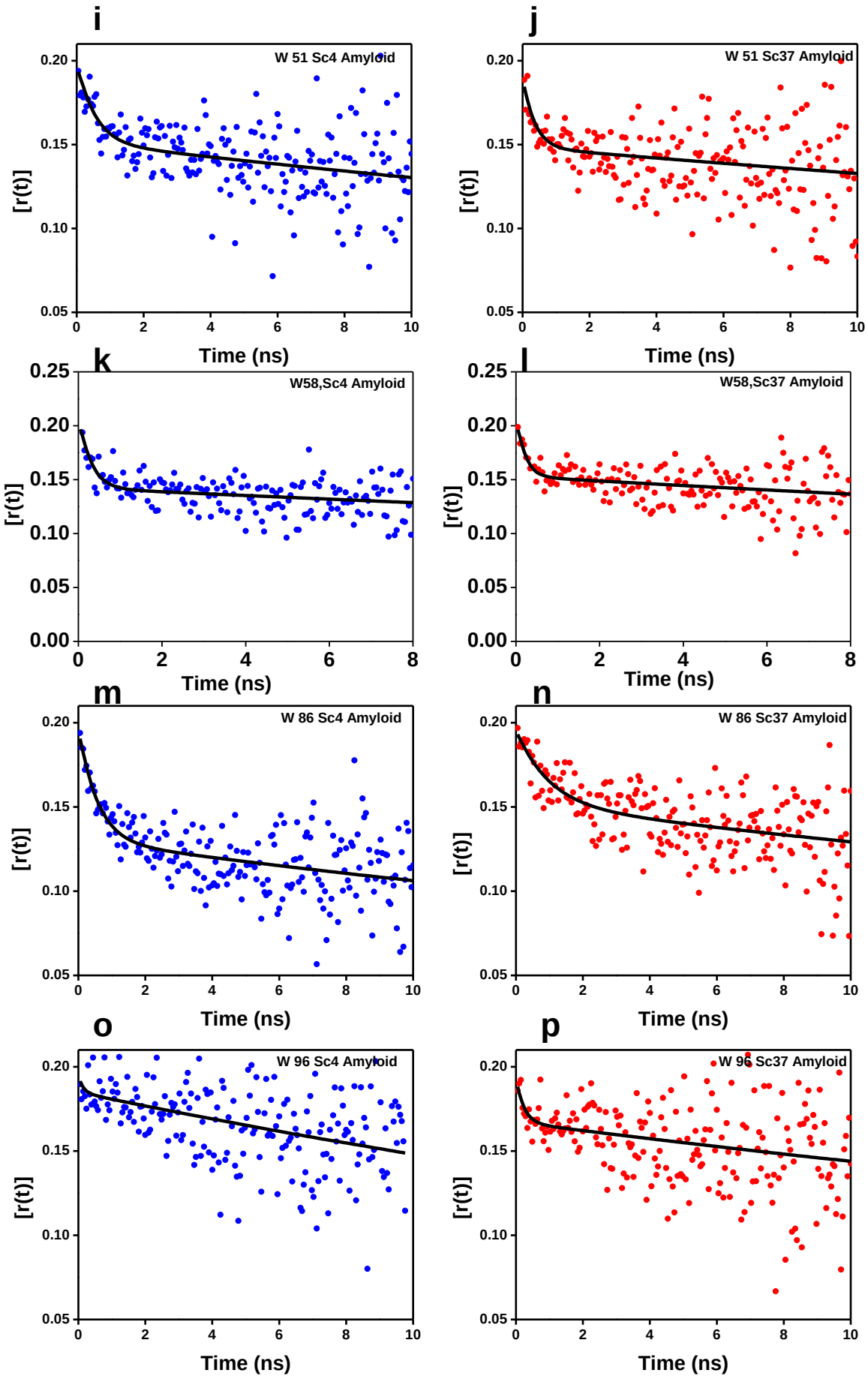
i
W 51 Sc4 Amyloid
[r(t)]
Time (ns)
j
W 51 Sc37 Amyloid
[r(t)]
Time (ns)
k
W58,Sc4 Amyloid
[r(t)]
Time (ns)
l
W58,Sc37 Amyloid
[r(t)]
Time (ns)
m
W 86 Sc4 Amyloid
[r(t)]
Time (ns)
n
W 86 Sc37 Amyloid
[r(t)]
Time (ns)
o
W 96 Sc4 Amyloid
[r(t)]
Time (ns)
p
W 96 Sc37 Amyloid
[r(t)]
Time (ns)

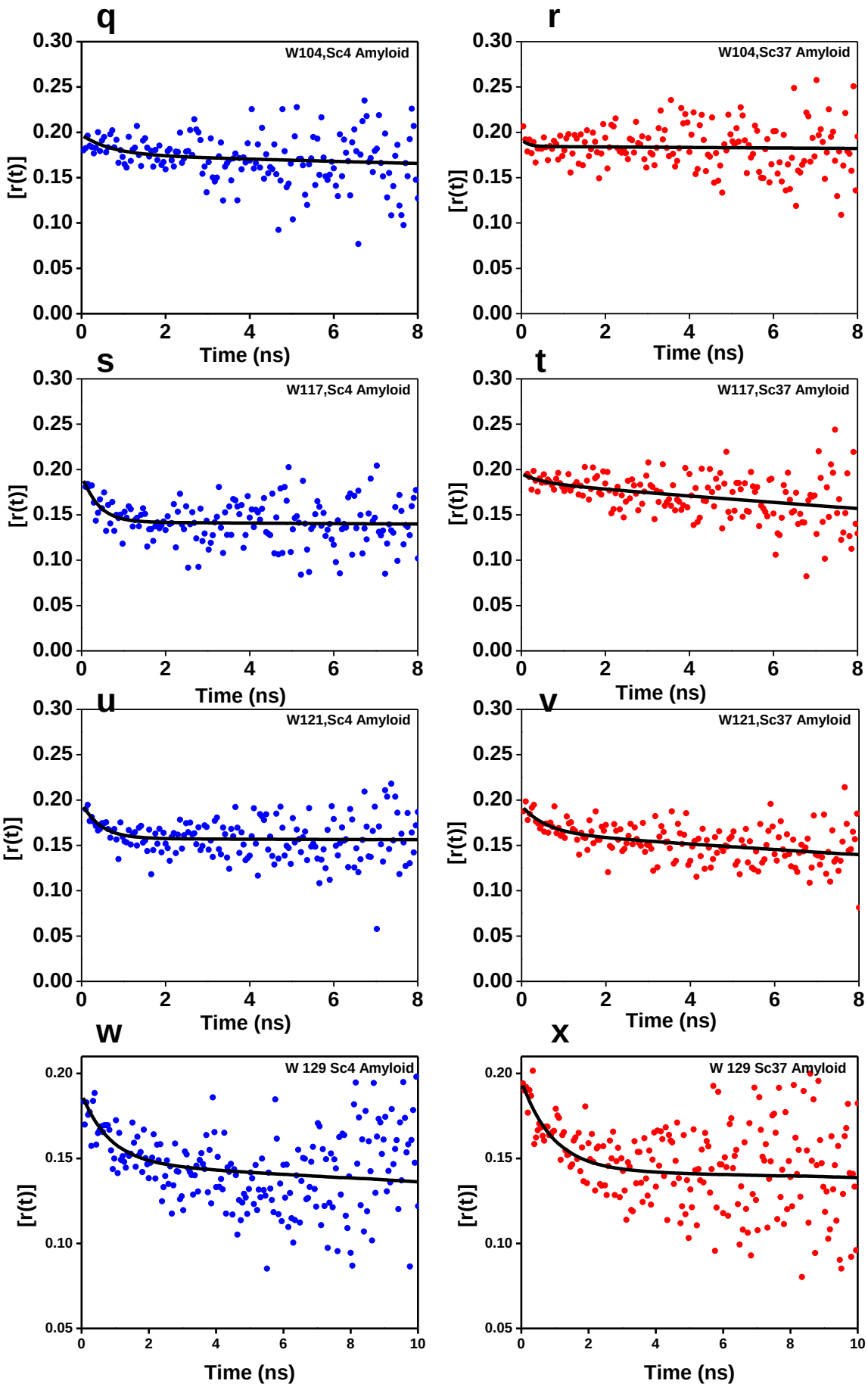
q
W104,Sc4 Amyloid
r
W104,Sc37 Amyloid
s
W117,Sc4 Amyloid
t
W117,Sc37 Amyloid
u
W121,Sc4 Amyloid
v
W121,Sc37 Amyloid
w
W 129 Sc4 Amyloid
x
W 129 Sc37 Amyloid
[r(t)]
Time (ns)

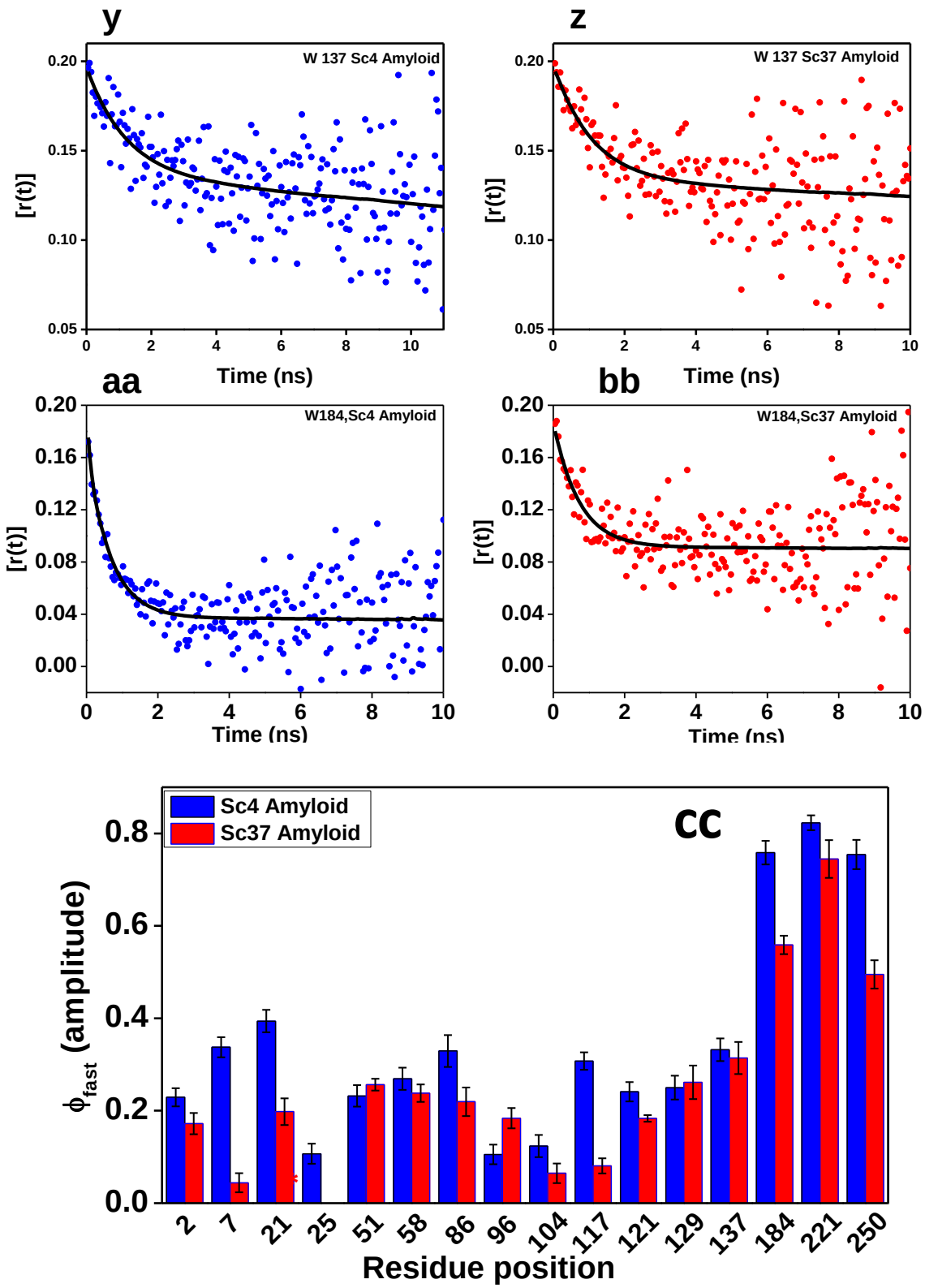

Figure 5.7 (a-t) Time-resolved fluorescence anisotropy decay of Trp of different mutants in two different amyloid states (Sc4 and Sc37) of Sup35NM. (u) Variations in the amplitude of fast rotation correlation time of anisotropy decay. * No local dynamics observed for this position. In all the fluorescence anisotropy decay profiles, the scatter points represent the observed decay and the black solid line represents the fit to the data (eq. 5.2).

5.4 Discussion

Yeast prions represent a protein-based non-mendelian mechanism for the inheritance of biological phenotypes (31). The strong and weak prion strains of Sup35 demonstrate different heritable phenotypes and are based on the distinct amyloid conformations of the same protein. The inheritance of both the strains is influenced by the action of cellular chaperone machinery particularly Hsp104. Despite intense studies to decipher the cause of different prion variants, the detailed structure of a prion variant has not yet been obtained. Using single Trp mutants created along the sequence of Sup35NM, we have been able to gain strain-specific structural and dynamical insights at specific locations of the protein in the amyloid state. The selective insight from each of these residues indicates that the intimidate environment around these residues are different in two distinct amyloid conformations. Further, the residues in the M domain which do not participate in the amyloid core and play an important role in Hsp104 interactions are found to have distinct structures with different dynamic properties.

Previous studies had established that the amyloid core of Sup35 fibrils is formed by the N domain and is shorter for the Sc4 compared to that of Sc37 conformations. The fibrils formed at 4 °C are structurally weak and show strong [PSI^{+}] phenotype, whereas, structurally strong fibrils formed at 37 °C confer weak phenotype(15). Using our single Trp mutants, we are able to distinguish that the two prion forms have different microenvironment at various residue positions reflecting the differences in the arrangement of the side chains in the well-ordered fibrils. The residue positions from 2 to 31 encompassing almost the entire Gln/Asn-rich subdomain are highly buried in the amyloid structure. The two strains had local structural differences in this subdomain indicating the differential packing of the side chains. The adjacent residues positions from 51 to 86 which includes the oligopeptide repeats are moderately buried in the amyloid structure. Further, the residue positions from 96 to 121 become more buried in the structure indicating the local structural constraints around the side chains. Taken together, our results establish that the amyloid core of both the prion strains have a distinct amyloid structure with many side chains observed by Trp residues have different microenvironment and flexibility.

Unlike the N domain, dynamic nature of the M domain in the amyloid state is highly debated. Previous studies report that the M domain is flexible part of β-helical or rigid structural part of the parallel in-register amyloid core (19, 26). Our results suggest that the residue positions (184, 221 and 250) in the M domain are highly dynamic in both the prion

fibrils. However, the residue positions are found to be more structured in Sc37 compared to that of Sc4 conformations as supported by earlier reports. *In vitro* studies suggest that the M-domain contains the primary binding site for Hsp104 which is an essential for the fibril fragmentation and propagation (32). Therefore, the differences in the dynamic nature of M domain can have an important role in the Hsp104 binding and severing activity required for the stable inheritance of the two prion strains.

In summary, our approach provides new residue specific insights into the organization and dynamics of the amyloid fibrils of two distinct [PSI^{+}] prion conformations. Tryptophan fluorescence is a reliable indicator of the micro-environment and is able to distinguish the packing of the prion core. Additionally, the polypeptide segment that extends from the amyloid core is more dynamic in Sc4 compared to that of Sc37 conformation. The differences in the dynamic nature of the amyloid core and the M domain can be the underlying mechanism for regulating the Hsp104 activity which consequently affects the inheritance of prion strains.

5.5 References

1. Uptain SM & Lindquist S (2002) Prions as protein-based genetic elements. (Translated from eng) *Annu Rev Microbiol* 56:703-741 (in eng).
2. Prusiner SB, Scott MR, DeArmond SJ, & Cohen FE (1998) Prion protein biology. *Cell* 93(3):337-348.
3. Chien P, Weissman JS, & DePace AH (2004) Emerging principles of conformation-based prion inheritance. *Annual review of biochemistry* 73:617-656.
4. Collinge J, Sidle KC, Meads J, Ironside J, & Hill AF (1996) Molecular analysis of prion strain variation and the aetiology of 'new variant' CJD. *Nature* 383(6602):685-690.
5. Safar J, *et al.* (1998) Eight prion strains have PrP(Sc) molecules with different conformations. *Nature medicine* 4(10):1157-1165.
6. Tycko R (2015) Amyloid Polymorphism: Structural Basis and Neurobiological Relevance. *Neuron* 86(3):632-645.
7. Paushkin SV, Kushnirov VV, Smirnov VN, & Ter-Avanesyan MD (1997) In vitro propagation of the prion-like state of yeast Sup35 protein. *Science* 277(5324):381-383.
8. Glover JR, *et al.* (1997) Self-seeded fibers formed by Sup35, the protein determinant of [PSI+], a heritable prion-like factor of S. cerevisiae. *Cell* 89(5):811-819.
9. Derkatch IL, Chernoff YO, Kushnirov VV, Inge-Vechtomov SG, & Liebman SW (1996) Genesis and variability of [PSI] prion factors in Saccharomyces cerevisiae. *Genetics* 144(4):1375-1386.
10. Ter-Avanesyan MD, Dagkesamanskaya AR, Kushnirov VV, & Smirnov VN (1994) The SUP35 omnipotent suppressor gene is involved in the maintenance of the non-Mendelian determinant [psi+] in the yeast Saccharomyces cerevisiae. *Genetics* 137(3):671-676.
11. Liu JJ, Sondheimer N, & Lindquist SL (2002) Changes in the middle region of Sup35 profoundly alter the nature of epigenetic inheritance for the yeast prion [PSI+]. *Proceedings of the National Academy of Sciences of the United States of America* 99 Suppl 4:16446-16453.
12. Ter-Avanesyan MD, *et al.* (1993) Deletion analysis of the SUP35 gene of the yeast Saccharomyces cerevisiae reveals two non-overlapping functional regions in the encoded protein. *Molecular microbiology* 7(5):683-692.

13. Tanaka M, Chien P, Naber N, Cooke R, & Weissman JS (2004) Conformational variations in an infectious protein determine prion strain differences. *Nature* 428(6980):323-328.
14. Krishnan R & Lindquist SL (2005) Structural insights into a yeast prion illuminate nucleation and strain diversity. *Nature* 435(7043):765-772.
15. Toyama BH, Kelly MJS, Gross JD, & Weissman JS (2007) The structural basis of yeast prion strain variants. *Nature* 449(7159):233-237.
16. Tanaka M, Collins SR, Toyama BH, & Weissman JS (2006) The physical basis of how prion conformations determine strain phenotypes. *Nature* 442(7102):585-589.
17. Chernoff YO, Lindquist SL, Ono B-i, Inge-Vechtomov SG, & Liebman SW (1995) Role of the chaperone protein Hsp104 in propagation of the yeast prion-like factor [psi+]. *Science* 268(5212):880-884.
18. Reidy M & Masison DC (2011) Modulation and elimination of yeast prions by protein chaperones and co-chaperones. *Prion* 5(4):245-249.
19. Wickner RB, *et al.* (2015) Yeast prions: structure, biology, and prion-handling systems. *Microbiology and molecular biology reviews : MMBR* 79(1):1-17.
20. Ross ED, Edskes HK, Terry MJ, & Wickner RB (2005) Primary sequence independence for prion formation. *Proceedings of the National Academy of Sciences of the United States of America* 102(36):12825-12830.
21. Diaz-Avalos R, King C-Y, Wall J, Simon M, & Caspar DL (2005) Strain-specific morphologies of yeast prion amyloid fibrils. *Proceedings of the National Academy of Sciences of the United States of America* 102(29):10165-10170.
22. Chen B, Thurber KR, Shewmaker F, Wickner RB, & Tycko R (2009) Measurement of amyloid fibril mass-per-length by tilted-beam transmission electron microscopy. *Proceedings of the National Academy of Sciences* 106(34):14339-14344.
23. Shewmaker F, Wickner RB, & Tycko R (2006) Amyloid of the prion domain of Sup35p has an in-register parallel β-sheet structure. *Proceedings of the National Academy of Sciences* 103(52):19754-19759.
24. Shewmaker F, Ross ED, Tycko R, & Wickner RB (2008) Amyloids of Shuffled Prion Domains That Form Prions Have a Parallel In-Register β-Sheet Structure†. *Biochemistry* 47(13):4000-4007.
25. Wetzel R (2002) Ideas of order for amyloid fibril structure. *Structure* 10(8):1031-1036.

26. Krishnan R & Lindquist SL (2005) Structural insights into a yeast prion illuminate nucleation and strain diversity. *Nature* 435(7043):765-772.
27. Lakowicz JR (2007) *Principles of fluorescence spectroscopy* (Springer Science & Business Media).
28. Jha A, Udgaonkar JB, & Krishnamoorthy G (2009) Characterization of the heterogeneity and specificity of interpolypeptide interactions in amyloid protofibrils by measurement of site-specific fluorescence anisotropy decay kinetics. *Journal of molecular biology* 393(3):735-752.
29. Palhano FL, *et al.* (2009) A fluorescent mutant of the NM domain of the yeast prion Sup35 provides insight into fibril formation and stability. *Biochemistry* 48(29):6811-6823.
30. Chen Y & Barkley MD (1998) Toward understanding tryptophan fluorescence in proteins. *Biochemistry* 37(28):9976-9982.
31. True HL & Lindquist SL (2000) A yeast prion provides a mechanism for genetic variation and phenotypic diversity. *Nature* 407(6803):477-483.
32. Helsen CW & Glover JR (2012) Insight into molecular basis of curing of [PSI+] prion by overexpression of 104-kDa heat shock protein (Hsp104). *The Journal of biological chemistry* 287(1):542-556.

Mapping the dynamics of interstitial water in the amyloid folds of distinct prion strains

6.1 Introduction

Fungal prions share many properties with the mammalian prion and hence serve as a good model system to understand many mysteries of prions, such as strain phenomenon. The propagation and inheritance of [*PSI*$^{+}$] prion in yeast are well-studied. The prion state is formed by the conversion of soluble functional Sup35p, a translation termination factor, into non-functional amyloid fibrils (1, 2). *In vitro*, Sup35NM aggregates at 4 and 37 °C to form amyloid fibrils with distinct molecular structures (3). The amyloid core in 37 °C (Sc37) fibrils is more expanded and thermodynamically more stable than fibrils formed at 4 °C (Sc4) (4, 5) which can be the plausible reason for [*PSI*$^{+}$] prion strains *in vivo*.

However, the majority of these studies carried out to comprehend the structural differences in amyloid strains are based on protein centric perspective. Whereas, very recently water centric perspective has gained a lot of attention as it has been shown that water plays a fundamental role in maintaining the structure, stability, and function of proteins (6-8). However, the role of water in amyloid fibril formation and conformational diversity has not yet been explored. The main aim of our study is to understand the nature of local solvation dynamics along the polypeptide chain length using single Trp mutants and to discern the water dynamics between different strains. The dynamic nature of water molecules in proteins can be examined either by using intrinsic or extrinsic fluorescent probes. Since, the installation of external fluorophore can affect the biological property of a protein, we chose to use intrinsic Trp fluorescence to monitor the site-specific solvation dynamics in amyloid fibrils. Many other groups including ours have extensively used Trp fluorescence to study the hydration dynamics in proteins (9-17). To carry out our experiments, we used single tryptophan mutants (W104, W117, W129, W137 and W184) along the polypeptide chain in both N domain (residues 104 and 117) and M domain (residues 129, 137 and 184). These residues are previously known to be significantly solvent exposed after assembly into amyloid (4, 5). Further, these residues are located in the stretch of sequence which is required for Hsp104 binding and prion strain propagation (18, 19). Therefore, it is interesting to understand the solvation dynamics in the two distinct amyloid states of Sup35NM around these residues which can possibly affect the Hsp104 interactions with the Sup35NM amyloid. This differential interaction of Hsp104 with two distinct amyloid state of Sup35 can be the possible reason for the strain phenomenon in yeast.

6.2 Experimental section

For materials; mutagenesis, protein expression and purification; and fibril preparation, please see chapter 5.

6.2.1 Steady-state fluorescence measurements

Steady-state tryptophan fluorescence measurements were performed on FluoroMax-4 (Horiba Jobin Yvon NJ). For Trp fluorescence spectra, excitation wavelength was set at 295 nm, excitation and emission slit widths were 0.8 nm and 4 nm, respectively. All the spectra were buffer subtracted to remove any contribution due to the solvent Raman scattering.

6.2.2 Time-resolved fluorescence measurements

Time-resolved fluorescence decay experiments were carried out using picosecond rhodamine 6G dye laser (Spectra Physics, Mountain View, CA) coupled to a time-correlated single-photon counting (TCSPC) setup. A mode-locked frequency doubled Nd:YAG laser (Millenia X, Spectra Physics) was used to pump a dye laser and the generated laser pulses were frequency doubled to 295 nm by using a KDP crystal. The instrument response function (IRF) at 295 nm was collected using a colloidal suspension of dried non-dairy coffee whitener and the width (full width at half maximum) of the IRF was ~60 ps. The emission of trp fluorescence was collected using a microchannel plate photomultiplier (2809u, Hamamatsu, Hamamatsu City, Japan). For time-resolved fluorescence intensity decay measurements, emission monochromator was fixed at 345 nm and the fluorescence was collected at magic angle (54.7°) with respect to the excitation polarizer and the peak count was ~10,000.

6.2.3 Construction of time-resolved emission spectra (TRES)

For constructing TRES, Trp fluorescence intensity decays were collected at different wavelengths ranging from 320 nm to 380 nm in intervals of 5 nm. The emission bandpass was 5 nm. The emission decays were fitted to a function by using a nonlinear least square procedure that involves the convolution of the instrument response function with a sum of exponentials. The derived parameters were then used to stimulate the fluorescence decay curve at different emission wavelengths in origin using $I_\lambda(t) = \Sigma\alpha_i e^{-t/\tau_i}$, where τ_i and α_i represents the lifetime components and the associated contributions, respectively. The overall time-resolved emission spectra were constructed using (20):

$$I\ (\lambda, t) = \frac{I_{\lambda}^{SS}\, I_{\lambda}(t)}{\Sigma\, \alpha_i \tau_i} \qquad (6.1)$$

where I_{λ}^{SS} is the steady-state fluorescence intensity at fixed wavelength. The resulting time-resolved spectra were fitted with a log-normal function to estimate the emission maxima *v* (t) as a function of time. The hydration correlation function is constructed from the time-resolved spectra as follows:

$$c\ (t) = \frac{\nu(t) - \nu(\infty)}{\nu(0) - \nu(\infty)} \qquad (6.2)$$

where $\nu(0)$, $\nu(t)$, $\nu(\infty)$ are time-resolved emission maxima (in cm^{-1}) at time 0, t and infinity, respectively. The determination of the exact position of time-zero spectrum of Trp is difficult due to experimental resolution (~ 60ps). Therefore, to get more precise information regarding the spectral shift and solvation dynamics, we used 31056 cm^{-1} as *v* (0) corresponding to wavelength 322 nm, reported previously for Trp solvation using femtosecond laser. The correlation function was then fitted using a sum of exponentials as follows:

$$C\ (t) = \sum \beta_i\, e^{-t/\tau_{si}} \qquad (6.3)$$

where τ_{si} and β_i represent the solvation time and the associated amplitude of the solvent components respectively.

6.3 Results and discussion

6.3.1 Steady state fluorescence

In the denatured state, Trp fluorescence emission spectra of all the 5 mutants showed peak ~345 nm suggesting the solvent-exposed nature of the residues (Fig. 6.1 *a*). After assembly into fibrils at 4 °C and 37 °C, all the mutants showed a blue shift in fluorescence emission maxima. In Sc4 amyloid conformation, the blue shift in emission maxima is more significant in W104, W117 and W129 relative to W137 and W184 (Fig 6.1 *b*). In Sc37 amyloid conformation, a similar pattern of blue shift in Trp fluorescence emission maxima was observed (Fig. 6.1 *c*). However, the emission maxima of residues are more blue shifted in Sc37 amyloid conformation as compared to the Sc4 amyloid conformation signifying that the residues are more buried in the earlier (Fig. 6.1 *d*). These results are in corroboration with the previously reported NMR and acrylodan-labeling results suggesting that the amyloid core is more extended in the Sc37 amyloid conformation (4, 5).

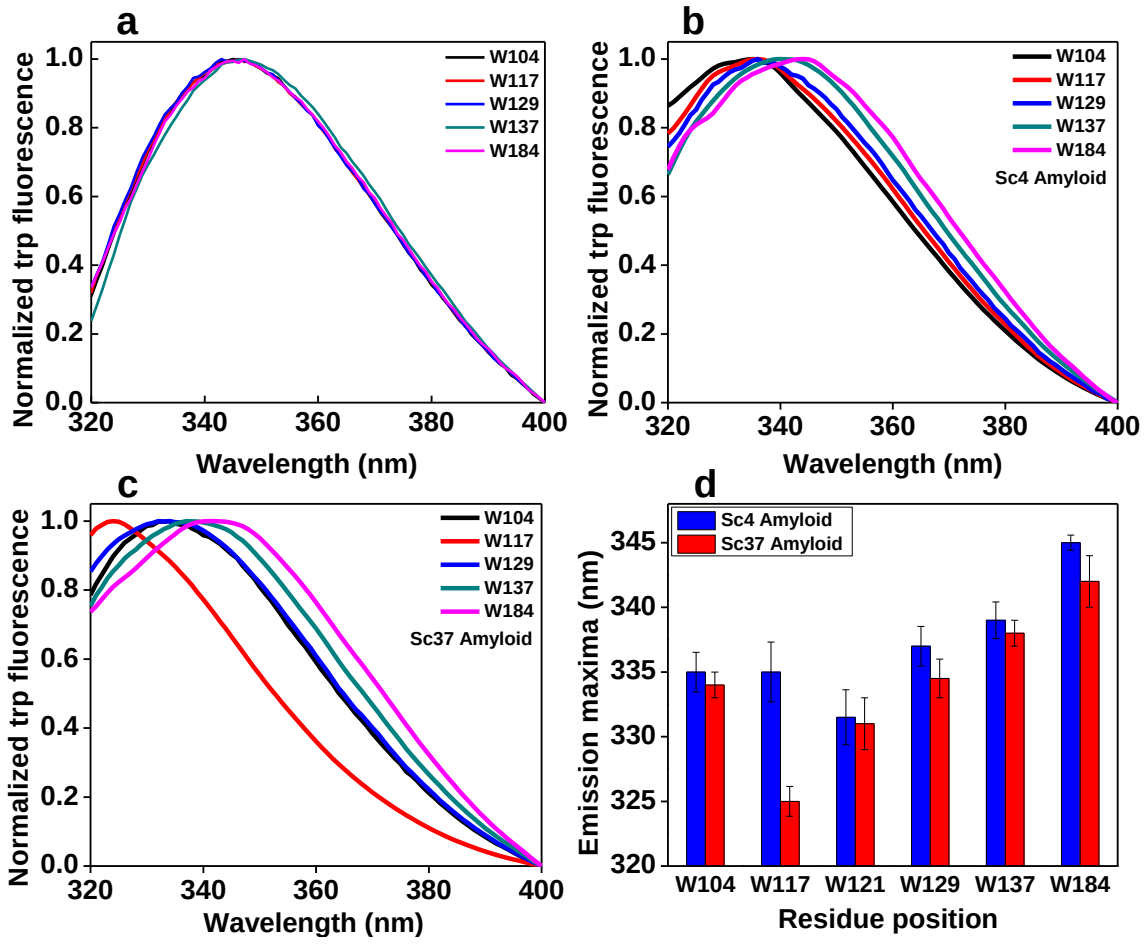

Figure 6.1 Steady state normalized Trp fluorescence spectra of all the mutants in the denatured (a), Sc4 (b) and Sc37 (c) amyloid conformations. (d) Comparison of Trp emission maxima of all the mutants in the Sc4 and Sc37 amyloid conformations.

6.3.2 Time-resolved emission spectra (TRES)

Next, in order to get insights into the solvation dynamics around these residues, we carried out time-resolved fluorescence intensity decay measurements. Fig. 6.2 *a* and *c* show the time-resolved fluorescence intensity decays of W117 in the Sc4 and Sc37 amyloid conformations, respectively at different emission wavelengths ranging from 320 nm to 380 nm. The intensity decay becomes progressively longer as a function of emission wavelength demonstrating the presence of slow nanosecond solvent relaxation. Time-resolved emission spectra (TRES) was constructed from these decays (Fig. 6.2 *b* and 6.2 *d*) and the corresponding observed total Stokes shift and solvation correlation functions were constructed using eq. 6.2.

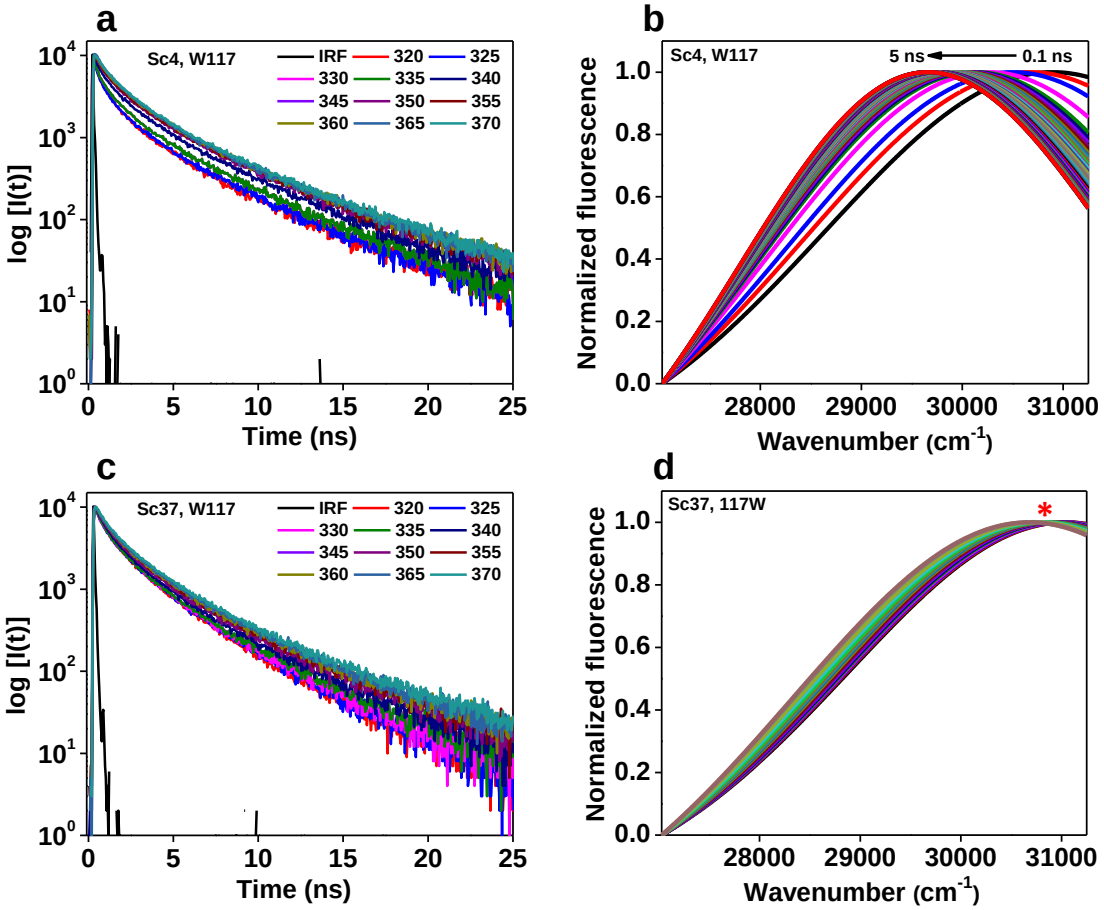

Figure 6.2 Time-resolved fluorescence intensity decays of W117 at different emission wavelengths in Sc4 (*a*) and Sc37 (*c*) amyloid conformations. TRES was constructed from the fluorescence transients of the Sc4 (b) and Sc37 (d) conformations of mutant W117. * No significant Stokes shift observed.

Using this approach, we constructed the time-resolved emission spectra for all the mutants in the amyloid conformations formed at 4 °C and 37 °C (Figure 6.3, 6.4).

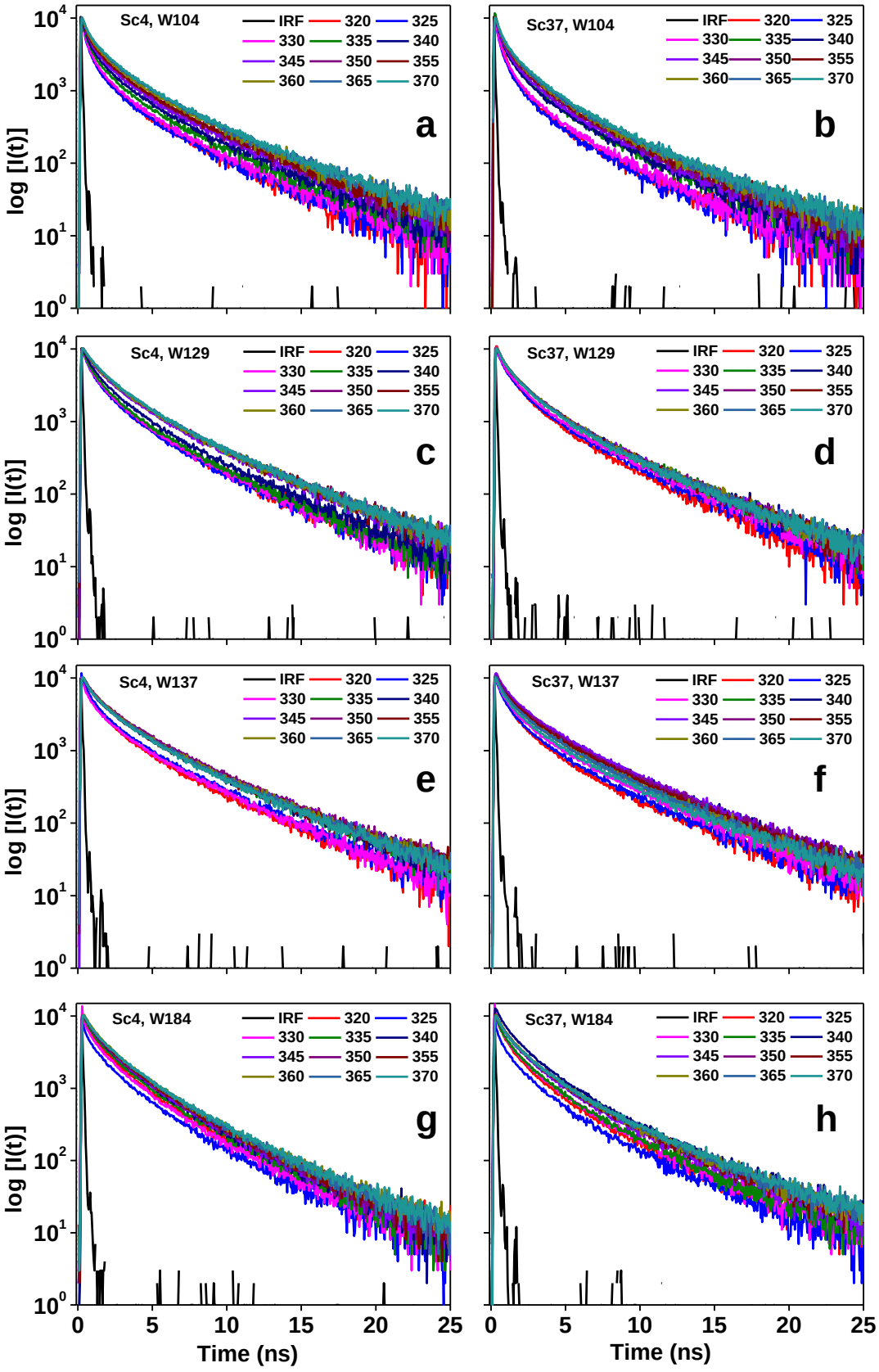

Figure 6.3 Time-resolved fluorescence intensity decays of mutant W104 (a), W129 (c), W137 (e) and W184 (g) at different emission wavelengths in Sc4 amyloid conformation. Time-resolved fluorescence decays at different emission wavelengths of mutant W104 (b), W129 (d), W137 (f) and W184 (h) in Sc37 amyloid conformation.

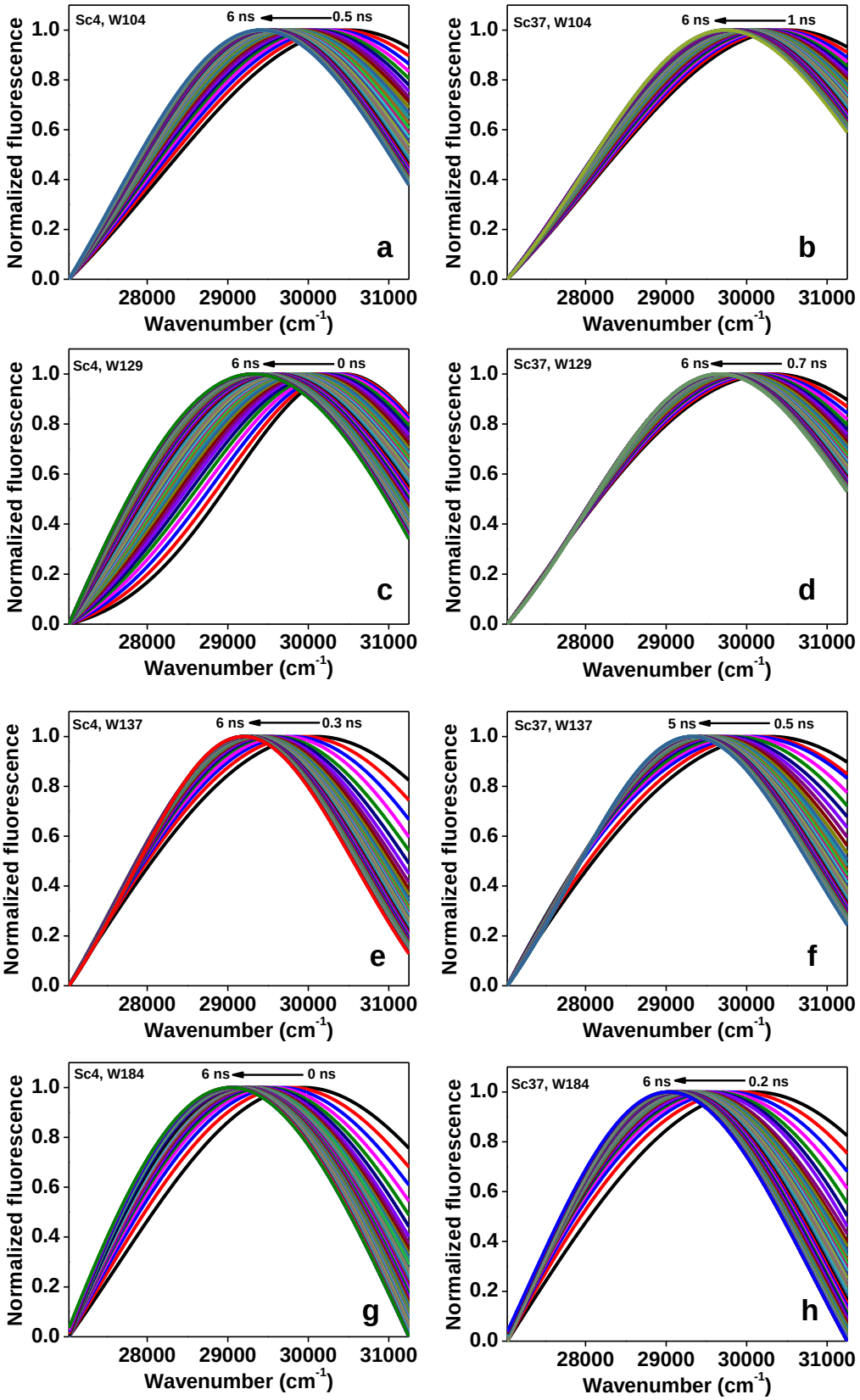

Figure 6.4 Time-resolved emission spectra constructed from the fluorescence decays of the mutant W104 (a) W129 (c) W137 (e) and W184 (g) in the Sc4 amyloid conformation. Time-resolved emission spectra constructed from the fluorescence decays of the mutant W104 (b) W129 (d) W137 (f) and W184 (h) in the Sc37 amyloid conformation.

This approach was used to estimate the total dynamic Stokes shifts during solvation relaxation of all the mutants in Sc4 and Sc37 amyloid conformations and is shown in Fig. 6.5 *a*. The observed Stokes shifts show a gradual increase from residue W104 to W184 similar to that of emission maxima shift. As the location of the Trp residue progressively moves towards the surface, the obtained total dynamic Stokes shifts increase from ~ 1640 cm^{-1} to ~ 2008 cm^{-1} and ~ 1319 cm^{-1} to ~ 2021 cm^{-1} for the 4 °C and 37 °C fibrils, respectively with an exception of W117 (Fig. 6.5 *a*). This indicates that the observed Stokes shift is predominantly due to solvent hydration. Interestingly, this kind of relationship has already been reported for a globular protein where the solvation dynamics at 29 different positions and states was monitored using 16 Trp mutants (15). For W117, there is a negligible Stokes shift in the Sc37 amyloid conformation and is strikingly different from the Sc4 amyloid conformation signifying the presence of dry interface around the region.

It is known that solvation dynamics in proteins can vary from bulk-type behavior (~ 1 ps) to buried-water behavior (few ns) (21, 22). Previous studies on local solvation dynamics around the protein surface using single Trp probe shows a biphasic behavior of the solvation correlation function where the ultrafast dynamics (1-10 ps) represents the bulk-type hydration around the probe and tens to hundreds of picoseconds dynamics represents the dynamic exchange between hydration water and bulk water (15, 23-26). In our studies, we have not been able to resolve this ultrafast component but for most of our experiments, we observed two components (fast: sub-nanoseconds and slow: nanoseconds). The fast sub-nanosecond solvation correlation function represents the dynamic exchange rate between the strongly bound water and bulk water which arises due to protein structural fluctuations (15). In Sc4 amyloid conformation, this sub-nanosecond component was not observed for W104 whereas around W137, the relaxation takes the longest time (~ 450 ps) as compared to W117 (~270 ps), W129 (~ 100 ps) and W184 (~ 86 ps) (Fig. 6.5 & Table 6.1). For residue 104, the presence of a nanosecond component instead of a sub-nanosecond component, indicates that the bound water molecules are more tightly held around the region in comparison to the other residues. The amplitudes of fast relaxation components are ~ 46%, ~ 28%, ~ 88% and ~ 72% for W117, W129, W137 and W184, respectively (Table 6.1). The percentage increase in the amplitude of fast hydration for W137 and W184 indicates that the exchange rate between the bulk and the bound water increases owing to more exposed nature of the residues and this corroborate well with the Stokes shifts data. Interestingly, in the Sc37 amyloid conformation, the fast sub-nanosecond component of solvent relaxation was observed for W184 only. The solvation correlation time is ~ 180 ps and amplitude is ~ 64%.

Instead of sub-nanosecond component, residues (W104, W129 and W137) in the Sc37 amyloid conformation showed only nanosecond component (Table 6.1). The absence of sub-nanosecond component in the Sc37 amyloid conformation indicate that either is no exchange between bulk and bound water or exchange rate become significantly slow that it happens on the nanosecond timescale. Since, these residues are significantly exposed to solvent in the amyloid state, there should be a dynamic exchange between bound and bulk water. Therefore, the presence of nanosecond component in the Sc37 amyloid conformation could be due to exchange between the bulk and bound water molecules around the proteins surface in the amyloid state. The presence of longer timescale of hydration dynamics in Sc37 amyloid conformation indicates that the water molecules are more ordered and strongly bound around these regions in Sc37 as compared to Sc4 amyloid conformations.

The slow component observed on the nanosecond timescale could be because of the collective water network rearrangements trapped inside the fibrils. In the Sc4 amyloid conformation, the observed relaxation time for W117, W129, W137 and W184 are ~ 1.5 ns, 1.7 ns, 1.8 ns and 1.7 ns, respectively (Table 6.1). On the contrary, in the Sc37 amyloid conformation, the slow component was observed only for W184 (~ 1.5 ns) (Table 6.1). These solvation correlation time values show a poor relationship with the emission maxima of the probes. The residues which are more buried like W117 (~ 1.5 ns), W129 (~ 1.7) show shorter correlation times compared to exposed residue W184 (~ 1.72 ns). For W184, both Sc4 and Sc37 amyloid conformations show similar hydration time scale and amplitudes.

Table 6.1

Residue	Sc4		Sc37	
	τ_1 (ns) (c_1)	τ_2 (ns) (c_2)	τ_1 (ns) (c_1)	τ_2 (ns) (c_2)
W104	---	1.10	---	1.68
W117	0.27 (0.46)	1.47 (0.54)	---	---
W129	0.1 (0.28)	1.66 (0.72)	---	0.93
W137	0.45 (0.88)	1.83 (0.12)	---	0.76
W184	0.086 (0.72)	1.72 (0.28)	0.18 (0.64)	1.51 (0.36)

Typical errors in the analysis of time-resolved emission spectra are as follows: $\tau_1 \leq 15\%$; $c_1 \leq 13\%$; $\tau_2 \leq 10\%$ and $c_2 \leq 18\%$.

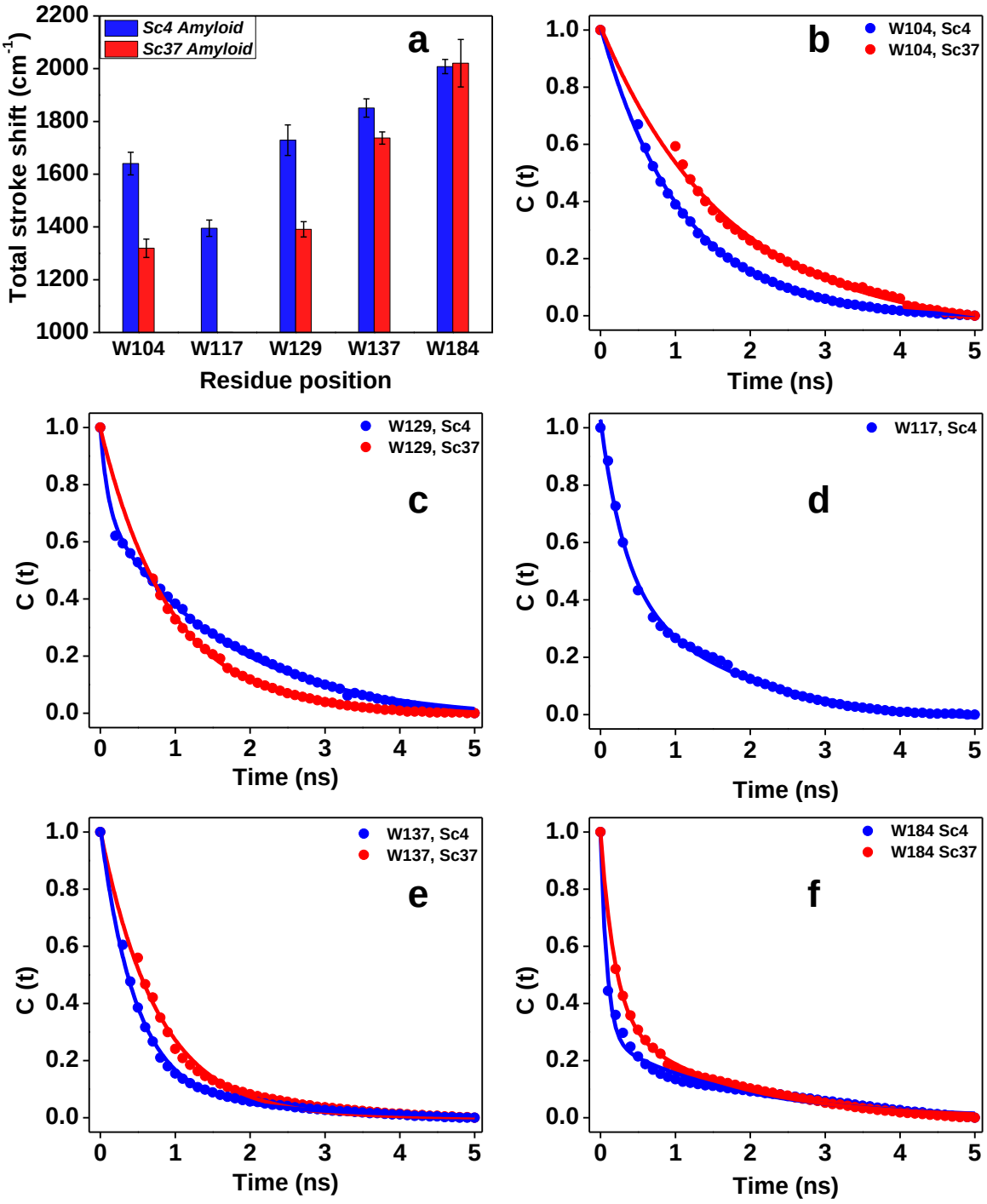

Figure 6.5 (a) The total dynamic Stokes shifts of all the mutants in the Sc4 (blue) and Sc37 (red) amyloid conformations. Hydration correlation functions probed by Trp in the Sc4 and Sc37 amyloid conformations of mutant W104 (b), W117 (c), W129 (d), W137 (e), and W184 (f). The solid blue and red circle represents the solvation function of the Sc4 and Sc37 amyloid conformations. The solid blue and red line represents the corresponding exponential fit.

6.4 Conclusion

In summary, our results suggest that the solvation dynamics around amyloid fibrils is 2-3 orders of magnitude slower than in bulk water (~ 1 ps). Further, the solvation dynamics was found to be slower in Sc37 compared to Sc4 amyloid conformation. The differences in the solvation dynamics in two different fibrillar states can have important biological implications in the propagation and inheritance of two different prion strains. Previous *in vivo* studies have shown that the region from residue 1 to 137 is important for the maintenance of weak or strong [PSI^{+}] prion (18) and mutations in the M-domain (residue 124-253) affects the stable inheritance of prion (27). Further, it has also been shown that the primary site for Hsp104 binding is in the M-domain and mutations in the region prevent curing by over-expression of Hsp104 (19). Together, these observations suggest that the M-domain has significant role in the binding and the prion severing activity of Hsp104 which is essential for prion inheritance. Since, the role of solvation dynamics in protein recognition and enzyme activity is now well established (28), we speculate that the distinct solvation dynamics has an important implication in amyloids conformations also. Difference in solvation dynamics in distinct amyloid strains explains the differential severing efficiency of Hsp104 on these strains, which in turn affects the inheritance pattern of strong and weak strains of [PSI^{+}] prion.

6.5 References

1. Paushkin SV, Kushnirov VV, Smirnov VN, & Ter-Avanesyan MD (1997) In vitro propagation of the prion-like state of yeast Sup35 protein. *Science* 277(5324):381-383.
2. Glover JR, *et al.* (1997) Self-seeded fibers formed by Sup35, the protein determinant of [PSI+], a heritable prion-like factor of S. cerevisiae. *Cell* 89(5):811-819.
3. Tanaka M, Chien P, Naber N, Cooke R, & Weissman JS (2004) Conformational variations in an infectious protein determine prion strain differences. *Nature* 428(6980):323-328.
4. Krishnan R & Lindquist SL (2005) Structural insights into a yeast prion illuminate nucleation and strain diversity. *Nature* 435(7043):765-772.
5. Toyama BH, Kelly MJS, Gross JD, & Weissman JS (2007) The structural basis of yeast prion strain variants. *Nature* 449(7159):233-237.
6. Chaplin M (2006) Do we underestimate the importance of water in cell biology? *Nature reviews. Molecular cell biology* 7(11):861-866.
7. Levy Y & Onuchic JN (2006) Water mediation in protein folding and molecular recognition. *Annual review of biophysics and biomolecular structure* 35:389-415.
8. Bagchi K & Roy S (2014) Sensitivity of water dynamics to biologically significant surfaces of monomeric insulin: role of topology and electrostatic interactions. *The journal of physical chemistry. B* 118(14):3805-3813.
9. Arya S & Mukhopadhyay S (2014) Ordered water within the collapsed globules of an amyloidogenic intrinsically disordered protein. (Translated from eng) *The journal of physical chemistry. B* 118(31):9191-9198 (in eng).
10. Yang J, Zhang L, Wang L, & Zhong D (2012) Femtosecond conical intersection dynamics of tryptophan in proteins and validation of slowdown of hydration layer dynamics. (Translated from eng) *Journal of the American Chemical Society* 134(40):16460-16463 (in eng).
11. Zhong D, Pal SK, & Zewail AH (2011) Biological water: A critique. *Chemical Physics Letters* 503(1):1-11.
12. Zhong D (2009) Hydration dynamics and coupled water-protein fluctuations probed by intrinsic tryptophan. *Adv Chem Phys* 143:83-149.

13. Zhang L, Yang Y, Kao YT, Wang L, & Zhong D (2009) Protein hydration dynamics and molecular mechanism of coupled water-protein fluctuations. *Journal of the American Chemical Society* 131(30):10677-10691.
14. Xu J, *et al.* (2009) Femtosecond fluorescence spectra of tryptophan in human gamma-crystallin mutants: site-dependent ultrafast quenching. (Translated from eng) *Journal of the American Chemical Society* 131(46):16751-16757 (in eng).
15. Zhang L, *et al.* (2007) Mapping hydration dynamics around a protein surface. *Proceedings of the National Academy of Sciences of the United States of America* 104(47):18461-18466.
16. Qiu W, *et al.* (2006) Protein surface hydration mapped by site-specific mutations. (Translated from eng) *Proceedings of the National Academy of Sciences of the United States of America* 103(38):13979-13984 (in eng).
17. Xu J, *et al.* (2006) Ultrafast fluorescence dynamics of tryptophan in the proteins monellin and IIAGlc. (Translated from eng) *Journal of the American Chemical Society* 128(4):1214-1221 (in eng).
18. Bradley ME & Liebman SW (2004) The Sup35 domains required for maintenance of weak, strong or undifferentiated yeast [PSI+] prions. *Molecular microbiology* 51(6):1649-1659.
19. Helsen CW & Glover JR (2012) Insight into molecular basis of curing of [PSI+] prion by overexpression of 104-kDa heat shock protein (Hsp104). *The Journal of biological chemistry* 287(1):542-556.
20. Lakowicz JR (2013) *Principles of fluorescence spectroscopy* (Springer Science & Business Media).
21. Pal SK & Zewail AH (2004) Dynamics of water in biological recognition. (Translated from eng) *Chem Rev* 104(4):2099-2123 (in eng).
22. Toptygin D, Woolf TB, & Brand L (2010) Picosecond protein dynamics: the origin of the time-dependent spectral shift in the fluorescence of the single Trp in the protein GB1. (Translated from eng) *The journal of physical chemistry. B* 114(34):11323-11337 (in eng).
23. Peon J, Pal SK, & Zewail AH (2002) Hydration at the surface of the protein Monellin: dynamics with femtosecond resolution. (Translated from eng) *Proceedings of the National Academy of Sciences of the United States of America* 99(17):10964-10969 (in eng).

24. Pal SK, Peon J, & Zewail AH (2002) Biological water at the protein surface: dynamical solvation probed directly with femtosecond resolution. (Translated from eng) *Proceedings of the National Academy of Sciences of the United States of America* 99(4):1763-1768 (in eng).
25. Qiu W, *et al.* (2005) Ultrafast hydration dynamics in melittin folding and aggregation: helix formation and tetramer self-assembly. (Translated from eng) *The journal of physical chemistry. B* 109(35):16901-16910 (in eng).
26. Qiu W, *et al.* (2006) Ultrafast solvation dynamics of human serum albumin: correlations with conformational transitions and site-selected recognition. (Translated from eng) *The journal of physical chemistry. B* 110(21):10540-10549 (in eng).
27. Liu JJ, Sondheimer N, & Lindquist SL (2002) Changes in the middle region of Sup35 profoundly alter the nature of epigenetic inheritance for the yeast prion [PSI+]. *Proceedings of the National Academy of Sciences of the United States of America* 99 Suppl 4:16446-16453.
28. Chang CW, *et al.* (2010) Ultrafast solvation dynamics at binding and active sites of photolyases. (Translated from eng) *Proceedings of the National Academy of Sciences of the United States of America* 107(7):2914-2919 (in eng).

List of Publications

1. Narang D and Mukhopadhyay S. Stepwise expansion of human β_2-microglobulin into a disordered amyloidogenic precursor (under review).

2. Narang D, Sharma PK, and Mukhopadhyay S (2013) Dynamics and dimension of an amyloidogenic disordered state of human β_2-microglobulin. *Eur Biophys J* 42: 767-776.

3. Dalal V, Bhattacharya M, Narang D, Sharma PK, and Mukhopadhyay S (2012) Nanoscale fluorescence imaging of single amyloid fibrils. *J Phys Chem Lett* 3:1783–1787.

4. Narang D and Mukhopadhyay S. Water dynamics within the amyloid fibrils distinguishes the yeast prion [PSI^+] strain variants. (Manuscript in preparation)

5. Narang D and Mukhopadhyay S. Structural differences between the amyloid fibrils of Yeast Prion [PSI^+] probed by site-specific Trp fluorescence. (Manuscript in preparation)

6. Narang D, Singh A, and Mukhopadhyay S. Effect of salt on the oligomerization state of human β_2-microglobulin under amyloidogenic condition. (Manuscript in preparation)

Presentation and Abstracts

1. Dominic Narang, Anup K. Srivastava and Samrat Mukhopadhyay (**2015**) The Role of Structural Dynamics in Determining the Prion Strain Diversity, *59th Annual Meeting of the Biophysical Society*, Baltimore Convention Centre, Baltimore, Maryland, USA.

2. Dominic Narang, Pushpender K. Sharma, Mily Bhattacharya, Vijit Dalal, and Samrat Mukhopadhyay (**2013**) Assembly of Amyloidogenic Disordered State of Human β_2-microglobulin into Amyloid Fibril, *82nd Annual Meeting of Society of Biological Chemists*, University of Hyderabad, Hyderabad, India.

3. Dominic Narang, Pushpender K. Sharma, G. Vinodh Kumar, Mily Bhattacharya, Vijit Dalal, and Samrat Mukhopadhyay (**2012**) Dynamical Insights into the Compact Disordered State of Amyloidogenic Human β_2-microglobulin, *International Symposium on Protein Folding and Dynamics*, National Centre for Biological Sciences, Bangalore.

4. Dominic Narang, Pushpender K. Sharma, Mily Bhattacharya, Vijit Dalal and Samrat Mukhopadhayay (**2011**) Mechanism of β_2-Microglobulin Aggregation Leading to Amyloid Fibril Formation, *National Fluorescence Workshop: Spectroscopy and Microscopy in Biology and Chemistry*, Jawaharlal Nehru University, New Delhi, India.